Development of Asymmetric Sulfoxidation Catalysts Based on Functional Models for Vanadium-Dependent Haloperoxidases

by

Curtis J. Schneider

A dissertation submitted in partial fulfillment
of the requirements for the degree of
Doctor of Philosophy
(Chemistry)
in The University of Michigan
2009

Doctoral Committee:

Professor Vincent L. Pecoraro, Chair
Professor David E. Ballou
Professor James E. Penner-Hahn
Assistant Professor Marc J. A. Johnson

To My Loving Wife, Elizabeth

Acknowledgements

First and foremost, I must thank Prof. Vincent L. Pecoraro for his unwavering support over the course my tenure at the University of Michigan. His guidance has taught me that there are no negative results; every experiment regardless of the outcome explains something important about the science. Vince has a remarkable talent for placing the appropriate perspective on all aspects of research. Regardless of my level of frustration with the experiments, our conversations are led to positive conclusions and new directions to explore. Vince is always supportive of his students' ideas and goals and consistently provides that extra information necessary to make an intelligent and informed decision. I would not have been able to make to this point in my academic career without his support. For all of his support, both in research and in career decisions, I am forever indebted. Thank you!

At the start of my graduate career, my research interests spanned both physical and inorganic chemistry. Prof. James E. Penner-Hahn significantly impacted my early development as a scientist through the application of x-ray absorption spectroscopy to bioinorganic chemistry. His early guidance helped to solidified my interest in research at the interface of chemistry and biology. Jim has been exceptionally patient over the years while I have fought through the

learning curves associated with the processing of x-ray absorption spectra. This work resulted in a significant portion of the research presented in Chapter 3.

Over the years, I have had the opportunity to work with a number of incredibly talented scientists. Prof. Marciela Scarpellini provided incredible insight into ligand synthesis and metal complexation. Jessica Gaetjens, Ph.D., assisted my efforts in the synthesis of vanadium coordination complexes. Marciela and Jessica greatly assisted my research early on in my graduate career; while their contributions to my doctorate stand-out, they do not overshadow the support provided by all members of the Pecoraro group. My favorite aspect of the Pecoraro group has been the international atmosphere created by the group members. The culturally diversity present in the group provided incredible insight into the subtleties of dealing with other cultures in a collaborative fashion.

I had the benefit of spending three months at the University of Milano-Biccoca in the laboratory of Prof. Luca DeGioia working on the theoretical calculations presented in Chapter 2. His abilities as a computational chemist are only exceeded by hospitality. This research trip was my first experience outside of the United States, Prof. DeGioia went out of his way to insure that I was comfortable and enjoying my stay Milan. Within the DeGioia group, I had the pleasure of working with the incredibly talented computational chemistry, Giuseppe Zampella, Ph.D. Without his assistance I would not have been able to complete the detailed computational studies presented in Chapter 2. Giuseppe was also graciousness enough to politely correct my poorly spoken Italian. My

experiences in Milan have dramatically impacted my perspective on science and the world.

Last, but definitely not least, my wife deserves a special thank you. Throughout the emotional roller coaster that is graduate school, she has been an unwavering pillar of support. Without her, none of this would have been possible. Thank you, Elizabeth!

Table of Contents

List of Figures

Figure

List of Tables

Table

List of Abbreviations

VHPO	Vanadium dependent haloperoxidase
DFT	Density Functional Theory
$Hheida^{2-}$	N-hydroxyethyl iminodiacetate
DMS	dimethyl sulfide
XANES	X-ray absorption near edge spectroscopy
XAS	X-ray absorption spectroscopy
FTIR	Fourier transform infrared spectroscopy
bpg^{-1}	bis-pyridylglycinate
Tf^{-1}	triflate
ATR	attenuated total reflectance
NMR	nuclear magnetic resonance
ESI-MS	electrospray ionization mass spectrometry
salen	N,N'-Ethylenebis(salicylimine)
salan	N,N'-Ethylenebis(salicylamine)
$HNorida^{2-}$	N,N-diacetate-(1S,2R-norephedrine)
$Hpheida^{2-}$	N-[(*1R*)1-phenyl-2-hydroxyethyl iminodiacetate)
$Halida^{2-}$	N,N-diacetate-(L-alaninol)
H*t*-butyl-alida	N,N-diacetate-((*1S,2S*) 2-amino-1-*t*-butyl-propan-1-ol)

Chapter 1

Introduction

Transition metals play a variety of diverse roles in biological systems. Zinc supports the folding and structure of transcription co-factors. Copper plays a number of key roles in electron transfer[1] and in the removal of reactive oxygen species via superoxide dismutase.[1] Manganese-containing proteins are responsible for the removal of reactive oxygen species and control one of the most important chemical reactions carried out in biology, the oxidation of water to dioxygen during photosynthesis.[2] Iron is ubiquitous in biology, participating in a large variety of functions including, but not limited to, oxygen transport,[3] electron transfer,[4] and drug metabolism.[5]

Vanadium is not typically an element discussed in the context of biological systems. Nonetheless, vanadium is the second most abundant transition metal in seawater and two examples of vanadium-dependent enzymes have been isolated, vanadium nitrogenase[6] and the vanadium-dependent haloperoxidases (VHPO).[7] Additionally, vanadium complexes have been explored as insulin enhancing agents for treatment of diabetes.[8] This thesis will focus on exploring vanadium based complexes as functional models for VHPOs and their applications to asymmetric catalysis. Vanadium-dependent haloperoxidases are a novel class of peroxidase that carries out the two-electron oxidation of halides and the subsequent addition to an organic substrate. A number of functional models have been studied by various groups; in particular, tripodal amine peroxo-oxovanadium(V) complexes are well known to be efficient functional models of the enzyme. For years researchers have been interested in applying small molecule vanadium complexes as catalysts,[9,10] and functional models for VHPOs provide a well-studied system to design asymmetric catalysts.

High valent vanadium complexes have been employed in a variety of oxidative transformations from the industrial desulfurization of crude oil[11-13] to the asymmetric epoxidation reactions pioneered by K. Barry Sharpless.[14] This introduction will cover vanadium-based oxidative catalysis in both biological and synthetic systems, and discuss the current approaches to asymmetric oxidation reactions with hydrogen peroxide and catalysts based on transition metals.

Activity of Vanadium-dependent Haloperoxidases

Vanadium-dependent haloperoxidases (VHPO) are metalloenzymes containing a mononuclear vanadium(V) co-factor,[15] and they catalyze the oxidation of halides in the presence of hydrogen peroxide. In the presence of an organic substrate, VHPOs carry out the regiospecific halogenation of olefins.

$$H_2O_2 + X^- + H^+ \rightarrow H_2O + HOX$$
$$H_2O_2 + Br^- + R\text{-}H \rightarrow R\text{-}Br + 2H_2O$$

The first example of a vanadoenzyme was the bromoperoxidase isolated from the marine algae *Ascophyllum nodosum* in 1981 by Vilter and co-workers.[7] Since that time a number of examples of VHPOs have been isolated from marine seaweeds,[7] lichens, and terrestrial fungi.[16] VHPOs are named for the most electronegative halide they are capable of oxidizing. For example, the vanadium chloroperoxidase (VCPO) isolated from *Curvularia inaequalis*[17] is competent with respect to chloride, bromide, and iodide oxidation whereas a vanadium bromoperoxidase (VBPO) is capable of oxidizing only the latter two halides. A strong sequence homology between the active sites of VBPO and VCPO exists; the most significant difference is the replacement of a phenylalanine and a tryptophan residue in VCPO by histidine and arginine in VBPO, respectively. A strong pH dependence exists for halide oxidation. In the case of VBPO, the catalytically relevant pKa = 5.9.[18] At pH < 5 the enzyme is irreversibly inactivated by the oxidation of His-404 to 2-oxohistidine. The optimal pH for catalytic

bromination of monochlorodimedone by a VBPO (*Ascophylum nodosum*) is pH=6.5.[19] This limits potential side reactions such as oxidation of active site residues and the halide-assisted disproportionation of hydrogen peroxide. Saturation kinetics observed for halide oxidation indicates that a binding site for the halide exists within the active site. In the absence of an organic substrate, VHPO can generate singlet oxygen via halide-assisted disproportionation of hydrogen peroxide (1).[20]

(1) $\text{“OX”}^{-} + H_2O_2 \rightarrow {}^1O_2 + H_2O + X^-$

Initially, little was known regarding the biological function of vanadium haloperoxidases. Proposed biological functions were a defense mechanism in which oxidation of a halogen generates hypohalous acid, which could passively diffuse from the active site and participate in the synthesis of halogenated natural products or play a direct role in antimicrobial defense. This hypothesis was supported by initial findings that halogenation of prochiral aromatic substrates were not regiospecific.[21-23] In contrast to these results, the kinetics of bromination for certain indoles is not consistent with a mechanism in which a released diffusible species is responsible for substrate halogenation.[24] Additionally, fluorescence quenching with aromatic indole substrates established binding of an organic substrate to a VBPO.[24] Martinez and co-workers demonstrated that vanadium bromoperoxidase catalyzes the regiospecific oxidation of 1,2-di-tert-butylindole,[25] in which bromination of the sterically encumbered C2-C3 position generates a bromonium species that undergoes nucleophilic attack and elimination (Figure 1.1). In sharp contrast, the use of HOBr generated a variety of brominated products in addition to oxidation of the C2 position. Subsequently, Carter-Franklin and co-workers demonstrated the ability of VHPOs to catalyze the bromination and cyclization of terpenes,[26] to produce bioactive halogenated natural product. This result further supports the role of VHPOs in the synthesis of halogenated natural products.

While not the native function, VHPO's efficiently catalyze the stereospecific two-electron oxidation of organic sulfides to chiral sulfoxides.[27] Similar

asymmetric oxidations have been observed for heme peroxidases and heme chloroperoxidases with enantiomeric excesses (%ee) as high as 99%.[27]

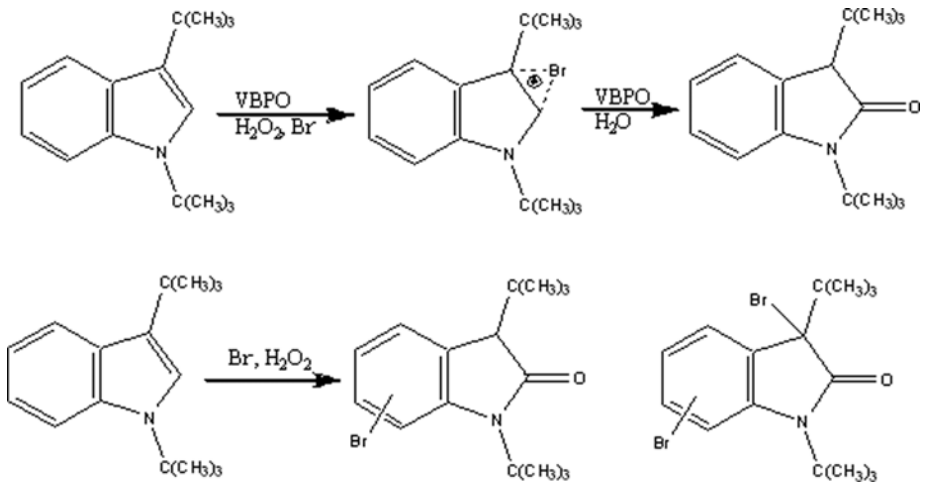

Figure 1.1: Product distribution for the bromination of 1,2-di-*t*-butylindole with VBPO and aqueous bromine with H_2O_2.[25]

However, it has been well documented that the prosthetic groups of heme peroxidases degrades due to the presence of hydrogen peroxide and eventually become fully inactivated during catalysis.[28] In contrast to their heme counterparts, VHPOs do not suffer from inactivation nor does the vanadium co-factor redox cycle during catalysis.[29] The vanadium bromoperoxidase isolated from *A. nodosum* is capable of carrying out the asymmetric oxidation of thioanisole to the (R)-sulfoxide with 91% ee.[27] Interestingly, the use of a VCPO yields a racemic mixture of sulfoxide, implicating a different substrate binding pocket between these two enzymes.[27] The ability of VBPO to carry out asymmetric sulfoxidation is consistent with its regiospecific bromination of indoles, indicating that a discrete substrate binding site exists near the vanadate. VBPOs undergo the direct oxo-transfer of an oxygen from hydrogen peroxide to the substrate, as is evident from the incorporation of ^{18}O in the products of sulfide oxidation when $H_2{}^{18}O_2$ is used as the terminal oxidant. VBPOs show considerable potential as biocatalysts because of their ability to retain catalytic activity after storage in up to 60% alcoholic solvents, to tolerate temperatures as high as 70º C, to be unaffected by detergents, and to be oxidatively robust.[27]

Structural and mechanistic aspects of vanadium-dependent haloperoxidases

The kinetics and reactivity studies discussed above raise some very interesting questions regarding the mechanism and origin of the differential activity for vanadium chloro- and bromoperoxidases. The kinetic mechanism is sequential ordered with peroxide binding occurring prior to halide.[19] Reduction of the metal cofactor leads to a reduction in activity, and slow reoxidation kinetics are observed. Isostructural analogs of vanadate will bind to the apo-enzyme but do not generate a catalytically active enzyme, thus indicating that vanadate plays more than structural role in VHPOs.[30-32]

The lack of redox cycling during catalysis clearly distinguishes VHPOs from their common heme counterparts. Heme peroxides, such as horseradish peroxidase, cytochrome c peroxidase, and chloroperoxidase, contain a ferric heme, which undergoes a two-electron oxidation with hydrogen peroxide generating an iron(IV) π-porphyrin-cation radical species (Figure 1.2). This high valent intermediate can then oxidize another equivalent of hydrogen peroxide in a catalase type reaction or can oxidize substrate molecule such as chloride. Following the oxidation of the substrate the ferric resting regenerated. This high valent iron intermediates a carry out a variety of oxidative transformations, including: the hydroxylation of aliphatic and aromatic substrates, sulfoxidations, chloride oxidation and epoxidations.[33]

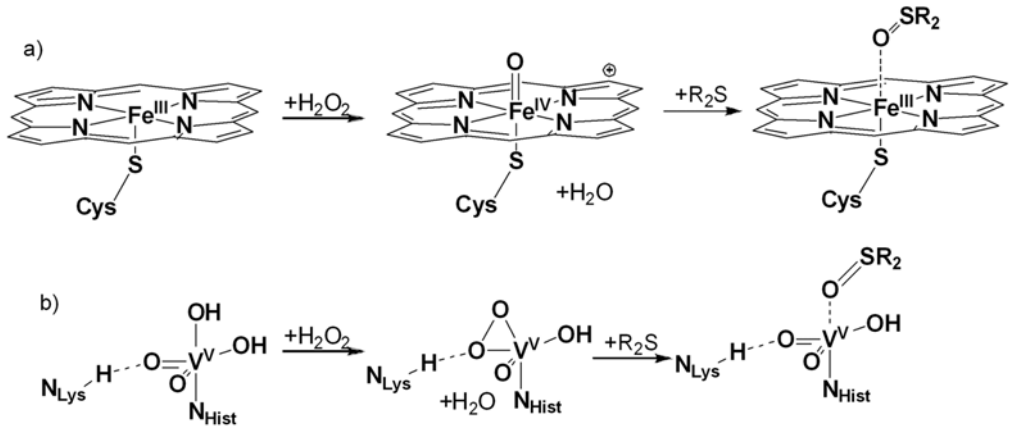

Figure 1.2: The proposed catalytic intermediates for sulfide oxidation by heme peroxidase (a) and vanadium dependant haloperoxidase (b).

A number of X-ray crystal structures are now available for VHPO,[34-37] including peroxide bound and unbound forms of a VCPO from the fungus *Curvularia inaequalis.*[36] The vanadate co-factor is covalently coordinated to an enzyme-bound histidine. The coordination geometry is trigonal bipyramidal, with an oxygen atom in the axial position trans to an N atom of histidine, and three other oxygen atoms complete the coordination sphere. The X-ray structure of the resting state of the enzyme is consistent with a trigonal bipyramidal vanadate with three equatorial and one axial oxygen atom (Figure 1.3).[38,39]

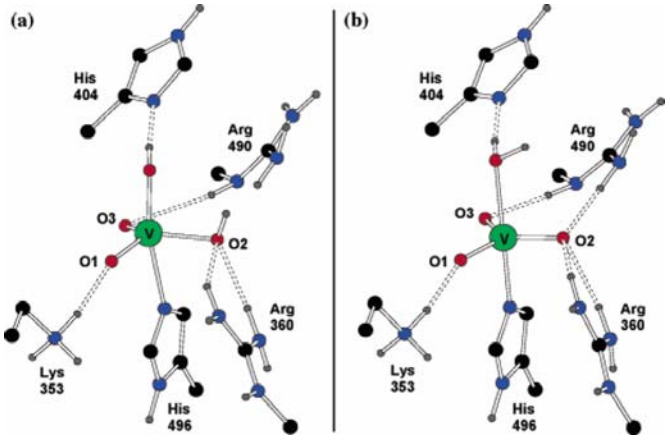

Figure 1.3: Two nearly isoenergetic active site protonation states for the resting form of vanadium-dependent chloroperoxidase.[40]

In absence of protonation or hydrogen bonding, the vandate co-factor would bear a -3 charge. This is a significant amount of charge to be confined inside of the protein active site; consequently, protonations of the co-factor and hydrogen bonding are necessary to stabilize the vanadate anion. For the VCPO isolated from *C. inaequalis*, four basic residues surround the active site, Lys353, His404, Arg360, and Arg490.[41] These residues hydrogen bond to the oxygen atoms to reduce the anionic character of the vanadate cofactor. These residues are maintained in both bromo- and chloroperoxidases. Second sphere amino acid residues appear to play a key role in differentiating the halide selectivity of VBPO. Chloroperoxidase contains a phenylalanine and a tryptophan residue, whereas the bromoperoxidase replaces these residues with a histidine and arginine respectively. Mutagenesis studies have shown that mutation of a VBPO at either,

and both, of these residues yields a marginal introduction of chloroperoxidase activity.[42] The mutagensis studies suggest that a simple increase in the hydrophobicity of active site is not solely responsible for imparting chloroperoxidase activity, thus long range interactions within the protein may contribute to the halide specificity.

The crystallographic assignment of the protonation state was one axial oxo donor with 3 equatorial hydroxos, yielding a monoanionic vanadate species. The limits of protein crystallography prevented a definitive assignment of the protonation state of the resting state vanadate co-factor. Kravitz and co-workers employed quantum chemical methods to explore the potential protonation states in the resting form of VHPO's.[43] The first set of quantum chemical models was developed from a simple vanadate with a distal imidazole. Two reasonable cationic protonation states were found to be protonated axial hydroxo or protonated equatorial oxo, yielding trioxo-aqua and dioxo-dihydroxo species, respectively.

These models provided a reasonable picture of what might occur in the active site, but did not address the complex hydrogen bonding networks provided by the enzyme. To account for these differences, QM/MM calculations were performed on a truncated protein model of a vanadium chloroperoxidase.[40] The final result showed two nearly isoenergetic structures shown in Figure 1.3. The QM/MM models showed one species in which water bound in axial position with three equatorial oxos was an energetically favorable species. It is likely that these two structures are in equilibrium within the active site, and this equilibrium may facilitate the proton transfer to nearby basic residues to assist in the coordination of hydrogen peroxide. Recently, magic angle spinning ^{51}V NMR has confirmed the protonation of the resting form of the enzyme, showing one axial and one equatorial hydroxo ion with two equatorial oxos.[44]

The peroxide-bound form of the enzyme shows a distorted tetragonal pyramidal geometry with two equatorial oxygen donors and a side-on bound peroxide moiety occupying a distal and apical position.[41] A single histidine residue is the only donor that is covalently linked to protein (Figure 1.4). The

axial position that was filled in the resting form of the enzyme is now vacant. This allows for the interaction of the halide ion with the vanadate cofactor during catalysis. X-ray absorption measurements have shown that no long-lived intermediate exists between the halide and the vanadium center, indicating that coordination of the substrate to the metal center does not occur prior to oxidation.[45] Kinetic and structural studies have provided significant insight into the potential mechanism and structure of VHPOs. The kinetic mechanism is sequential ordered, with peroxide binding first, followed by halide oxidation in a two-electron oxo-transfer step with no redox cycling of the vanadate co-factor.[46] The kinetic pH profiles indicate a kinetic pKa = 5.8 consistent with protonation of a glutamic acid or a histidine residue.[19]

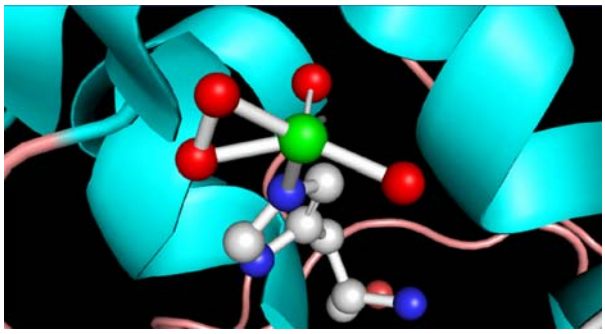

Figure 1.4: Peroxide bound vanadate co-factor at the active site of a vanadium chloroperoxidase isolated from *Curvularia inaequalis.* Oxygen = red, nitrogen = blue, carbon = grey.

Functional modeling of vanadium-dependent haloperoxidases

Small molecule mimics of an enzyme active site allow for certain types of mechanistic that are often not possible with an enzymatic system. Enzymes are often limited to aqueous buffered conditions which hinder kinetic studies involving discrete protonated intermediates. Additionally, kinetic studies with enzymes are complicated by the binding affinities for both the substrate and the product. The first functional mimic of VHPOs was simply aqueous vanadate in acidic (pH<~2).[47] Under acidic conditions, the VO^{2+} ion is the dominate form of vanadate. This simple hydrogen peroxide and vanadium oxide solution was able to oxidize bromide (and most probably iodide) but not chloride. A Schiff-base

complex of oxovanadium(V), reported in 1993, was the first coordination complex mimic of VHPOs.[48] Since then numerous other coordination complexes have been applied as functional mimics for VHPOs.[6,10,49-53]

Aqueous vanadate in acidic solutions was the first reported functional mimic of VHPOs,[47] which in the presence of hydrogen peroxide at low pH was capable of bromide oxidation and the subsequent halogenation of trimethoxybenzene. In the absence of an organic substrate, the production of singlet oxygen was observed. This is consistent with the halide-assisted disproportionation of hydrogen peroxide observed for VHPOs. The formation of a monoperoxovanadate species ($VO(O_2)^+$) was evident by the ^{51}V NMR chemical shift of -529 ppm. In addition, some diperoxo vanadate ($VO(O_2)_2^-$) was apparent during catalysis (chemical shift = -687 ppm). The starting dioxovanadium(V) species used as a pre-catalyst is regenerated upon complete consumption of hydrogen peroxide. Two critical differences exist between aqueous vanadate reactivity and VHPOs: 1) the vanadate system requires approximately 1000-fold higher proton concentration than the enzyme, and 2) the rate of halide oxidation is four orders of magnitude slower than VHPOs. This functional model supported the hypothesis that a peroxovanadate intermediate may play role in the enzymes mechanism and shows that protonation of the co-factor is involved in catalysis. It is important to note that the speciation of peroxovanadates is concentration, pH, and solvent dependent; under the conditions employed for the simple vanadate reaction the catalytically relevant species is a dimeric $(VO)_2(O_2)_3$. This is consistent with low pH being required for reactivity, because higher pH's generate $[VO(O_2)_2]^-$, a catalytically inactive species, and limit dimerization. Similar activity has been observed for peroxomolybdates and peroxotungstenates.[54] Both metals carry out the oxidation of bromide with hydrogen peroxide in acidic solutions (pH 2-4) at rates significantly faster than that observed for the corresponding vanadium system. In the case of the group VI metals, such as molybdenum and tungsten, the increased reactivity can be attributed to the higher Lewis acidity of the metal center. In contrast to the d^0 ions of group V and group VI metals, Ti(IV) has been shown to stabilize peroxide

against the oxidation of even iodide. This is consistent with the reduced Lewis acidity being correlated with reactivity.[55]

It was demonstrated that simple aqueous vanadate is capable of carrying out the oxidation of bromide. Not surprisingly, the lower rates of oxidation and the changes in catalytically effective pH indicate that the protein environment of VHPOs plays a key role in modulating the reactivity of the enzyme. Prior to the determination of the crystal structure, EPR[56] and X-ray absorption[45] spectroscopies showed multiple O and/or N donors were present within the first coordination sphere of the vanadium cofactor. A number of research groups began exploring the use of mixed O,N donor sets with a variety of ligands. A notable class of functional mimics has been developed from Schiff base type ligands. A cis-hydroxo-oxovanadium(V) complex of N-(2-hydroxyphenyl)salicylideneamine (VO(OH)HPS) was explored as a functional mimic of VHPOs (Figure 1.5).[48] In the presence of H_2O_2, this complex generates a monoperoxo species in DMF that is capable of carrying out bromide oxidation. The addition of acid generated a catalytic bromination system that was stoichiometric with respect to hydrogen peroxide. This process was demonstrated to be an electrophilic bromination of an aromatic substrate as opposed to being radical-mediated. The HPS ligand enforces the formation of a

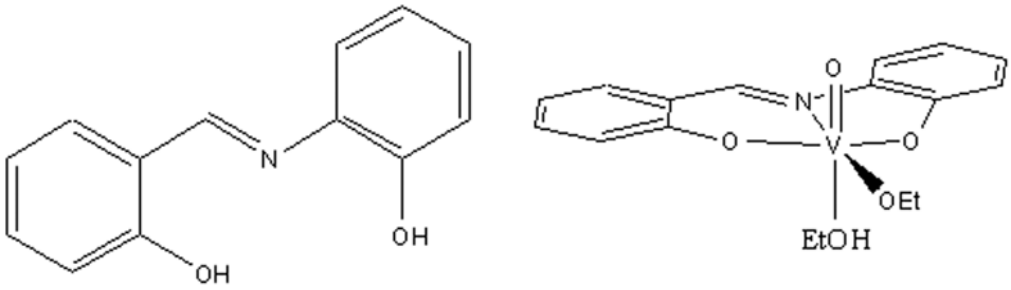

Figure 1.5: ChemDraw representation of N-(2-hydroxyphenyl)salicylideneamine and the corresponding oxovanadium(V) complex.[48]

peroxo-oxovanadium(V) species and prevents the inactivation of vanadium through the formation of diperoxovanadates.

Because the enzyme contains a distal histidine residue linking the vanadate co-factor to the protein, more structurally relevant donors sets employed ligands

derived form amino-acids were investigated.[57,58] The Schiff base generated from the condensation of salicylaldehyde and 2-aminoethylbenzimidazole generates an N_2O donor set containing one imidazole moiety (Figure 1.6).[59] X-ray structural determination showed that the ligand set binds in the equatorial plane with a cis-dioxo moiety completing the penta-coordinate structure. No peroxovanadium(V) species was isolated using this ligand set. In acetonitrile, the complex mimics the sulfoxidation activity of the enzyme, converting thioanisole to its corresponding sulfoxide in 91% yield with turnover rates (mol of product/mol of catalysts) of ≈ 30 h^{-1}. Minimal overoxidation (<3%) of the resulting sulfoxide to the sulfone was observed for this catalytic process. The proton dependence of this reaction was not explored, likely due to protonation of the Schiff base ligands. This complex demonstrates that vanadium Schiff base complexes with biologically relevant donors can carry out sulfoxidation reactions in a manner similar to that observed for vanadium-dependent haloperoxidases. The presence of aromatic donors in the Schiff base ligands, and in the case of imidazole type donors the inherent instability in the presence of acids, preclude a detailed mechanistic investigation of halide oxidation.

Non-aromatic donor sets reduce the possibility of interactions of an oxidized halide species with the vanadium complex and allow for a thorough investigation

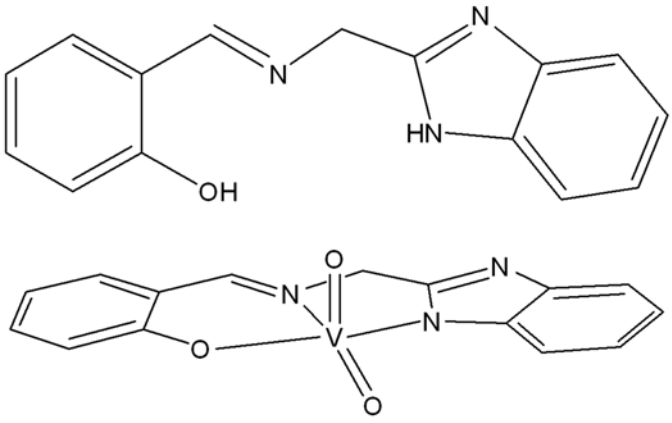

Figure 1.6: ChemDraw representation of a Schiff base ligand derived from salicylaldehyde and 2-aminoethylbenzimidazole and the corresponding cis-dioxovanadium(V) species.

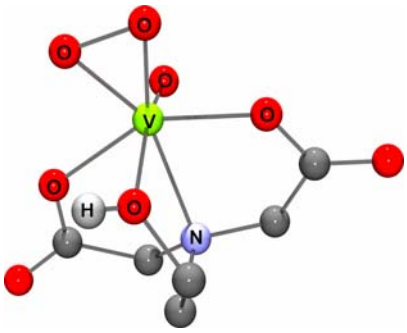

Figure 1.7: Ball-and-stick representation of the X-ray crystal structure for $K[VO(O_2)Hheida]$.[60]

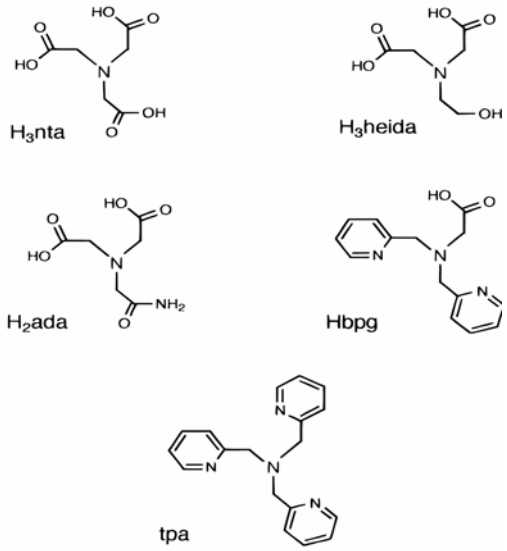

Figure 1.8: Tripodal amine ligands used in peroxide binding and substrate oxidation studies of functional models for vanadium-dependent haloperoxidases.[53,61]

of the factors controlling substrate oxidation and peroxide binding. The tripodal amine, N-2-hydroxyethyl iminodiacetate ($Hheida^{2-}$), was structurally characterized as the potassium salt of its peroxo-oxovanadium(V) complex (Figure 1.7).[60] $K[VO(O_2)Hheida$ is capable of carrying out the oxidation of bromide in the presence of hydrogen peroxide. This finding prompted the investigation of a series of tripodal amine ligand sets with varying charges and O/N donor sets (Figure 1.8) as functional models for VHPOs.[53]

It is of historical interest to note that these complexes were developed before the determination of the X-ray structure of VCPO.[34] The functional mimics retain key functionalities present in the active site structure of VHPOs; a single oxo donor, a side-on bound peroxide, and a single nitrogen donor. The difference in coordination number between the functional mimics and the active site structure is a result of the lability of the V^{+5} d^0 ion. The enzyme has the benefit of the entire protein scaffold to limit the accessibility of other donor ions to the coordinatively unsaturated vanadium. Small molecule modeling does not have this benefit, in which case it is important to fill the coordination sphere of the labile metal center to limit potential interactions of exogenous donors, which may complicate kinetics measurements.

Hamstra and co-workers demonstrated that dioxovanadium(V) complexes of the ligands depicted in Figure 1.8 were capable of coordinating hydrogen peroxide.[61] The generation of a peroxo-vanadium charge transfer band upon peroxide binding provides a clean spectroscopic handle to monitor the kinetics of this process. The kinetic profiles generated were fit to a pre-equilibrium model in which formation of a $VO(O_2)L$-H_2O_2 complex precludes the formation of $VO(O_2)L$. Peroxide coordination was found to be first order in peroxide concentration with second-order rate constants ranging between 0.12 – 0.33 M^{-1} s^{-1} depending on the identity of the ligand set. The importance of protonation in the catalytic cycle for VHPOs is alluded to by the acidic pH necessary for reactivity. The rate of peroxide coordination to tripodal amine complexes of dioxovanadium(V) increases in the presence of up to one equivalent of a strong acid. This kinetic information demonstrates that peroxide binding is a pH-assisted step. Based on this, a mechanism for peroxide binding was proposed in which protonation of an oxovanadium bond labilizes the oxo for the subsequent addition of H_2O_2 (Figure 1.9). [61]

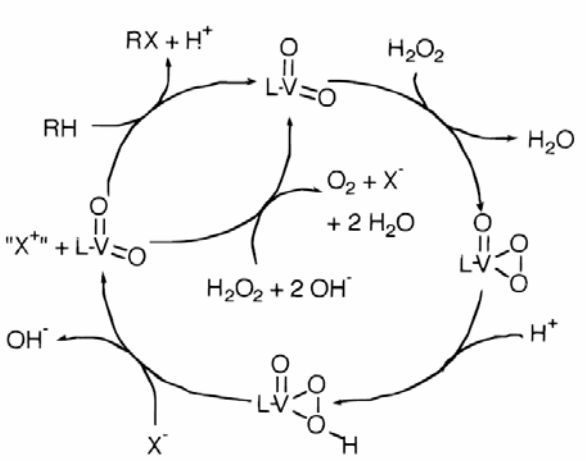

Figure 1.9: Proposed mechanism for halide oxidation by functional models of vanadium-dependent haloperoxidases.[53,61]

Having established a reasonable mechanism for peroxide binding, Colpas and co-workers explored the reactivity of the aforementioned tripodal amines with respect to halide oxidation.[53] The importance of protonation to catalysis became evident in the oxidation of bromide, in which proton per bromide ion was absolutely necessary to observe reactivity. In the presence of an aromatic or olefinic substrate for electrophilic aromatic substitution, the proton dependence was one proton per vanadium for the maximum rate of halide oxidation. These two observations led to the hypothesis that protonation of the vanadium complex generates the catalytically active vanadium species.[53] In the absence of an organic substrate, a second equivalent of proton is required to neutralize the generated hydroxide. In addition to the kinetic observations of proton dependence, in the absence of substrate there is an observable shift of the peroxo-vanadium-charge transfer band in the visible spectrum. It is important to note that these complexes are only catalytically active in organic solvents. In most cases the reactivity studies were carried out in acetonitrile.

While these complexes efficiently perform bromide and iodide oxidation, they are incapable of carrying out chloride oxidation. The basis for explaining this discrepancy in the reactivity was that the apparent pKa's in acetonitrile for the protonated vanadium species (pKa = 5.4-6.0) were lower the apparent pKa's of chloride (pKa = 8.9) and bromide (pKa = 5.4).[53] In the case of chloride, the

anionic substrate is a strong enough base in acetonitrile to deprotonate the activated vanadium complex, thereby shutting off reactivity.[53]

In addition to mimicking the oxidation of halides by VHPO, the aforementioned tripodal amine complexes are capable of oxidizing thioethers.[62] The complicated proton dependence for halide oxidation results from the apparent basicity of halides compared to the basicity of the peroxovanadium catalysts. Because thioethers are neutral substrates, the effects of apparent pKa's on reactivity are limited. Smith and co-workers demonstrated that K[VO(O_2)Hheida] is capable of oxidizing thioethers with rates exceeding that observed for VBPO or any other reported thioether oxidation catalyst (Table 1.1). Additionally, thioether oxidation has an absolute dependence on the presence of a proton for the oxidation to occur. The maximal rate for thioether oxidation is observed at 1 eq. of H^+ per vanadium; additional equivalents have no affect on the rate of substrate oxidation up to the point where complex decomposition becomes dominant. These results provided a confirmation of the two-fold role that protonation plays in the catalytic cycle for VHPOs, where: 1) peroxide coordination is a proton-assisted step, and 2) protonation of the peroxo intermediate is necessary to activate the complex to carry out substrate oxidation. These studies showed that K[VO(O_2)Hheida] is a complete functional mimic of vanadium-dependent haloperoxidases mimicking the peroxide coordination, halide oxidation, and thioether oxidation observed with the enzyme.

Based on the peroxide binding studies, kinetics of bromide oxidation, and shift in the charge-transfer band upon protonation, a mechanism was proposed in which a hydroperoxo oxovanadium(V) is responsible for substrate oxidation (Figure 1.9). This proposal provided significant insight into the importance of the catalytically relevant pKa of VHPOs. Additionally, this mechanism differs dramatically from typical heme peroxidases in which the iron center starts in the +3 oxidation state and then forms a high-valent iron-oxo species through heterolytic cleavage of hydrogen peroxide, which subsequently carries out the oxidation.

Table 1.1: Reported turnovers and time for a variety of sulfide oxidation catalysts.

System	Oxidant	Substrate	Max. Turnovers (time = h)	pseudo-first order k, s^{-1}	corrected or second order k, M^{-1} S^{-1}
K[VO(O_2)(Hheida)]	H_2O_2	PhSMe	950 (3)	2.00 x10^{-3}	8.1
K[VO(O_2)(Hheida)]	H_2O_2	PhSEt	950 (3.5)		
VBPO (A. nodosum)	H_2O_2	PhSMe	520 (20)		
VBPO (C. pilulifera)	H_2O_2	PhSMe	450 (20)		
VCPO (recomb.)	H_2O_2	PhSMe	560 (20)		
Kagan-modified Sharpless reagent (Ti/diethyltartrate)	t-BuOOH	PhSMe	20 (3)		
VO($acac)_2$	H_2O_2	PhSMe			2.9
VO($OEt)_3$	t-BuOOH	Bu_2S			6.1 x 10^{-3}
(VO(O-i-$Pr)_3$ + diethyltartrate	t-BuOOH	pTolSMe	1 (6)		
(VO(3-MeOSal-RR-chxn)	CmOOH	PhSMe	10 (37)		
VO(sal-L-ala)(OMe)(MeOH)	t-BuOOH	PhSMe	10 (5.5)		
(VO($acac)_2$ + chiral shed L)	H_2O_2	PhSMe	100 (16)		
VO(O-i-$Pr)_3$ + chiral shed L	H_2O_2	PhSMe	73 (13)		
VO_4^{3-} substituted phytase (A. ficuum)	H_2O_2	PhSMe			0.13
K[VO(O_2)(dipic)]	H_2O_2	$[(en)_2Co(SCH_2CH_2NH_2)]^{2+}$	0.1	4.0 x 10^{-9}	8 x 10^{-4}

Proposed Mechanism of Vanadium-dependent Haloperoxidases based on biochemical and functional modeling studies

Biochemical and functional modeling studies have provided a wealth of information into the mechanism of this novel class of haloperoxidases. A number of mechanisms have been proposed for VHPO, and these generally involve an oxo-transfer process, where vanadium acts as a Lewis acid that activates hydrogen-peroxide for its subsequent addition to the substrate. Isotope labeling studies of peroxide illustrated that an oxygen atom derived from hydrogen peroxide is transferred to the substrate, but do not identify the catalytically active intermediate, nor do they account for the role of protonation in activating the peroxo-cofactor. Computational methods have been employed to address these questions using truncated *in silico* models of VHPO.[63] Two oxo-transfer reaction pathways involving either the equatorial or the axial peroxo oxygen atom using two typical VHPO substrates, Br^- and dimethylsulfide (DMS), were explored. In addition, two potential protonation states of the peroxovanadate co-factor may exist, a neutral form and an anionic form. The reaction pathways for the attack of Br^- on both the peroxo oxygen atoms of the anionic form have very large potential energy barriers, as expected considering that it is a reaction between two anionic species. A similar observation was made for the neutral substrate, DMS. The computed potential energy barriers for the nucleophilic attack of the substrate on the pseudo-axial and equatorial peroxo oxygen atoms were lower (21.2 and 29.8 kcal mol^{-1}, respectively). In contrast, energy barriers computed for the reaction between Br^- or DMS and the neutral species, showed that the oxo-transfer step involving the pseudo-axial peroxo atom is more favored than the corresponding equatorial pathway for both substrates. The transition state resembles a classic S_N2 mechanism, in which the attack of the nucleophile and cleavage of the O-O bond are simultaneous (Figure 1.10).[63]

On the basis of these results, it was concluded that the oxo-transfer reaction path involves the unprotonated axial peroxo oxygen atom. Moreover, protonation of the peroxo moiety plays a crucial role in the activation of peroxo-vanadium complexes. In this context, it is noteworthy that in the peroxide-bound form of the

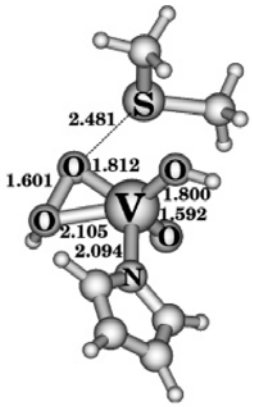

Figure 1.10: Transition state calculated for dimethyl sulfide oxidation by *in silico* models of VHPO.[63]

enzyme a lysine residue (K353) is hydrogen bonded to the equatorial oxygen atom of the peroxo group,[36] suggesting that this amino acid might play a role similar to H^+ in peroxide activation. A methyl ammonium group was employed in the computational model as a hydrogen bond mimic for the equatorial peroxo oxygen atom of the cofactor. Results indicated that a polarizing group such as CH_3-NH_3^+ plays a role, albeit less dramatic than protonation of the peroxo moiety, in the activation of the peroxo form of the cofactor. The barrier to activation for bromide oxidation in this case is 10.2 kcal mol^{-1}.[63] These computational studies are in full agreement with reported catalytic abilities of both the enzyme system and functional models, and address the role of protonation in the catalytic cycle for VHPOs. As these models only account for the activity of the coordinatively unsaturated active site of the enzyme system, this leaves questions whether the functional mimics discussed above are true functional models, i.e., do they proceed through the same type of transition state to carry out substrate oxidation?

Metal-based oxidation catalysts utilizing peroxides

A wide variety of transition metal-catalysts are utilized for oxidative transformations in both academia and industry. Transition metals are activated by, or serve to activate a terminal oxidant, such as dioxygen, superoxide, radicals,

and peroxides. This section will focus on the general mechanism of d^0 transition-metal catalyzed oxidations with peroxides and the application of asymmetric oxidation catalysts for epoxidations and sulfoxidations.

Early transition metals, such as molybdenum(VI), tungsten(VI), titanium(IV) and vanadium(V), form stable peroxide compounds capable of carrying out a variety of oxidative transformations. The group VI transition metals form a variety of stable peroxo species.[64] For the purposes of this introduction, the mechanistic conclusions applied to molybdenum are also applicable to the tungsten system; however, it is important to note that differences in the speciation and acidity of these two metal ions can lead to minor variations in the reactivity. Aqua diperoxo molybdenum species are typically seven-coordinate with pentagonal bipyramidal with an oxo donor and a trans ligand filling the axial positions.[65] Aqua-bridged dimers of diperoxo molybdenum species are well known[64] and are believed to be one of the forms responsible for the stoichiometric and catalytic alcohol oxidation and alkene epoxidation in halocarbon solvents.

An important class of dimeric polyoxo molybdenum and tungsten peroxo complexes was first prepared by Mimoun in 1969.[66] The $[M_2O_3(O_2)_4(H_2O)_2]^-$ species can be isolated from basic hydrogen peroxide solutions treated with MO_3. A large number of analogous compounds with varying monodentate and bidentate ligands have since been reported. The neutral and monoanionic species with the appropriate counterion are readily soluble in both polar and non-polar solvents, and have been widely used as both stoichiometric and catalytic oxidants in organic chemistry.[64] The neutral hexamethylphosphoric triamide complexes of both molybdenum and tungsten diperoxo species, were extensively studied for their alkene epoxidation[67-71] and sulfide oxidation[72] abilities. The tungsten complex has a greater catalytic efficiency for sulfide oxidations by H_2O_2 in the presence of a strong acid, whereas in the absence of acid the molybdenum complexes show a higher rate of epoxidation[70,73] and sulfoxidation.[74,75] This difference in reactivity can be attributed to the differences in Lewis acidity of molybdenum and tungsten, where the harder lewis acid, molybdenum, forms a stronger coordination bond with the dianionic peroxo moiety, thus activating it for

the oxidation of a nucleophile in the absence of acid.[65] In the presence of acid, the tungsten bound peroxide has a higher basicity do to the weaker coordination thereby facilitating the formation of a hydroperoxo species that is activated for substrate oxidation.

The mechanism of epoxidation and sulfoxidation by group VI polyoxoanions was proposed to undergo two potential mechanisms, coordination of the substrate to the metal center followed by an insertion of the peroxo moiety[67] or the direct nucleophilic attack of the substrate on coordinated electrophilic peroxide.[71,76] The use of $H_2{}^{18}O_2$ and M=^{18}O confirmed that the substrate incorporated oxygen is derived exclusively from hydrogen peroxide lending credence to the nucleophilic attack mechanism which is similar to what has been proposed for VHPOs. As was observed for functional models of vanadium-dependent haloperoxidases, the rate of epoxidation and sulfoxidation with group VI monoperoxo and diperoxo species is enhanced in the presence of acid.[54,65,72] This effect was attributed to generation of a neutral metal complex that can lead to a more electrophilic hydroperoxo moiety. Computational studies have shown the transition state for epoxidation to involve nucleophilic attack of the olefin on the unprotonated oxygen of a hydroperoxo moiety (Figure 1.11).[77]

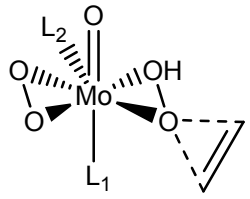

Figure 1.11: Representative transition state for the epoxidation of ethylene by a $MoO(O_2)_2L_2$ complex.[77]

Polyoxometallates of group VI metals are an important class of epoxidation catalysts. The polyoxoanions of molybdenum and tungsten form oxobridged clusters that in the presence of hydrogen peroxide can carry out a wide variety of oxidations. Under typical reaction conditions (high concentrations of hydrogen peroxide in an acidic solution), polyoxometallates dissociate into monomeric/dimeric species that are the proposed catalytically relevant

oxidants.[64] Transition-metal-doped polyoxometalles have been employed to carry out stereoselective oxidations in which the polyoxometallate serves as a solid support to reduce the conformational flexibility in the transition state for the covalently linked transition metal.[78]

No discussion of transition-metal-catalyzed oxidations is complete without addressing the Nobel-prize-winning work of K. Barry Sharpless. Sharpless systems generate an *in situ* chiral complex of (+) or (-)-diethyl tartrate and titanium(IV) tetraisopropoxide.[79] Group VI and vanadium-based catalysts generate a peroxo-oxometal complex that carries out the reaction without coordinating the substrate to the metal center. In contrast, titanium complexes do not have an oxo donor and rely on a coordinatively unsaturated metal complex to chelate the allylic alcohol.[80] Sharpless showed the titanium(IV) (+)diethyl tartrate complex with *t*-butylhydroperoxide to be an effective asymmetric epoxidation catalyst for a variety of allylic alcohols with enantiomeric excesses (%ee) greater than 90% and an overall yield of >70%. As mentioned previously, titanium(IV) peroxide complexes are typically inactive with respect to nucleophilic oxidations. The use of organic peroxides provides a more activated peroxo moiety capable of carrying out the two-electron oxo-transfer process by polarizing the peroxo bond. The success of Sharpless-type catalysts is evident from the commercial synthesis of both enantiomers of glycidol, an important chiral building block.[9]

Henri B. Kagan pioneered the application of titanium(IV) diethyl tartrate systems to the asymmetric oxidation of thioethers.[81] Given the accepted nucleophilic oxidation mechanism for Sharpless epoxidation, the oxidation of other nucleophilic substrates is not surprising. As is the case for Sharpless epoxidation, the sulfoxidation reaction explored by Kagan and co-workers requires the use of organic peroxides to obtain high enantioselectivities. Typical reaction conditions employ halocarbon solvents, commonly dichloromethane or 1,2-dichloroethane, and cumylhydroperoxide as the terminal oxidant. In the case of alkyl aryl sulfides, such as *p*-tolyl methyl sulfide, the sulfoxidation reaction can generate enantiomeric excesses as high as 99%.[82] In contrast to the Sharpless

epoxidation system, the Kagan methodology for sulfoxidation employs a biphasic reaction system. Water is added dropwise after the *in situ* generation of the catalyst to limit hydrolysis of the titanium(IV) tetraisopropoxide starting material, which may generate reactive oligomers.

The titanium(IV) diethyl tartrate systems have proven to be effective catalytic systems for asymmetric epoxidation of allylic alcohols and sulfoxidations. The requirement of the Sharpless system for a hydroxyl group proximal to the double bond limits its application to unsubstituted or terminal alkenes. The use of reduced salen ligands partially alleviated this substrate restriction. Reduced Schiff-base ligands provide an aromatic platform to interact with the substrate as well as providing hydrogen bond donors adjacent to the metal center. In contrast to the Sharpless and Kagan-modified system, Ti^{IV}(salan) systems form isolable *μ*-oxobridged dimers and are competent epoxidation catalysts using hydrogen peroxide.[83,84] Computational studies have suggested that the presence of a strong hydrogen bond between the secondary amine of the ligand and an *η*-peroxide serves to activate the peroxo moiety for nucleophilic attack by the substrate (Figure 1.12).[85]

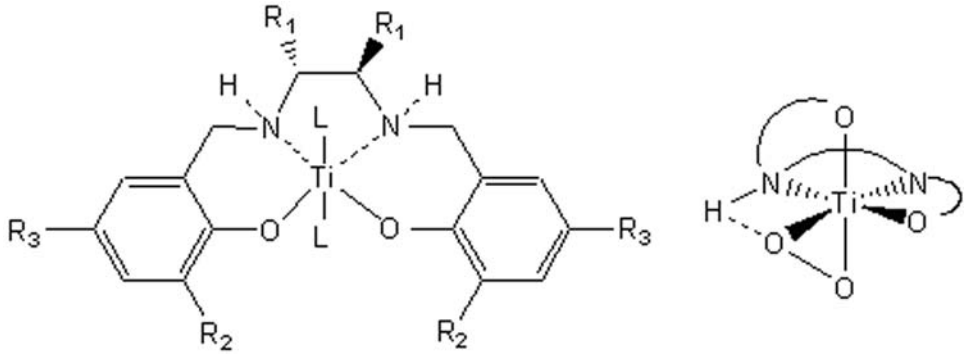

Figure 1.12: Reduced schiff base ligand applied to the asymmetric epoxidation of terminal olefins with hydrogen peroxide (left). Proposed hydrogen bond formed to activate η^2-peroxo moiety for nucleophilic attack (right).

Enantiomeric excesses show a strong dependence on substrate concentration and range from 70%-97%. Unlike the Sharpless system, the substrate interacts non-covalently with the hydrophobic ligand set, which in turn, leads to facial selectivity for the epoxidation.

Prior to the exploration of titanium(IV)-salen complexes, Kochi and co-workers demonstrated that Mn^{3+}(salen) complexes were capable of carrying out olefin epoxidation.[86] Jacobsen and co-workers and Katsuki and co-workers modified the manganese-salen complexes to carry out asymmetric epoxidations.[87,88] The condensation of cis-1,2 cyclohexyldiamine with a substituted salicylaldehyde generates the Schiff-base ligand utilized in the Jacobsen epoxidation system (Figure 1.13).[87]

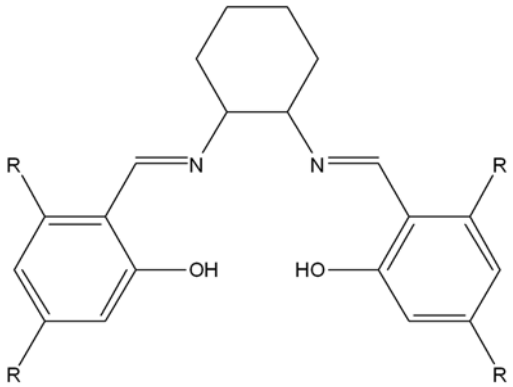

Figure 1.13: The Schiff-base ligand architecture used in Jacobsen-type catalysts

In contrast to the group VI and titanium-based systems, the Jacobsen-type system can utilize a variety of terminal oxidants including hypochlorite, iodosylbenzene, molecular oxygen, monoperoxysulfates and peracids.[89-92] The choice of terminal oxidants in Jacobsen catalysts dramatically effects the regio- and stereoselectivity in the oxidation of 1,3-dienes.[93] This indicates that multiple oxidation pathways may exist. Jacobsen systems are capable of the stereoselective epoxidation of a wide variety of alkenes, including: *cis*-alkenes, conjugated Z-enynes, acyclic conjugated polyenes, cyclic dienes, heterocyclic enamines, cinnamate esters, tri and tetra-substituted alkenes, and enol ethers. The substrate scope of this catalyst far exceeds that of the Sharpless system, but the stereoselectivity of Jacobsen epoxidations vary greatly depending on the identity of the substrate and the choice of terminal oxidant.[94] The stereoselectivity of this reaction arises from the chirality of the diamine backbone and the subsequent non-covalent interactions with the alkene. The identity of

active oxidants is highly debated, and proposals have indicated a variety of high-valent Mn=O, μ-oxo bridged dimer, peracid and hydroperoxo species.[95] As previously mentioned, the nature of the terminal oxidant employed can affect the identity of the active oxidant. For most cases it is generally believed that a high valent Mn=O species is responsible for catalysis, and reaction proceeds via an oxygen rebound mechanism, originally proposed by Groves and co-workers for Mn-porphyrin systems.[96] Jacobsen systems differ dramatically from group VI, titanium(IV) and vanadium(V) systems because a manganese-centered oxidation plays a critical role in catalysis.

A wealth of literature exists for the application of metal-based oxidants to oxidative catalysis. Group VI metals constitute an important class of peroxo-type oxidation catalysts that provide interesting parallels with vanadium(V)-type systems. The molybdenum and tungsten systems form stable diperoxo-oxo species for which the epoxidation rate is enhanced by the addition of acid. Titanium systems, on the other hand, require the use of an organic peroxide to activate the O-O bond for epoxidation. Finally, the Mn(salen)-type systems can utilize a wide variety of terminal oxidants and consequently can tune their reactivity to a particular class of substrate.

Peroxovanadium(V) complexes as oxidation catalysts

Vanadium oxides have been employed in a wide range of catalytic oxidations ranging from alkane oxidation[10] to the industrial desulfurization of crude oil streams.[12] As the focus of this thesis is on peroxo-vanadium complexes, this section will discuss the varied activity of vanadium peroxide complexes in oxidative transformation.

Peroxovanadium(V) compounds carry out a rich and diverse variety of net two-electron oxidations. Alkenes and allylic alcohols can be epoxidized and hydroxylated, sulfides can be oxidized to sulfoxides and sulfones, benzene and other arenes can be hydroxylated, halides are oxidized, and primary and secondary alcohols are oxidized to aldehydes and ketones, respectively.[10]

Vanadium(V) forms stable and in some cases isolable mono and diperoxo species with the peroxide bound in a η^2-fashion. One example of a *t*-butylperoxo complex exists with the tridentate ligand, dipiciolinate (Figure 1.14).[97] In all known peroxo-oxovanadium(V) complexes the V=O bond occupies an axial position, and the peroxide binds side-on in the equatorial plane. Diperoxo-oxovanadium(V) complexes usually form pentagonal bipyramidal geometries with both peroxo donors in the equatorial plane with two exogenous donors coordinating trans and cis to the oxo bond. In acidic solutions, vanadium(V) exists as the VO_2^+ ion. Addition of hydrogen peroxide yields both monoperoxo and diperoxo vanadium species, with the monoperoxo form dominates at pH < 2.[98] In organic solutions, the monoperoxo complex is favored at low concentrations of hydrogen peroxide. The aqueous speciation has important implications for the synthesis of vanadium coordination compounds that are performed in aqueous solutions using a potassium vanadate salt as the

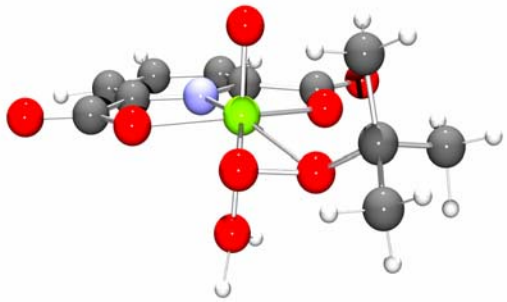

Figure 1.14: Ball-and-stick representation of VO(*t*BuOO)(dipic)[97]

metal source. Vanadium(V) complexes are diamagnetic and therefore amendable to ^{1}H and ^{13}C NMR. In addition, the I=7/2 ^{51}V nucleus is 100% istopically abundant, allowing for the application of ^{51}V NMR. These spectroscopic tools allow for detailed mechanistic studies of the active oxidant.

The choice of vanadium salt used to generate the catalytically active species can have a profound effect on the reactivity of the complex. Kinetic studies have shown that the oxidation of vanadium(IV) to vanadium(V) by hydrogen peroxide proceeds via a radical-mediated process that generates free hydroxyl radicals in solution.[99] It is proposed that an organic peroxide-derived radical is responsible for the hydroxylation of arenes with *t*-butylhydroperoxide and some epoxidation

reactions when using oxovanadium(IV) acetylacetonate ($VO(acac)_2$). Interestingly, the use of peracids with $VO(acac)_2$ for epoxidation of geraniol, leads to selective epoxidation of the electron rich terminal alkene.[100] Generally, peroxo-oxovanadium(V) complexes undergo two electron oxidations; however, it can function as a one electron oxidant in cases where no two-electron pathways are available. In the case of the conversion of 2-propanol to acetone, the proposed mechanism involves hydrogen atom abstraction from the C2 position by the coordinated peroxide and the subsequent release of a hydroxyl radical to generate a cis-dioxovanadium(V) species.[101] Primary and secondary alcohols require the use of hydrogen peroxide to initiate the reaction; in contrast, benzylic alcohols are converted to their aromatic ketones under aerobic conditions via radical mediated hydrogen abstraction by vanadium(IV).[102]

Two-electron oxidation pathways dominate the reactivity of peroxo-oxovanadium(V) species. The most common two-electron oxidations are the oxidation of halides, epoxidations and sulfoxidations.[10] As halide oxidations have been discussed in detail above, this section will focus on the latter two. The use of chiral hydroxyamic acid ligands with oxovanadium(V) trialkoxides gives rise *in situ* to a chiral epoxidation catalysts capable of transforming allylic alcohols to chiral epoxides with enantioselectivities up to 50%.[14] This work was initially pioneered by Sharpless and co-workers, who proposed a mechanism similar to that of the titanium(IV) diethyl tartrate catalysts, in which the allylic alcohol coordinates to the vanadium center, and oxygen atom transfer occurs by nucleophilic attack of the olefin on the coordinated peroxide. A significant limitation of this initial work was the large excess of ligand (5 molar equivalents) for asymmetric induction. Yamamoto and co-workers expanded on this initial work with vanadium-based asymmetric epoxidations by using axially chiral hydroxyamic acids.[103] In contrast to Sharpless' attempts, the Yamamoto systems only required a 1.5 molar equivalents of ligand to effectively perform asymmetric epoxidations with %ee as high as 96%. Both systems employed the use of organic peroxides such as *t*-butylhydroperoxide and triphenylmethyl hydroperoxide and required low temperatures (-20 C) and long reaction times (2-

3 days). The requirement of excess ligand stems from the *in situ* formation of the catalysts from oxovanadium(V) triisopropoxide. At 1:1 concentrations of ligand to metal, two species are evident in the ^{51}V NMR, one being attributed to the 1:1 metal ligand complex with two isopropoxide donors coordinated, and the second being $VO(O\text{-}i\text{-}Pr)_3$. The excess of ligand is necessary to drive the formation of the chiral complex. Sharpless' vanadium epoxidation system shows a decrease in the enantioselectivity with ligand equivalents greater than five; the inverse relationship is true for the Yamamoto derivatives. This difference likely stems from the ability of the hydroxamic acid to form a bis-complex, which may eliminate the vacant coordination site necessary for binding of an allylic alcohol. The chiral hydroxamic acids employed by Yamamoto and co-workers are significantly sterically encumbered, which may hinder the formation of the bis complex.[103]

As was the case for the titanium(IV)-based Sharpless system, the vanadium(V) hydroxamic acids were only capable of stereoselectively oxidizing allylic alcohols. Efforts were made to expand the scope of these vanadium-based epoxidation systems to non-functionalized alkenes. Tridentate Schiff base ligands (H_2HPS) and alkyl peroxides were shown to stereoselectively epoxidize olefins.[48] The reactivity of this catalytic system increases with enhanced nucleophilicity of the alkene and is sensitive to steric hindrance of the alkene. This observation is consistent with nucleophilic attack of the double bond on an electrophilic peroxo moiety coordinated to the vanadium.

The success of Sharpless type and related catalysts for allylic epoxidation, pre-empted a surge of asymmetric catalysis research. One functionality that has become particularly interesting over the past decade is the chiral sulfoxide.[104] Chiral sulfoxides are important synthetic and pharmaceutical targets.[104] A number of organometallic reactions use chiral sulfoxides as stereoselective directing agents. With the release of omeprazole, a gastric proton pump inhibitor containing a chiral sulfoxide, pharmaceutical manufacturers marketed a variety of chiral sulfoxide-containing derivatives. Current synthetic approaches

towards asymmetric sulfoxides often use nucleophilic attack on a sulfinyl starting material or asymmetric oxidation of the sulfide precursor.[104]

Vanadium coordination complexes are effective sulfoxidation catalysts, and attempts to develop asymmetric sulfoxidation catalysts have met with varying degrees of success. $V^{IV}O(acac)_2$ in dioxane/ethanol solutions oxidizes *p*-chlorophenylmethyl sulfide by hydrogen peroxide.[105] This reaction proceeds nearly quantitatively. At high concentrations of hydrogen peroxide the rate of sulfide oxidation decreases, which is consistent with the formation of the less reactive diperoxo-oxo species. The rate of sulfide oxidation is also dependent on the identity and concentration of the alcohol introduced to the solution. Modena and co-workers rationalized this rate dependence in terms of the increasingly acidic alcohols assisting in an O-O bond breaking step.[105] Given the accessibility of one-electron oxidations with vanadium(V)-peroxo complexes, two potential mechanisms become evident: 1) a radical-mediated process and 2) an electrophilic oxo-transfer mechanism. These two mechanistic pathways can be differentiated by the preferential oxidation of sulfides over sulfoxides. An electrophilic mechanism will show a preference for sulfoxide formation where a radical-mediated step will show a preference for sulfone formation. Functional models of VHPO and the enzyme itself undergo an electrophilic oxidation mechanism that preferentially oxidizes sulfides to sulfoxides without generating a significant quantity of sulfone. An interesting exception to this reactivity is provided by $VO(O_2)$(picolinate), where both mechanisms contribute to the observed sulfoxidation reactivity as evident by the formation of both disulfoxide and sulfone products when thianthrene 5-oxide is used as a substrate (Figure 1.15).[106] This exception to general reactivity of peroxo-oxovanadium(V) complexes is explained by the ability of $VO(O_2)$(picolinate) to be reduced to a radical anion. It is important to keep in mind when designing new catalysts that radical-mediated pathways may be involved in oxidation or in complex degradation.

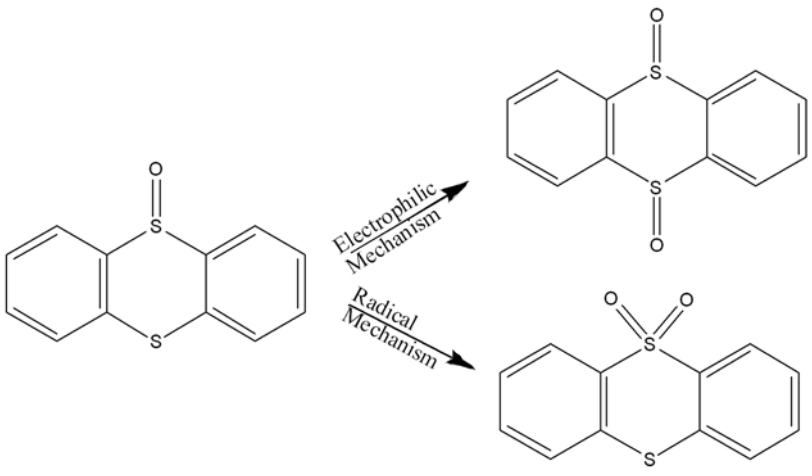

Figure 1.15: Thianthrene 5-oxide as a mechanistic probe for electrophilic versus radical oxidation mechanisms.

Much of the vanadium-based asymmetric sulfoxidation research has focused on the application of the Bolm-type system, which utilizes chiral Schiff base ligands (Figure 1.16).[107] These conditions typically involve a chiral Schiff base derived from an amino alcohol and salicylaldehyde, the most effective of which is the Schiff base generated from *tert*-leucinol and 3,5-di-*tert*-butylsalicylaldehyde. Similar to the Sharpless methodology, the ligand is added in a marginal excess with an oxovanadium(IV) salt (typically vanadyl acetylacetonate) to generate the catalysts *in situ*. In a simple hydrogen peroxide/chloroform mixture this system affords an 85% enantiomeric excess for the oxidation of thioanisole. These remarkably simple reaction conditions have led to a wealth of research involved in optimizing the conditions for a variety of thioether oxidations.

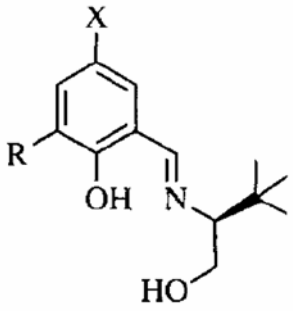

Figure 1.16: Schiff base ligand originally employed by Bolm et. al for asymmetric sulfide oxidation with vanadium.[107]

This work was expanded upon by Blum and co-workers in 2003, where a mechanistic investigation of oxidation of di-*t*-butyl disulfide was performed.[108] This study highlighted some important aspects of the biphasic reaction conditions and its affect on the enantiomeric excess of the reaction. In the presence of excess hydrogen peroxide it is possible for vanadium(V) to coordinate additional equivalents of peroxide, thereby generating a non-selective oxidant. The enantiomeric excess of disulfide oxidation was found to track with the miscibility of the organic solvent and water. The original biphasic reaction conditions reduce the amount of peroxide present in the organic phase, thereby limiting the generation of a non-selective oxidant. Slow addition of aqueous hydrogen peroxide afforded enantiomeric excess up to 97% for disulfide oxidation. A precise determination of the non-selective oxidant was not performed, but the ^{51}V NMR suggests the presence of a diperoxo-vanadium(V) species.

In addition to the experimental work performed on this system, a QM/MM investigation of the factors controlling the enantioselectivity of disulfide oxidation was performed by Balcells and co-workers.[109,110] This systematic computational analysis showed that there are four possible transition states arising from two coordination modes of the ligand to vanadium(V). The transition states are S_N2-like oxo-transfer processes in which a side-on bound hydroperoxide transfers the unprotonated oxygen to the substrate. The enantioselectivity of this reaction is governed by the sterically hindered approach of the thioether towards the hydroperoxo moiety of the active catalysts. The stereochemical preference of the reaction is governed by two factors: 1) the diastereomeric identity of the vanadium complex and 2) the approach of the sulfide. These two factors are modulated by the identity of the substituents at R_1 and R_3 in Figure 1.17. R_3 limits the ring conformations accessible to the 5-membered chelate ring upon binding to vanadium, thereby providing an energetic preference for one of the diastereomeric coordination modes. R_1, on the other hand, limits the rotational confirmations accessible to the approaching disulfide. These computational

results explain the experimental observation that the identity of R_1 and R_3 greatly influence the stereoselectivity of the reaction whereas R_2 has relatively little affect.

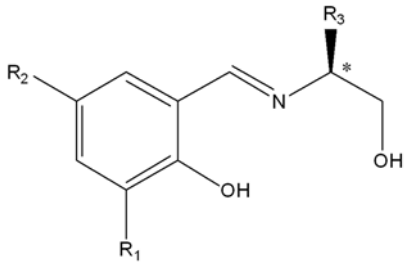

Figure 1.17: Schiff base ligand commonly employed for asymmetric sulfoxidation. Generic R groups indicate sites of derivatization explored computationally to enhance stereoselectivity.[110]

Oxovanadium complexes using tripodal-amine derivatives have also been employed to carry out the asymmetric oxidation of thioethers in the presence of organic peroxides (Figure 1.18).[49,111] Unlike the Bolm protocol, these oxovanadium(V) complexes are isolated as the oxo-alkoxo species and then introduced into dichloroethane for catalysis. The X-ray crystal structure of the isolated oxovanadium(V) complex shows that the tripodal amine coordinates in a tridentate fashion, with one chelate arm twisted away from the metal center (Figure 1.18a).[49] The enantiomeric excess for these systems is marginal, 37.9% for the oxidation of thioanisole and 36.7% for the sterically encumber benzyl phenyl sulfide. The reduced enantiomeric selectivity of these systems is likely due to the conformational flexibility of the ligand system, which allows for a variety of diastereomeric vanadium species to form. DFT calculations suggest a high degree of flexibility with the end-on bound cumyl peroxide group, which may also contribute to a reduction in the stereoselectivity of the reaction.

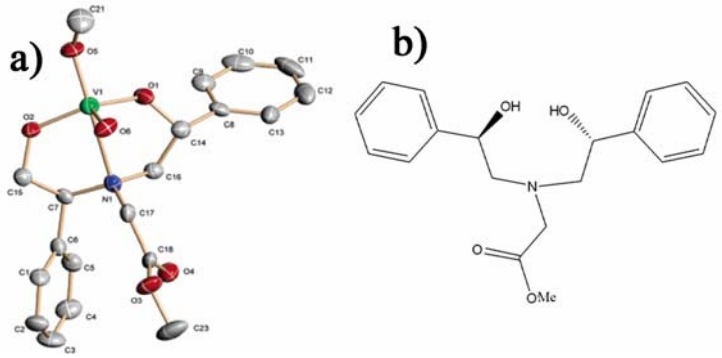

Figure 1.18: (a) Ortep diagram at 50% probability of a methoxo-oxovanadium(V) complex with a chiral tripodal amine ligand. (b) Tripodal amine ligand derived from glycine and (S)-styrene oxide.[49]

Scope of this Work

Functional mimics for vanadium-dependent haloperoxidases provided significant insight into the proton dependence of the reactivity as alluded to by the catalytically relevant pKa = 5.8 for the enzyme. Protonation plays a dual-fold role in catalysis by assisting in both the coordination of hydrogen peroxide and activating the peroxo-vanadium species for catalysis. Quantum chemical models of the active site have suggested that a strong hydrogen bond from a nearby basic residue polarizes the peroxide bound vanadate co-factor, thereby activating it for a nucleophilic S_N2-type transition state with a nearly linear S-O-O bond angle. Interestingly, similar proton dependence for peroxo complex activation has been observed in the case of molybdenum(VI), tungsten (VI), and titanium(IV) reduced Schiff base epoxidation catalysts, indicating that the protonation state of small molecule catalysts can have a significant effect on their reactivity.

Despite the wealth of information obtained from enzymatic and functional mimic studies, questions can still be raised regarding the mechanism of functional mimics and the precise role that protonation plays in halide and sulfide oxidation. Currently the functional mimics developed previously by the Pecoraro group, most notably K[VO(O_2)Hheida], are the most effective reactivity mimics for VHPOs and also have the fastest reported rates of any sulfoxidation catalyst.[62] Modern computational methods are employed in Chapter 2 to understand the

relative energetics of various protonation sites and to determine the role of protonation in peroxo-complex activation for halide and sulfide oxidation using a model of the most efficient functional mimic K[VO(O_2)Hheida]. This work elucidates the important role protonation plays in activation of the peroxo moiety and confirms that this class of functional models proceeds through an identical transition state as that observed for quantum chemical models of the enzyme, making K[VO(O_2)Hheida] a true functional model of VHPOs. In addition, this work provides the necessary geometrical constraints of the transition state for sulfide oxidation to rationally design an asymmetric catalyst.

While computational studies of the protonation states for K[VO(O_2)Hheida] provide energetic trends, they do not confirm the presence of a particular protonation state under catalytic conditions. X-ray absorption spectroscopy and vibrational spectroscopy can provide direct spectroscopic probes for a variety of protonation states. In particular, X-ray absorption spectroscopy provides a direct probe for protonation of the M=O moiety, while vibrational spectroscopy allows direct observation of the peroxo and carboxylate donor sets. These complementary techniques have increased our understanding of the accessible protonation states for peroxo-oxovanadium(V) complexes in both solution and the solid state as discussed in Chapter 3.

The most effective sulfoxidation catalyst reported to date is K[VO(O_2)Hheida]. With the transition state geometries calculated in Chapter 2, a chiral ligand set was designed to limit the accessible conformations in the transition state, while maintaining the first coordination sphere of K[VO(O_2)Hheida]. This new chiral catalyst allows for investigations into sulfide oxidation, solvent dependence on stereoselectivity and solution speciation, presented in Chapter 4. This work provides insight into the factors controlling the stereoselectivity of sulfoxidation and lays the groundwork for further design of chiral ligands.

Finally, Chapter 5 summarizes the results and discussions contained herein, and examine the implications of this work on VHPOs and general asymmetric oxidations using hydrogen peroxide. Several avenues for future work in this area are also discussed.

References

1. Lippard, S. J.; Berg, J. M. *Principles of Bioinorganic Chemistry*; University Science Books: Mill Valley, California, 1994.

2. Barber, J. *Inorganic Chemistry (Washington, DC, United States)* **2008**, *47*, 1700-1710.

3. Collman, J. P.; Boulatov, R.; Sunderland, C. J.; Fu, L. *Chemical Reviews (Washington, DC, United States)* **2004**, *104*, 561-588.

4. Rodgers, K. R.; Lukat-Rodgers, G. S. *Comprehensive CoordiComprehensive Coordination Chemistry IInation Chemistry II* **2004**, *8*, 17-60.

5. Guengerich, F. P. *Metal Ions in Life Sciences* **2007**, *3*, 561-589.

6. Rehder, D. *Inorganic Chemistry Communications* **2003**, *6*, 604-617.

7. Vilter, H. *Phytochemistry* **1984**, *23*, 1387-1390.

8. Thompson, K. H.; Orvig, C. *Journal of Inorganic Biochemistry* **2006**, *100*, 1925-1935.

9. Bolm, C. *Coordination Chemistry Reviews* **2003**, *237*, 245-256.

10. Butler, A.; Clague, M. J.; Meister, G. E. *Chemical Reviews (Washington, D. C.)* **1994**, *94*, 625-638.

11. Ligtenbarg, A. G. J.; Hage, R.; Feringa, B. L. *Coordination Chemistry Reviews* **2003**, *237*, 89-101.

12. Caero, L. C.; Hernandez, E.; Pedraza, F.; Murrieta, F. *Catalysis Today* **2005**, *107-108*, 564-569.

13. Anisimov, A. V.; Fedorova, E. V.; Lesnugin, A. Z.; Senyavin, V. M.; Aslanov, L. A.; Rybakov, V. B.; Tarakanova, A. V. *Catalysis Today* **2003**, *78*, 319-325.

14. Michaelson, R. C.; Palermo, R. E.; Sharpless, K. B. *Journal of the American Chemical Society* **1977**, *99*, 1990-1992.

15. Vilter, H. *Metal Ions in Biological Systems* **1995**, *31*, 325-362.

16. Wever, R.; Hemrika, W. *Handbook of Metalloproteins* **2001**, *2*, 1417-1428.

17. Van Schijndel, J. W. P. M.; Barnett, P.; Roelse, J.; Vollenbroek, E. G. M.; Wever, R. *European Journal of Biochemistry* **1994**, *225*, 151-157.

18. Everett, R. R.; Kanofsky, J. R.; Butler, A. *Journal of Biological Chemistry* **1990**, *265*, 4908-4914.

19. De Boer, E.; Wever, R. *Journal of Biological Chemistry* **1988**, *263*, 12326-12332.

20. Everett, R. R.; Soedjak, H. S.; Butler, A. *Journal of Biological Chemistry* **1990**, *265*, 15671-15679.

21. Krenn, B. E.; Izumi, Y.; Yamada, H.; Wever, R. *Biochimica et Biophysica Acta, Protein Structure and Molecular Enzymology* **1989**, *998*, 63-68.

22. Itoh, N.; Hasan, A. K.; Izumi, Y.; Yamada, H. *European Journal of Biochemistry* **1988**, *172*, 477-484.

23. Itoh, N.; Izumi, Y.; Yamada, H. *Biochemistry* **1987**, *26*, 282-289.

24. Tschirret-Guth, R. A.; Butler, A. *Journal of the American Chemical Society* **1994**, *116*, 411-412.

25. Martinez, J. S.; Carroll, G. L.; Tschirret-Guth, R. A.; Altenhoff, G.; Little, R. D.; Butler, A. *Journal of the American Chemical Society* **2001**, *123*, 3289-3294.

26. Carter-Franklin, J. N.; Parrish, J. D.; Tschirret-Guth, R. A.; Little, R. D.; Butler, A. *Journal of the American Chemical Society* **2003**, *125*, 3688-3689.

27. ten Brink, H. B.; Holland, H. L.; Schoemaker, H. E.; Van Lingen, H.; Wever, R. *Tetrahedron: Asymmetry* **1999**, *10*, 4563-4572.

28. Baciocchi, E.; Lanzalunga, O.; Malandrucco, S.; Ioele, M.; Steenken, S. *Journal of the American Chemical Society* **1996**, *118*, 8973-8974.

29. ten Brink, H. B.; Tuynman, A.; Dekker, H. L.; Hemrika, W.; Izumi, Y.; Oshiro, T.; Schoemaker, H. E.; Wever, R. *Inorganic Chemistry* **1998**, *37*, 6780-6784.

30. De Boer, E.; Plat, H.; Tromp, M. G. M.; Wever, R.; Franssen, M. C. R.; Van der Plas, H. C.; Meijer, E. M.; Schoemaker, H. E. *Biotechnology and Bioengineering* **1987**, *30*, 607-610.

31. De Boer, E.; Tromp, M. G. M.; Plat, H.; Krenn, G. E.; Wever, R. *Biochimica et Biophysica Acta, Protein Structure and Molecular Enzymology* **1986**, *872*, 104-115.

32. De Boer, E.; Van Kooyk, Y.; Tromp, M. G. M.; Plat, H.; Wever, R. *Biochimica et Biophysica Acta, Protein Structure and Molecular Enzymology* **1986**, *869*, 48-53.

33. Groves, J. T. *Journal of Inorganic Biochemistry* **2006**, *100*, 434-447.

34. Rush, C.; Willetts, A.; Davies, G.; Dauter, Z.; Watson, H.; Littlechild, J. *FEBS Letters* **1995**, *359*, 244-246.

35. Weyand, M.; Hecht, H. J.; Vilter, H.; Schomburg, D. *Acta Crystallographica, Section D: Biological Crystallography* **1996**, *D52*, 864-865.

36. Messerschmidt, A.; Prade, L.; Wever, R. *Biological Chemistry* **1997**, *378*, 309-315.

37. Mueller-Fahrnow, A.; Hinrichs, W.; Saenger, W.; Vilter, H. *FEBS Letters* **1988**, *239*, 292-294.

38. Weyand, M.; Hecht, H. J.; Kiesz, M.; Liaud, M. F.; Vilter, H.; Schomburg, D. *Journal of Molecular Biology* **1999**, *293*, 595-611.

39. Messerschmidt, A.; Wever, R. *Proceedings of the National Academy of Sciences of the United States of America* **1996**, *93*, 392-396.

40. Kravitz, J. Y.; Pecoraro, V. L.; Carlson, H. A. *Journal of Chemical Theory and Computation* **2005**, *1*, 1265-1274.

41. Messerschmidt, A.; Prade, L.; Wever, R. *ACS Symposium Series* **1998**, *711*, 186-201.

42. Soedjak, H. S.; Butler, A. *Inorganic Chemistry* **1990**, *29*, 5015-5017.

43. Kravitz, J. Y.; Pecoraro, V. L. *Pure and Applied Chemistry* **2005**, *77*, 1595-1605.

44. Pooransingh-Margolis, N.; Renirie, R.; Hasan, Z.; Wever, R.; Vega, A. J.; Polenova, T. *Journal of the American Chemical Society* **2006**, *128*, 5190-5208.

45. Arber, J. M.; De Boer, E.; Garner, C. D.; Hasnain, S. S.; Wever, R. *Physica B: Condensed Matter (Amsterdam, Netherlands)* **1989**, *158*, 126-127.

46. ten Brink, H. B.; Schoemaker, H. E.; Wever, R. *European Journal of Biochemistry* **2001**, *268*, 132-138.

47. De la Rosa, R. I.; Clague, M. J.; Butler, A. *Journal of the American Chemical Society* **1992**, *114*, 760-761.

48. Clague, M. J.; Keder, N. L.; Butler, A. *Inorganic Chemistry* **1993**, *32*, 4754-4761.

49. Wikete, C.; Wu, P.; Zampella, G.; De Gioia, L.; Licini, G.; Rehder, D. *Inorganic Chemistry* **2007**, *46*, 196-207.

50. Maurya, M. R.; Agarwal, S.; Bader, C.; Rehder, D. *European Journal of Inorganic Chemistry* **2005**, 147-157.

51. Plitt, P.; Pritzkow, H.; Kraemer, R. *Dalton Transactions* **2004**, 2314-2320.

52. Bashirpoor, M.; Schmidt, H.; Schulzke, C.; Rehder, D. *Chemische Berichte/Recueil* **1997**, *130*, 651-657.

53. Colpas, G. J.; Hamstra, B. J.; Kampf, J. W.; Pecoraro, V. L. *Journal of the American Chemical Society* **1996**, *118*, 3469-3478.

54. Meister, G. E.; Butler, A. *Inorganic Chemistry* **1994**, *33*, 3269-3275.

55. Butler, A.; Baldwin, A. H. *Structure and Bonding (Berlin)* **1997**, *89*, 109-132.

56. Cornman, C. R.; Colpas, G. J.; Hoeschele, J. D.; Kampf, J.; Pecoraro, V. L. *Journal of the American Chemical Society* **1992**, *114*, 9925-9933.

57. Rehder, D.; Bashirpoor, M.; Jantzen, S.; Schmidt, H.; Farahbakhsh, M.; Nekola, H. *ACS Symposium Series* **1998**, *711*, 60-70.

58. Maurya, M. R.; Khurana, S.; Schulzke, C.; Rehder, D. *European Journal of Inorganic Chemistry* **2001**, 779-788.

59. Maurya, M. R.; Kumar, A.; Ebel, M.; Rehder, D. *Inorganic Chemistry* **2006**, *45*, 5924-5937.

60. Colpas, G. J.; Hamstra, B. J.; Kampf, J. W.; Pecoraro, V. L. *Journal of the American Chemical Society* **1994**, *116*, 3627-3628.

61. Hamstra, B. J.; Colpas, G. J.; Pecoraro, V. L. *Inorganic Chemistry* **1998**, *37*, 949-955.

62. Smith, T. S.; Pecoraro, V. L. *Inorganic Chemistry* **2002**, *41*, 6754-6760.

63. Zampella, G.; Fantucci, P.; Pecoraro, V. L.; De Gioia, L. *Journal of the American Chemical Society* **2005**, *127*, 953-960.

64. Dickman, M. H.; Pope, M. T. *Chemical Reviews (Washington, DC, United States)* **1994**, *94*, 569-584.

65. Arcoria, A.; Ballistreri, F. P.; Tomaselli, G. A.; Di Furia, F.; Modena, G. *Journal of Molecular Catalysis* **1984**, *24*, 189-196.

66. Mimoun, H.; De Roch, I. S.; Sajus, L. *Bulletin de la Societe Chimique de France* **1969**, 1481-1492.

67. Mimoun, H.; Seree de Roch, I.; Sajus, L. *Tetrahedron* **1970**, *26*, 37-50.

68. Westland, A. D.; Haque, F.; Bouchard, J. M. *Inorganic Chemistry* **1980**, *19*, 2255-2259.

69. Schurig, V.; Hintzer, K.; Leyrer, U.; Mark, C.; Pitchen, P.; Kagan, H. B. *Journal of Organometallic Chemistry* **1989**, *370*, 81-96.

70. Bortolini, O.; Conte, V.; Di Furia, F.; Modena, G. *Journal of Molecular Catalysis* **1983**, *19*, 331-343.

71. Sharpless, K. B.; Townsend, J. M.; Williams, D. R. *Journal of the American Chemical Society* **1972**, *94*, 295-296.

72. Bortolini, O.; Di Furia, F.; Modena, G. *Journal of Molecular Catalysis* **1983**, *19*, 319-329.

73. Amato, G.; Arcoria, A.; Ballistreri, F. P.; Tomaselli, G. A.; Bortolini, O.; Conte, V.; Di Furia, F.; Modena, G.; Valle, G. *Journal of Molecular Catalysis* **1986**, *37*, 165-175.

74. Arcoria, A.; Ballistreri, F. P.; Tomaselli, G. A.; Di Furia, F.; Modena, G. *Journal of Molecular Catalysis* **1983**, *18*, 177-188.

75. Bortolini, O.; Campestrini, S.; Di Furia, F.; Modena, G. *Journal of Organic Chemistry* **1987**, *52*, 5093-5095.

76. Conte, V.; Di Furia, F.; Modena, G.; Bortolini, O. *Journal of Organic Chemistry* **1988**, *53*, 4581-4582.

77. Gisdakis, P.; Yudanov, I. V.; Roesch, N. *Inorganic Chemistry* **2001**, *40*, 3755-3765.

78. Mizuno, N.; Yamaguchi, K.; Kamata, K. *Coordination Chemistry Reviews* **2005**, *249*, 1944-1956.

79. Sharpless, K. B.; Verhoeven, T. R. *Aldrichimica Acta* **1979**, *12*, 63-74.

80. Katsuki, T.; Sharpless, K. B. *Journal of the American Chemical Society* **1980**, *102*, 5974-5976.

81. Pitchen, P.; Kagan, H. B. *Tetrahedron Letters* **1984**, *25*, 1049-1052.

82. Brunel, J.-M.; Diter, P.; Duetsch, M.; Kagan, H. B. *Journal of Organic Chemistry* **1995**, *60*, 8086-8088.

83. Matsumoto, K.; Sawada, Y.; Saito, B.; Sakai, K.; Katsuki, T. *Angewandte Chemie, International Edition* **2005**, *44*, 4935-4939.

84. Sawada, Y.; Matsumoto, K.; Kondo, S.; Watanabe, H.; Ozawa, T.; Suzuki, K.; Saito, B.; Katsuki, T. *Angewandte Chemie, International Edition* **2006**, *45*, 3478-3480.

85. Yudanov, I. V.; Gisdakis, P.; Di Valentin, C.; Rosch, N. *European Journal of Inorganic Chemistry* **1999**, 2135-2145.

86. Srinivasan, K.; Michaud, P.; Kochi, J. K. *Journal of the American Chemical Society* **1986**, *108*, 2309-2320.

87. Zhang, W.; Loebach, J. L.; Wilson, S. R.; Jacobsen, E. N. *Journal of the American Chemical Society* **1990**, *112*, 2801-2803.

88. Irie, R.; Noda, K.; Ito, Y.; Matsumoto, N.; Katsuki, T. *Tetrahedron Letters* **1990**, *31*, 7345-7348.

89. Khavrutskii, I. V.; Musaev, D. G.; Morokuma, K. *Proceedings of the National Academy of Sciences of the United States of America* **2004**, *101*, 5743-5748.

90. Chellamani, A.; Harikengaram, S. *Journal of Physical Organic Chemistry* **2003**, *16*, 589-597.

91. Pietikainen, P. *Tetrahedron Letters* **1999**, *40*, 1001-1004.

92. Lane, B. S.; Burgess, K. *Chemical Reviews (Washington, DC, United States)* **2003**, *103*, 2457-2473.

93. Linde, C.; Koliai, N.; Norrby, P.-O.; Akermark, B. *Chemistry--A European Journal* **2002**, *8*, 2568-2573.

94. Cavallo, L.; Jacobsen, H. *Journal of Organic Chemistry* **2003**, *68*, 6202-6207.

95. Linker, T. *Angewandte Chemie, International Edition in English* **1997**, *36*, 2060-2062.

96. McLain, J. L.; Lee, J.; Groves, J. T. *Biomimetic Oxidations Catalyzed by Transition Metal Complexes* **2000**, 91-169.

97. Mimoun, H.; Chaumette, P.; Mignard, M.; Saussine, L.; Fischer, J.; Weiss, R. *Nouveau Journal de Chimie* **1983**, *7*, 467-475.

98. Jaswal, J. S.; Tracey, A. S. *Inorganic Chemistry* **1991**, *30*, 3718-3722.

99. Talsi, E. P.; Chinakov, V. D.; Babenko, V. P.; Zamaraev, K. I. *Journal of Molecular Catalysis* **1993**, *81*, 235-254.

100. Funahashi, S.; Funada, S.; Inamo, M.; Kurita, R.; Tanaka, M. *Inorganic Chemistry* **1982**, *21*, 2202-2205.

101. Conte, V.; Di Furia, F.; Modena, G. *Journal of Organic Chemistry* **1988**, *53*, 1665-1669.

102. Bonchio, M.; Conte, V.; Di Furia, F.; Modena, G. *Journal of Organic Chemistry* **1989**, *54*, 4368-4371.

103. Murase, N.; Hoshino, Y.; Oishi, M.; Yamamoto, H. *Journal of Organic Chemistry* **1999**, *64*, 338-339.

104. Fernandez, I.; Khiar, N. *Chemical Reviews (Washington, D. C.)* **2003**, *103*, 3651-3705.

105. Bortolini, O.; Di Furia, F.; Scrimin, P.; Modena, G. *Journal of Molecular Catalysis* **1980**, *7*, 59-74.

106. Ballistreri, F. P.; Tomaselli, G. A.; Toscano, R. M.; Conte, V.; Di Furia, F. *Journal of the American Chemical Society* **1991**, *113*, 6209-6212.

107. Bolm, C.; Bienewald, F. *Angewandte Chemie, International Edition in English* **1996**, *34*, 2640-2642.

108. Blum, S. A.; Bergman, R. G.; Ellman, J. A. *Journal of Organic Chemistry* **2003**, *68*, 153-155.

109. Balcells, D.; Maseras, F.; Lledos, A. *Journal of Organic Chemistry* **2003**, *68*, 4265-4274.

110. Balcells, D.; Maseras, F.; Ujaque, G. *Journal of the American Chemical Society* **2005**, *127*, 3624-3634.

111. Santoni, G.; Licini, G.; Rehder, D. *Chemistry--A European Journal* **2003**, *9*, 4700-4708.

Chapter 2

Mechanistic Analysis of Nucleophilic Substrate Oxidations by Functional Models of Vanadium-Dependent Haloperoxidases: A Density Functional Theory Study

Introduction

Vanadium complexes have been used in a number of oxidative transformations[1] relevant to organic synthesis, including but not limited to alcohol oxidation, halide oxidation, and sulfoxidation. Of these reactions, the oxidation of achiral sulfides to chiral sulfoxides[1-4] has sparked the most attention in recent years because of the potential applications of chiral sulfoxides in pharmaceuticals and chiral resolution.[5] Oxovanadium peroxo complexes react with organic sulfides to form sulfoxides with little formation of the double oxidation product (sulfone).[1,6,7] The peroxo complexes can be formed in good yield using green oxidants, such as hydrogen peroxide, and a number of catalysts have been shown to be competent with respect to sulfide oxidation and in some cases to be stereoselective.[3,8-11] In addition to small molecule catalysts, vanadium dependent haloperoxidases have also been shown to carry out the stereoselective conversion of thieothers to their corresponding chiral sulfoxides. To date, K[VO(O_2)Hheida] (Hheida = N-2-hydroxyethyl iminodiacetate) is the most efficient vanadium-based sulfoxidation catalyst, having the highest reported rate in the literature. The reactivity of this complex has been studied extensively with respect to peroxide binding, kinetics, and halide and sulfide oxidation.[12-14] Thus, K[VO(O_2)Hheida] not only serves as an effective functional mimic for the vanadium dependent haloperoxidases, but is an excellent catalyst in its own right.

While considerable effort has been expended to clarify the enzymatic mechanism, relatively little attention has been focused on understanding the mechanism of the original catalysts described by Colpas and co-workers.[12-14] These complexes are not only important for furthering our understanding of VHPO's, but they are as useful catalysts in organic synthesis. Mechanistic studies have shown that the maximal rate of substrate oxidation occurs when one proton per vanadium is present. A red shift in the peroxo-vanadium charge transfer band indicates the direct protonation of the vanadium complex. V^{51} NMR showed a single resonance with a chemical shift and a linewidth consistent with a single mono-peroxo oxovanadium(V) species under the reaction conditions; however, this result does not rule out rapidly interconverting isoenergetic species. These observations were incorporated into a mechanistic proposal that was developed on the bases of the previously proposed halide oxidation mechanism, involving a hydroperoxo vanadium species undergoing an oxo transfer reaction with organic sulfides[6] (Figure 2.1). Despite these extensive mechanistic studies, solution speciation under the reported reaction conditions, the site of catalyst protonation, the role of the protonated peroxo moiety in oxidative catalysis, and the geometry of the transition state are not fully understood.

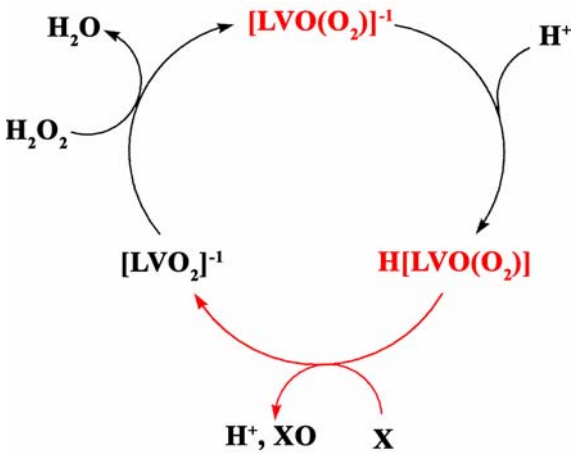

Figure 2.1. Diagram of the proposed mechanism for oxidation of a nuclephilic substrate by tripodal amine complexes of vanadium(V). X = Br^-, I^-. or R_2S. Steps highlighted in red are the focus of this study.

Density Functional Theory (DFT) has been used to address questions regarding reactivity and spectroscopic properties of transition metal systems related to biology[15] and catalysis.[16] Balcells et al. reported computational studies of truncated quantum chemical (QC) models for vanadium(V) containing Schiff-base complexes[17] and their ability to oxidize organic disulfides in the presence of hydrogen peroxide. This study was later expanded using QM/MM methods to determine the factors controlling the stereoselectivity of disulfide oxidation[18] on sterically hindered Schiff-base-vanadium complexes.[7,9-11,19] Balcells et. al showed that an S_N2 like transition state is likely to be involved in disulfide oxidation, where oxo-transfer occurs to the organic disulfide from the unprotonated oxygen of the peroxo moiety. Although the coordination environment of the Schiff base complex is significantly different from that of the enzyme, it does bear some similarities, including a side-bound peroxo and an S_N2 type transition state. Schiff-base vanadium(v) complexes have been shown to be functional mimics for VHPO, and this is based on their ability to oxidize bromide and organic sulfide.[9,11,19] The kinetic analysis, and consequently, detailed mechanistic studies, are complicated by bromination of the ligand.[20]

K($VO(O_2)$Hheida) has been studied extensively with respect to both bromide[13] and sulfide[6] oxidation. These studies have provided mechanistic insight for both VHPOs and peroxovanadium(V) catalysts; however, questions can still be raised regarding the identity of a protonated peroxo-vanadium species, the role of protonation in substrate oxidation, and the geometry of the transition state. We present herein a detailed computational investigation of this catalyst. By treating the entire complex quantum mechanically, we provide insight into the mechanism for substrate oxidation, allowing for the rational design of a new chiral catalysts to be discussed in Chapter 4. These studies provide a mechanistic correlation between these functional mimics and VHPO's. This work was published and featured as a cover article for European Journal of Inorganic Chemistry.[21]

Experimental Section

DFT geometry optimizations of molecular structures were performed using the BP86 functional[22] and an all-electron triple-ζ basis set with polarization functions on all atoms (TZVP).[23] Calculations were carried out using the Turbomole suite of programs[24] in conjunction with the resolution of identity technique.[25,26]

Optimizations of the transition state structures were performed using a procedure based on a pseudo Newton-Raphson method. Initial starting structures of a guessed transition state were optimized by constraining the distances related to the reaction coordinate, specifically those for the peroxo O-O and the substrate X-O or S-O (where X= I^-, Br^-, Cl^- S=sulfur of dimethyl sulfide) interatomic distances. The initial Hessian matrix was calculated at the classical level, whereas the BP86-RI/TZVP was used to compute the Hessian matrix of the minimum energy structures. Full vibrational analysis of the stationary points was carried out to ensure the presence of one eigen-mode featuring an imaginary frequency that corresponded to the reaction coordinate. This point was then used as a starting point for the transition state searches, which were conducted using an eigenvector-following strategy.

Transition states are labeled on the basis of the number of negative charges present on vanadium complex (**-1** or **0**), site of protonation (Figure 2.2a), and the nature of the substrate. In the case of dimethyl sulfide transition states, a letter has been assigned to the rotational conformation of the methyl groups. **P** indicates a methyl group that is parallel to the vanadium peroxo group or **A** indicates an antiparallel methyl group (Figure 2.2b). A transition state corresponding to protonation of the left-side peroxo oxygen atom with dimethyl sulfide in a parallel methyl group orientation would be **0a_sP**, while the anionic transition state for bromide oxidation would be **1_br** (Figure 2.2).

Full vibrational analysis has been carried out to characterize each stationary point. The effects of solvation were evaluated with the solvent continuous model approach COSMO[27,28] as implemented in the Turbomole suite of programs. The

polarizable continuum medium is expected to mimic the effects of a pure solvent environment; to this purpose the dielectric constant for acetonitrile (ε=36.64) was used because previous studies[6,13] have employed it as the solvent to explore the reactivity of monoperoxo oxovanadium complexes. Corrections have been computed to estimate ΔG from ΔE, by calculating the roto-vibrational partition function of the different molecular species. The error within the calculated energy differences is estimated to be approximately 2.0 kcal/mol for neutral species. Charged species are expected to have a greater error due to the stronger effects of solvation, in which case we have conservatively estimated the error to be 4 kcal/mol.

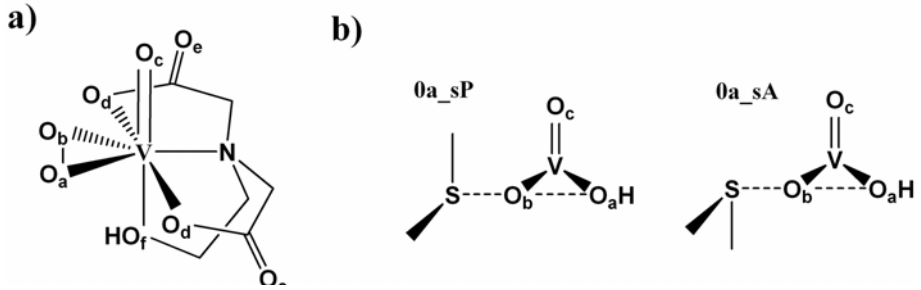

Figure 2.2. (a) Oxygen atom labeling scheme for $KVO(O_2)Hheida$ for protonation studies. (b) Schematic representation of two rotational confirmations explored for transition states involving dimethyl sulfide.

Results

Quantum Chemical System

The x-ray coordinates for $K[VO(O_2)Hheida]$[12] were used as a starting point to set up a quantum chemical model of this system. Waters of crystallization and the potassium counterion were removed from the quantum chemical model. Under the reaction conditions used by Colpas et al., there are two equivalents of 18-crown-6 that chelate the potassium ion in acetonitrile, which limits the potential interactions of the cation with the vanadium complex during the catalytic cycle. The resulting energy-minimized geometry of $[VO(O_2)Hheida]^{-1}$ (**1**), depicted in Figure 2.3 is nearly identical to the bond distances reported in the crystal structure (Table 2.1).

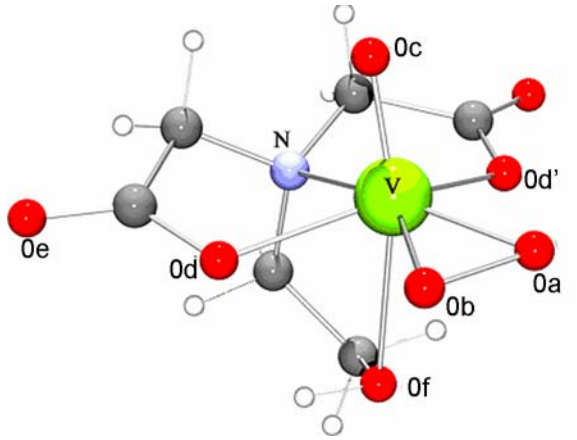

Figure 2.3. Ball-and-stick representation of geometry-optimized $[VO(O_2)Hheida]^{-1}$ (**1**) ($Hheida^{2-}$ = N-(2-hydroxyethyl)iminodiacetate).

Potential solution species and viable protonation states

Before exploring the oxidative chemistry of **1**, a better understanding of the solution state speciation for this pre-catalytic species is necessary. The crystal structure of $K[VO(O_2)Hheida]$ shows a disordered hydroxyl ethyl arm due to the two ring conformation of the five-membered chelate rings. The interconversion between these two states is rapid compared to the rate of oxidation; therefore, the two rings on the left and right hand sides of **1** are treated as equivalent for optimizations involving an $Hheida^{-2}$ ligand. The weakest coordinating and, therefore, most labile donor atom is the oxygen associated with the N-hydroxyethyl arm of $Hheida^{2-}$. Geometry-optimized structures were obtained initially both with a coordinated hydroxyl oxygen atom and a completely dissociated hydroxyl group. The former being the more stable of the two by 1.3 kcal/mol. Given the two potential pre-catalytic isomers, a coordinated hydroxyl and the uncoordinated hydroxyl group, and the presence of sigma donor ligands under the reaction conditions used (water, acetonitrile, and substrate), a vacant coordination site is not likely. As there is no experimental evidence supporting coordination of substrate molecules in VHPO or in the small molecule models, substrate coordination was ruled out as a possibility. A comparison was made of the energetic differences between the van der Waals complex of the exogenous

donors, water and acetonitrile, with the coordinated exogenous donor in place of the hydroxyl group (Figure 2.4c,d). These comparisons were made using the most stable protonated species to reduce the electronic repulsion created by the approach of a sigma donor to an anionic vanadium species. The results of this comparison are presented later in this chapter.

Table 2.1. Bond distance comparison in Å of $[VO(O_2)Hheida]^{-1}$.

	X-ray Structure	*Optimized*
V-Oc	1.60	1.62
V-Oa	1.87	1.85
V-Ob	1.86	1.85
V-Od	2.05	2.10
V-Od'	2.04	2.05
V-Of	2.24	2.45
V-N	2.19	2.28
Oa-Ob	1.43	1.44

Five potential sites of protonation were identified on the basis of the areas of highest electron density for **1**: oxo (**0c**), peroxo left (**0b**), peroxo right (**0a**), carboxylate oxygen (**0d**), and the carbonyl oxygen (**0e**) (Figure 2.4). Only one of the carboxylate donors was protonated due to the previously mentioned conformational isomerism. Protonation of the peroxo can occur in four possible locations as illustrated in Figure 2.4b. The most stable optimized structures involved protonation of the peroxo ligand **0a** or **0b**. The four possible orientations of the proton around the peroxo ligand were isoenergetic when ring conformations were taken into account. There is significant contraction of the vanadium hydroxyl bond (V-Of) upon protonation of the complex in **0a**, **0b**, or **0c**, a decrease of 0.1 Å for **0a** and **0b**, and 0.2 Å for **0c.**

The most stable optimized geometry, **0a**, was used to determine whether exogenous ligands can bind trans to the oxo-moiety. Three exogenous donors were tested in place of hydroxyl coordination to the vanadium center: water, acetonitrile, and bromide. In all cases, a van der Waals complex of the exogenous donor and **0a** is more stable than coordination of the respective donor

in place of the hydroxyl. In the case of water coordination to **0a,** (Figure 2.4c,d), hydroxyl coordination to vanadium over water was favored by 4.0 kcal/mol. The absence of a trans donor to the V=O bond resulted in a complex that is 4.6 kcal/mol higher in energy than the coordinatively saturated complex, **0a**.

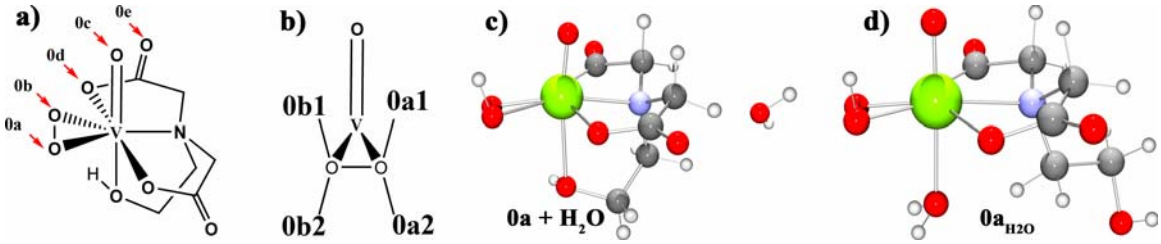

Figure 2.4. (a) Possible proton acceptors in $VO(O_2)$Hheida (b) Nomenclature for the orientation of proton with respect to V=O bond (c) Representative ball-and-stick diagram of a non-coordinated exogenous donor, in this case the non coordinating donor is water. (d) Representative cartoon for coordination of an exogenous donor (water) to vanadium. White atoms are hydrogens, green is vanadium, oxygen is red, and carbon is gray.

Transition State Calculations - Halide Transition States

Transition states corresponding to the nucleophilic attack of halide ions (Cl^-, Br^-, I^-) on the peroxo ligand of the vanadium atom were located for both **1** and **0a**. Because of the anionic character of both the halide and **1,** starting materials were calculated using two infinitely separated species, as any attempt to minimize a van der Waals complex resulted in the two ions rapidly diverging. The transition state geometry found for **1** with all three halides (**1_cl, 1_br, 1_i)** are nearly identical; therefore, a representative case will be presented for the oxidation of bromide. The transition state for bromide oxidation is characterized by a nearly linear halide peroxo bond angle (173°), where the dihedral angle between the peroxo ligand and the vanadium-oxo is 100° (Figure 2.5). The rest of the vanadium coordination sphere is significantly perturbed in comparison to **1**, and there is a dramatic lengthening of all bonds in the first coordination sphere. In the case of **1_br,** the carboxylate donors have bond distances of 2.27 Å, whereas the carboxylate-vanadium distances in **1** are 2.04 Å. Additionally, the

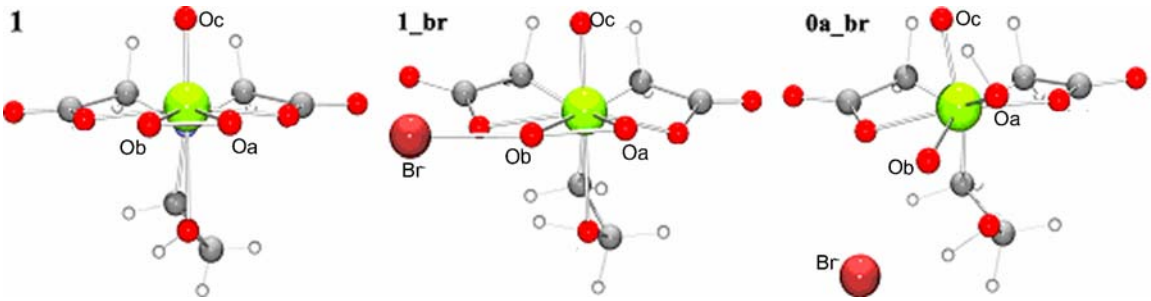

Figure 2.5. Ball-and-Stick cartoons showing pre-catalytic anionic complex (left), dianionic transition state for bromide oxidation (middle), and the corresponding monoanionic transition state. White atoms are hydrogens, green is vanadium, oxygen is red, carbon is gray, and bromide is dark red.

tertiary nitrogen bond lengthened by 0.3 Å in relation to **1** (Table 2.2). The computed barrier of activation, $\Delta G^{\ddagger}$, for bromide oxidation is 38.1 kcal/mol.

Protonation of **1** at the most stable site (**0a**) yields an earlier transition state (**0a_br**), in which the Br-O bond is only partially formed with a nearly complete O-OH bond in the peroxo moiety. This state has a significantly lower barrier of activation (21.1 kcal/mol). The bromide–peroxo oxygen bond distances is longer by 0.11 Å than **1_br**, with a comparably shorter peroxide bond length. The Br-Ob-Oa bond angle is 163.4° while the dihedral angle between the Ob-Oa and V=Oc is 123.8°. Transition states were only located in the protonated case where a hydrogen bond formed between the halide and the hydroxyl ligand. No transition states related to halide oxidation could be located for attack of the substrate on the protonated peroxo ligand. This is true for all anionic halide transition states (**0a_cl, 0a_br, and 0a_i**), where the corresponding barriers to activation are 23.0 kcal/mol for Cl^- and 19.0 kcal/mol for I^-. Table 2.2 shows the relevant bond distances for the neutral halide transition states with **1** and **1_br**.

To explore the reactivity of **0a_x** further, a coordinatively unsaturated geometry in which a halide can weakly coordinate to vanadium(V) center, was used as the starting point. Bromide was used as the substrate and positioned to weakly coordinate to the vanadium center. **0a_br2** is characterized by a distortion of the dihedral angle between V=Oc and Ob-Oa of 149°, this allows for a weak interaction between bromide and vanadium with a bond length of 3.03 Å. A reasonable reactant structure could be located with bromide coordinating to the

vanadium, and the computed barrier of activation is 8.6 kcal/mol. The barrier is significantly lower energy because the coordination of bromine to a coordinatively unsaturated vanadium complex (**0a_br2**) is 10 kcal/mol higher energy than the corresponding hydrogen bonded starting materials (**0a_br**). The geometries and respective energy differences between starting materials and transition states for all located halide transition states are presented in Table 2.3. No transition states could be located corresponding to attack of bromide on the oxo ligand of **1**, **0a**, or **0c.**

Table 2.2. Bond Distances (Å) of transition states for halide oxidation.

	1	**1_br**	**0a_br**	**Oa_cl**	**Oa_i**
V-Oc	1.62	1.64	1.62	1.61	1.62
V-Ob	1.85	1.71	2.05	2.03	2.09
V-Oa	1.86	1.90	1.90	1.90	1.88
V-Od	2.10	2.27	2.02	2.01	2.01
V-Od'	2.05	2.27	1.99	2.02	1.99
V-Of	2.45	2.48	2.30	2.34	2.29
V-N	2.28	2.50	2.29	2.28	2.27
Ob-Oa	1.44	1.87	1.69	1.77	1.67
Ob-X	N/A	2.27	2.38	2.29	2.85

Table 2.3. Comparison of relevant bond distances (Å), dihedral angles (°) and $\Delta G^{\ddagger}$ (kcal/mol) for transition states associated with halide oxidation.

	1	**1a_cl**	**1a_br**	**1a_i**	**0a**	**0a_cl**	**0a_br**	**0a_i**	**0a_br2**
Ob-X (Å)	---	2.17	2.27	2.39	---	2.29	2.38	2.55	2.48
Ob-Oa (Å)	1.44	1.85	1.87	1.90	1.46	1.77	1.69	1.69	1.70
V=Oc Ob-Oa	98°	100°	100°	100°	103°	124°	123°	121°	149°
$\Delta G^{\ddagger}$ *kcal/mol*	---	39.2	38.1	36.0	---	23.0	21.1	19.0	20.0

Transition State Calculations - Sulfide Transition States

The effects of protonation on the barrier of activation were also explored for the oxidation of dimethyl sulfide. Transition states calculated for dimethyl sulfide oxidation are less distorted from the energy-minimized structures of **1** or the appropriate protonated species **0(a,b)** than for the corresponding halide transition state. Figure 2.6 shows two representative transition states located for sulfide oxidation by anionic and neutral vanadium species.

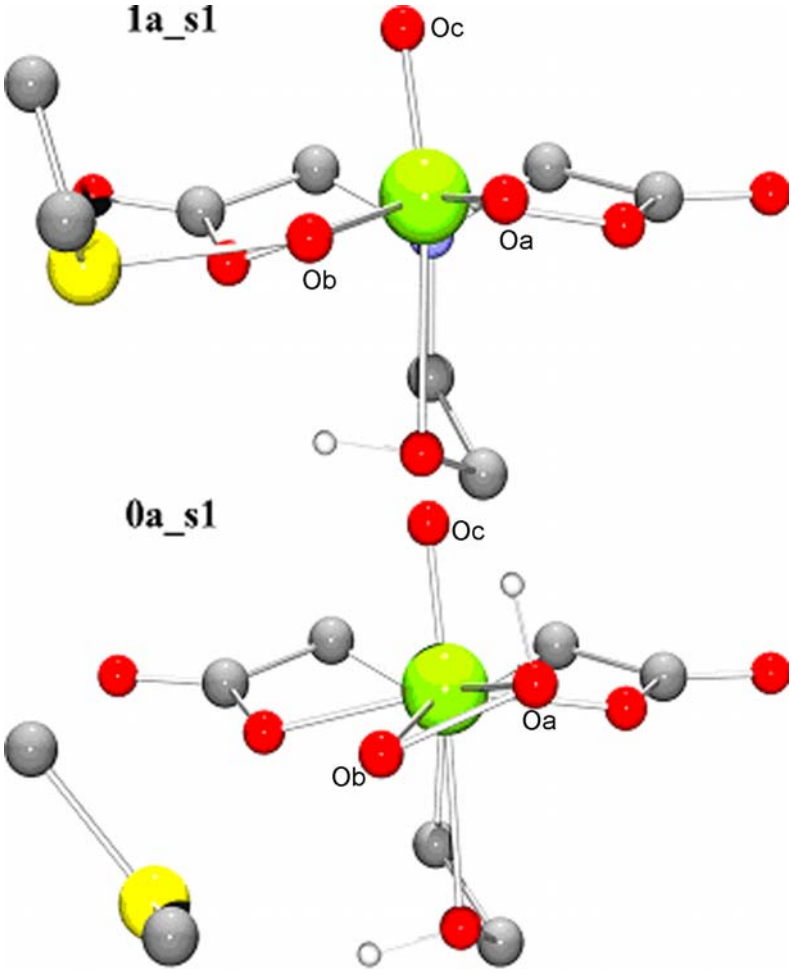

Figure 2.6. Ball-and-stick representation of an anionic (top) and neutral (bottom) transition states located for dimethyl sulfide oxidation. Protons have been omitted for clarity.

The transition state geometry **1_s1** is characterized by a nearly linear S-Ob-Oa bonding angle of 176°, identical to that identified for the case of halide

oxidation. Due to the asymmetry associated with upper and lower halves of **1,** multiple transition states with slightly different energies could be located, the only difference being related to the relative orientation of the methyl groups of dimethyl sulfide. Approach of dimethyl sulfide to the left or right hand side of **1** yielded nearly isoenergetic transition states, with a barrier of activation of 18.3 kcal/mol. Starting materials were minimized from each located transition state generating a van der Waals complex of dimethyl sulfide and **1**.

Transition states were located for the protonated complexes **0a_s** and **0b_s**. As was the case for **1**, multiple rotational isomers could be located and are related to orientation of the methyl groups on the substrate. The neutral transition states located for dimethyl sulfide oxidation are less distorted than those located for halide oxidation. For dimethyl sulfide oxidation the V=Oc and Ob-Oa dihedral angle = 111.8°, and the substrate peroxide bond angle, S-Ob-Oa, = 166.6°. To calculate the barrier of activation, van der Waals complexes of dimethyl sulfide and the appropriately protonated vanadium species were optimized. The lowest energy starting material complex located contained a hydrogen-bond between dimethyl sulfide and the hydroxyl group of the complex. The barrier of activation for the oxidation reaction is 9.4 kcal/mol. The barrier of activation drops significantly (by 9 kcal/mol), when the peroxo moiety is protonated, leading to four isoenergetic transition coordinates differing in the approach of sulfide to the neutral vanadium complex and the orientation of the sulfide. No transition states could be located that are related to attack of the sulfide on the unprotonated oxo group (**0c**) or attack of the sulfide on the protonated peroxo oxygen.

Discussion

Although many model complexes of VHPOs[13,19,20,29,30] have been reported, the pre-catalytic species K[VO(O_2)Hheida][12] isolated by Colpas and co-workers is the most thoroughly investigated system. Detailed mechanistic studies have shown the importance of protonation of the complex with respect to halide[13] and sulfide oxidation.[6] These studies established K[VO(O_2)Hheida] as a functional

mimic of the vanadium dependent haloperoxidases and as an excellent catalyst for organic transformations. We have undertaken a thorough computational investigation of the mechanism for halide and sulfide oxidation, specifically with respect to the effects of protonation of the complex on the activation barrier for these processes in order to develop a basis for synthesizing future asymmetric oxidation catalysts based on the H_3heida architecture.

Starting coordinates are taken from the crystallographically characterized pre-catalyst. From these, chemically reasonable solution state species were optimized. The crystal structure of K[VO(O_2)Hheida][12] shows a hydroxyl group trans to the oxo, with tertiary nitrogen trans to the peroxo moiety, a typical binding mode for oxovanadium(V) peroxo complexes with tripodal amine ligands. The solvent dielectric and potential exogenous donors present under the experimental conditions were taken into account. Potassium is chelated by 18-C-6 in order to solubilize K[VO(O_2)Hheida] in acetonitrile. The chelated potassium is unlikely to have strong interactions with the vanadium complex and consequently was excluded from the quantum chemical models (Figure 2.3 and Table 2.1). The weakest donor group in **1** is the hydroxyl group trans to the oxo. As there is no ligand field stabilization energy for a vanadium(V) complex, a coordinatively unsaturated species is potentially feasible. Geometry optimization was performed on an anionic complex in which the hydroxyl group was completely dissociated from the complex, the resulting optimized structure is 1.3 kcal/mol higher in energy when enthalpic and entropic corrections are taken into account. Under the reaction conditions a number of exogenous donors are present in at least equimolar quantities with respect to the vanadium complex, making a coordinately unsaturated species less likely.

Before examining the energetic preference for exogenous donors, we explored the energetics of monoprotonated **1**. The potential proton acceptors in the complex are all of the oxygen atoms associated with the ligand. This generates five potential sites of protonation (Figure 2.4). Protonation of the peroxo ligand is the most energetically favored. There is only a slight difference between protonation of O3 and O2, and this effect is negligible when chelate ring

conformations of the hydroxyethyl arm of **1** are taken into account. Protonation of the peroxo (**0a** and **0b**) is favored by 3 kcal/mol; this difference in energy corresponds to a 10-fold higher concentration of the hydroperoxo species over protonated oxo species (**0c**). Protonation of either carboxylate oxygen generates a species 6 kcal/mol higher in energy.

Using the energetically favored protonation states of the complex, two optimizations were performed for exogenous donors, one in which a van der Waals complex of the donor was made with a coordinated hydroxyl species **0a**, and one with the exogenous donors coordinated in place of the hydroxyl. Of the exogenous donors tested, water, acetonitrile, and bromide, coordination of the N-hydroxyethyl donor was more stable by 2, 7, and 15 kcal/mol respectively. Thus, a coordinated hydroxyl species is likely to be the dominate solution species present. Previously, ^{51}V NMR has been used to explore the number of vanadium species present under the reaction conditions, suggesting that only one species is present or there is an exchange process with a rate constant > 0.5 s^{-1}. All factors considered, the loss of entropy is higher in the cases of exogenous donor molecules. Since the enthalpic contribution is roughly similar when considering exogenous and endogenous ligands (on binding to V) a larger gain in the entropy is expected when a water, bromide, or other exogenous ligand dissociates, compared to an endogenous ligand.

Using the most stable unprotonated (**1**) and protonated species (**0a**) as a starting point, searches for transition states were performed for chloride, bromide, and iodide (Figure 2.5). Transition state located for **1** showed a significant lengthening of all ligand bonds to the vanadium, due to the increased electron density of the complex in the transition state (Table 2.2). All bond distances are still within a weak bonding distance. The transition state corresponded to the S_N2 like attack on the peroxo ligand of the vanadium complex, as determined by examining the single negative vibrational eigenvalue. Importantly, no transition state could be located for bromide attack on the vanadium-oxo bond. The instability of the two anionic species in the gas phase calculation prevented the energy minimizaiton of van der Waals complexes of the vanadium complex and a

halide. Consequently, the sum of self-consistent-field energies for **1** and the appropriate halide were used as the starting materials to calculate the barriers to activation. The resulting energies of activation were 39, 38, and 36 kcal/mol for chloride, bromide, and iodide respectively.

Upon protonation of the complex, a pre-reaction adduct is formed, in which a hydrogen bond between the halide ion and the complex is present, and most importantly, the barriers of activation decreased dramatically. The resulting monoanionic transition states are S_N2-like with the nearly linear X-Ob-OaH bond angle ≈ 163º and have strongly distorted V=Oc and Ob-Oa dihedral angle ≈ 123º (Figure 2.5). The hydrogen bond is maintained in all anionic halide transition states, and no transition states could be located for complexes in which this hydrogen bond was not present. Due to the large electron density surrounding the carboxylate donors of **0a**, it is necessary to stabilize the negative charge of the halide in this early transition state. Under the experimental reaction conditions this stabilization could be accomplished by the presence of hydrogen bond donors (water or hydrogen peroxide) or cations (tetraethylammonium or potassium).

Zampella et al. located transition states for the oxidation of bromide using quantum chemical models of the active site of a VHPO.[31] Their results showed that nucleophilic attack of the halide on the unprotonated oxygen of a hydroperoxo species had the lowest barrier of activation. Transition states were located for the vanadium peroxo adduct; protonation of the peroxo moiety yielded a significantly more stable transition geometry that resulted in a lower barrier of activation. The hydroperoxo transition state occurred significantly earlier with respect to halide-oxygen formation than the peroxo transition state. The transition states located for bromide oxidation by **1** and **0a** show the same trend with respect to the halide-oxygen bond formation. The resulting transition state **0a_br** shows a longer halide-oxygen bond than **1_br**, indicating an earlier transition state. Additionally, there is a dramatic decrease in the barrier of activation from **1_br** to **0a_br** (Table 2.3); this observed decrease in the barrier of activation is likely an oversimplification of the experimental barrier because of the

interaction between two anionic species (vanadium complex and the halide) in the case of **1_br**. Indeed, under reaction conditions it may be possible to carry out this reaction by offsetting the negative charge with strongly associated cations or hydrogen bond donors. These results now correlate the mechanism of halide oxidation for the best reported functional model for VHPO, K[VO(O_2)Hheida], with the proposed mechanism for halide oxidation by the enzyme. The importance of offsetting the negative charge on the anionic halide is observed in the case of the **0a_br** transition state. Thus, a hydrogen bond forms between the bromide and the hydroxyl group of the ligand resulting in a distorted dihedral angle for the peroxo moiety with respect to the vanadium-oxo bond (Table 2.2). This is further supported by the location of a nearly isoenergetic reaction pathway, in which the bromide weakly coordinates to vanadium (Figure 2.5, **0a_br2**).

Given that VClPO is capable of oxidizing chloride, bromide, and iodide, and K[VO(O_2)Hheida] has been shown to be competent with respect to only bromide and iodide oxidation, we chose to explore the differences in activation barriers for the oxidation of the aforementioned halides. Reactivity studies demonstrate that protonated K[VO(O_2)Hheida] is capable of oxidizing bromide and iodide, but not chloride. Two possible factors could contribute to this inability to oxidize chloride: 1. The reduction potential of the chloride is sufficiently high to prevent oxidation, 2. The active protonated form of the complex cannot be generated in presence of chloride. The latter hypothesis was presented by Colpas et al. to explain this reactivity.[13] Slebodnick et. al. demonstrated the ability of a tripodal amine complex to oxidize chloride when a mixture of acetonitrile (94%) and water (6%) were used as the solvent system.[32] Since chloride oxidation is not observed in either pure solvent it was suggested that in a mixture of the two solvents the basicity of the peroxo vanadium species increases with respect to chloride, allowing the catalytically active protonated species to be formed. Based on the transition state energies presented herein, there is not a large difference in the energies of activation for each of the halides (19 kcal/mol for I^-, 20 kcal/mol for Br^- to 23 kcal/mol for Cl^-); therefore, differences in the reactivity cannot be

explained solely on the differences in reduction potentials of the oxidized halides. Because protonation of the complex generates an early transition state, in which formation of the halide oxygen bond is very weak, there is less contribution of halide orbital character in the transition state, leading to smaller differences in the barrier of activation for halide oxidation (Table 2.3). These energies of activation presented here provide further support for the hypothesis that the basicity of chloride in acetonitrile is high enough to deprotonate the activated catalysts, thereby preventing chloride oxidation.

To complete the functional correlation between the quantum chemical models of the enzyme system and functional models for the enzyme, we examined the effects of protonation of the complex on organic sulfide oxidation. In the case of halide oxidation, the effects of protonation on the reaction barriers are masked to some degree by a highly charged dianionic transition state in the case of **1_x**. However, this does represent the experimental conditions very well, considering the chelation of potassium ions by 18-crown-6 prevent strong ion pair formation.

The organic sulfide oxidation system does not suffer from this highly charged transition state, so that we are better able to understand the effects of protonation of the peroxo with respect to the barrier of activation for oxidation. Dimethyl sulfide was used as the organic sulfide to explore a number of transition state geometries for both anionic and neutral catalytic species. The anionic transition states located were similar to those located for halide oxidation, a nearly linear S-Ob-Oa bond angle (175°) with V=Oc and Ob-Oa dihedral angle of 101°. The S-O bond length at the transition state was 2.08 Å, indicating a high degree of sulfide-oxygen bonding character. These geometric parameters were conserved across the four anionic transition states located, two transitions for nucleophilic attack of DMS on the left and right hand side of the complex with two rotational isomers of DMS per side. Protonation of the peroxo moiety of **1** yielded lower energy transitions states (**0a_s, 0b_s**), again exhibiting a lower degree of sulfur oxygen bond formation leading to an earlier transition state that is identical to the trend observed for halide oxidation. The decrease in the barrier of activation of 8 kcal/mol is consistent with the dramatic increase in the rate of

sulfide oxidation by K[VO(O_2)Hheida] upon protonation. As the transition states located for the anionic catalytic species (**1_s1, 1_s2, etc…**) are monoanionic, there is an overestimation of the barrier of activation for this pathway, though this overestimation is less dominant that it was in the case of the dianionic halide transition states. The overall error in the energy differences is estimated to be approximately 2.0 kcal/mol. The error with respect to experimental systems is likely greater than this; however, knowledge of experimental barriers to activation does not exist to reliably estimate these differences. The anionic catalytic species may still present a viable reaction path in the presence of strong hydrogen bonding or other ionic effects that could stabilize the transition state. This being said, the energy differences between the **1_s** and **0a_s** or **0b_s** are significant enough to consider the latter to be the dominant catalytic pathway.

The results presented above provide a direct correlation between the proposed transition state geometries for VHPO's with the best known functional mimic for the same enzymes, making K[VO(O_2)Hheida] a complete functional model for vanadium dependent bromoperoxidases. As was the case for the enzyme studies, protonation of the peroxo moiety leads to an early transition state and a dramatic decrease in the barrier of activation for substrate oxidation (substrate = halide or sulfide). Typical features of the transition states from enzyme model system are maintained (i.e., nearly linear S-O-O angle and similar bonding distances). Additionally, we provide support for the reactivity hypothesis presented by Colpas et al. that describes the halide oxidation ability of K[VO(O_2)Hheida]. The early transition states generated by protonation of the complex lead to small differences in the barrier of activation for halide oxidation, in contrast to the large difference in reduction potential for chloride, bromide, and iodide.

A comparison of van der Waals adducts obtained with the hydro-peroxo species of enzyme and synthetic models show that in both cases the substrate has a suitable spatial orientation to react with the hydroperoxo moiety. In particular, in the enzyme models, the atom of the substrate that undergoes oxidation (S, Br, I, Cl) is weakly coordinated to the vacant coordination position of

vanadium, and the interaction with vanadium places the substrate in the proper spatial orientation to act as attacking group in the S_N2 reaction.[31] In the synthetic model, the role of vanadium in positioning the substrate is played by the hydroxyl ligand coordinated to the metal. In fact, the structure of the pre-reaction adducts obtained with the hydro-peroxo form of the synthetic complex show that the atom of the substrate that will undergo oxidation is involved in a hydrogen bond with the hydroxo group. Formation of this hydrogen bond positions the substrate in the proper location to act as a nucleophile in the S_N2 reaction. Therefore, in both cases (enzyme and synthetic models), the vanadium complex plays a role in properly positioning the substrate in the transiently formed pre-reaction adduct.

The calculated barriers to activation for K[VO(O_2)Hheida], in the case of both bromide and sulfide oxidation, are slightly higher than that calculated for the enzyme system (Table 2.4). The differences in the barriers of activations between the enzyme and synthetic model systems can be explained by the polarization of the peroxo bond and the torsional angle of the peroxo ligand in the transition-state geometries . The hydroperoxo moiety is more activated in the enzyme model; in particular, the O-O bond is longer (1.467 enzyme model vs 1.458 Å synthetic model), and the peroxo bond is more polarized (Dq = 0.12 enzyme model vs 0.02 synthetic model). This difference in polarization arises from the coordinatively unsaturated 5 coordinate vanadate co-factor in the enzyme. The functional model has a filled coordination sphere (7 coordinate) with a pseudo- σ_v symmetry element bisecting the peroxo moiety and thereby reducing the polarization of the peroxo species. Additionally, in the transition states computed for the synthetic model, the hydroperoxo group is slightly tilted (Figure 2.5 and Figure 2.6) due to simultaneous formation of the hydrogen bond with the hydroxo group and S_N2 type oxo transfer reaction. The tilting of the hydroperoxo group in the transition state is possibly another factor responsible for increasing the energy of the transition state, thereby increasing the barrier to activation.

Table 2.4. Comparison of computed $\Delta G^{\ddagger}$ for thioether (DMS) and bromide (Br) oxidation using the enzyme and synthetic models (energies in kcal/mol). All energy values are obtained as difference between TS energies and Van der Waals reactant adducts.

	Enzyme model	*Synthetic model*
DMS	2.9	9.4
Br^-	3.7	21.1

These computational results demonstrate the importance of protons in this catalytic process. Many vanadium catalysts have been reported for a variety of oxidations: alcohol oxidations,[33] olefin epoxidation,[1,34-36] sulfide oxidation,[6,7,9,11,36] and phosphine oxidation.[1,8] Many of these processes use *in situ*-derived catalytic systems from vanadium starting materials, with vanadyl sulfate and vanadyl acetylacetonate being the most common, and with a variety of ligands. The reported rates and turnover numbers for sulfide oxidation are significantly lower than those presented for K[VO(O_2)Hheida], despite the similarities in coordination environments and terminal oxidant (hydrogen peroxide). The difference between other systems and the Hheida system is often the degree of protonation of the peroxo ligand; which as shown herein, decrease the activation barrier of the reaction and has experimentally been shown to increase the rate of reaction. To design better oxidation catalysts using vanadium, care should be taken to limit potential competitive protonation states. Additionally, steric bulk and H-bond acceptors should be added in such a way as to encourage selective protonation of one side of the peroxo ligand, thereby limiting the potential orientations that a pro-chiral sulfide can adopt in the linear S_N2 type transiton state. The computational results contained herein make it possible to design ligand sets capable of stereoselective oxidations using non-redox active d^0 metal-peroxo coordination complexes rationally.

Conclusion

The Pecoraro group has shown K[VO(O_2)Hheida] to be an effective functional model and biomimetic catalyst for thioether and halide oxidations. At the onset of this work two questions remained regarding the mechanism of

VHPO functional models: 1) the role of protonation in activation of the peroxo complex, and 2) the identity of the transition state. Density functional theory was used to explore the chemically feasible pre-catalytic species, protonation states, and transition state geometries. We have shown that coordination of the hydroxyl ethyl arm of Hheida is energetically favored over coordination of an exogenous donor such as acetonitrile or water. All chemically reasonable protonation states were examined based on the precatalytic species. These results showed that protonation of the peroxo moiety is favored over protonation of Hheida or the oxo ligand. Transition states were located for thioether and halide oxidations (halide = I^-, Br^-, and Cl^-), and all transition states were S_N2-like, with a nearly linear substrate-peroxo oxygen bond angles. Protonation of the peroxo moiety dramatically reduces the barrier to activation for both thioether and halides; however, barriers are insensitive to the identity of the halide. This further supports the hypothesis that the inability of K[VO(OOH)Hheida] to oxidize chloride is the result of the increasing basicity of the substrate, which leads to deprotonation of the catalytically active hydroperoxo species. Equivalents of acid beyond one proton per vanadium result in decomposition of the complex and inactivation of the halide with respect to nucleophilic attack on the complex. These results provide the necessary information regarding the transition state geometry and the importance of protons in the catalytic cycle to develop the class of catalysts based upon K[VO(OOH)Hheida] for asymmetric oxidations which will be discussed in Chapter 4.

References

1. Bolm, C. *Coord. Chem. Rev.* **2003**, *237*, 245-256.

2. Blum, S. A.; Bergman, R. G.; Ellman, J. A. *J. Org. Chem.* **2003**, *68*, 153-155.

3. Santoni, G.; Licini, G.; Rehder, D. *Chem. -- A Eur. J.* **2003**, *9*, 4700-4708.

4. Van de Velde, F.; Arends, I. W. C. E.; Sheldon, R. A. *J. Inorg. Biochem.* **2000**, *80*, 81-89.

5. Fernandez, I.; Khiar, N. *Chem. Rev.* **2003**, *103*, 3651-3705.

6. Smith, T. S.; Pecoraro, V. L. *Inorg. Chem.* **2002**, *41*, 6754-6760.

7. Barbarini, A.; Maggi, R.; Muratori, M.; Sartori, G.; Sartorio, R. *Tetrahedron: Asymm.* **2004**, 2467-2473.

8. Du, G.; Espenson, J. H. *Inorg. Chem.* **2005**, *44*, 2465-2471.

9. Jeong, Y.-C.; Choi, S.; Hwang, Y. D.; Ahn, K.-H. *Tetrahedron Lett.* **2004**, *45*, 9249-9252.

10. Plitt, P.; Pritzkow, H.; Kraemer, R. *Dalt. Trans.* **2004**, 2314-2320.

11. Sun, J.; Zhu, C.; Dai, Z.; Yang, M.; Pan, Y.; Hu, H. *J. Org. Chem.* **2004**, *69*, 8500-8503.

12. Colpas, G. J.; Hamstra, B. J.; Kampf, J. W.; Pecoraro, V. L. *J. Am. Chem. Soc.* **1994**, *116*, 3627-3628.

13. Colpas, G. J.; Hamstra, B. J.; Kampf, J. W.; Pecoraro, V. L. *J. Am. Chem. Soc.* **1996**, *118*, 3469-3478.

14. Hamstra, B. J.; Colpas, G. J.; Pecoraro, V. L. *Inorg. Chem.* **1998**, *37*, 949-955.

15. Siegbahn, P. E. M.; Blomberg, M. R. A. *Chem. Rev.* **2000**, *100*, 421-437.

16. Niu, S.; Hall, M. B. *Chem. Rev.* **2000**, *100*, 353-405.

17. Balcells, D.; Maseras, F.; Lledos, A. *J. Org. Chem.* **2003**, *68*, 4265-4274.

18. Balcells, D.; Maseras, F.; Ujaque, G. *J. Am. Chem. Soc.* **2005**, *127*, 3624-3634.

19. Butler, A.; Clague, M. J.; Meister, G. E. *Chem. Rev.* **1994**, *94*, 625-638.

20. Clague, M. J.; Keder, N. L.; Butler, A. *Inorg. Chem.* **1993**, *32*, 4754-4761.

21. Schneider, C. J.; Zampella, G.; Greco, C.; Pecoraro, V. L.; De Gioia, L. *Eur. J. Inorg. Chem.* **2007**, 515-523.

22. Becke, A. D. *Phys. Rev. A* **1988**, *38*, 3098-3100.

23. Schaefer, A.; Huber, C.; Ahlrichs, R. *J. Chem. Phys.* **1994**, *100*, 5829-5835.

24. Ahlrichs, R.; Baer, M.; Haeser, M.; Horn, H.; Koelmel, C. *Chem. Phys. Lett.* **1989**, *162*, 165-169.

25. Eichkorn, K.; Weigend, F.; Treutler, O.; Ahlrichs, R. *Theor. Chem. Acc.* **1997**, *97*, 119-124.

26. Eichkorn, K.; Treutler, O.; Oehm, H.; Haeser, M.; Ahlrichs, R. *Chem. Phys. Lett.* **1995**, *240*, 283-290.

27. Klamt, A. *J. Phys. Chem.* **1996**, *100*, 3349-3353.

28. Klamt, A. *J. Phys. Chem.* **1995**, *99*, 2224-2235.

29. Conte, V.; Di Furia, F.; Moro, S.; Rabbolini, S. *J. Mol. Catal.* **1996**, *113*, 175-184.

30. Conte, V.; Bortolini, O.; Carraro, M.; Moro, S. *J. Inorg. Biochem.* **2000**, *80*, 41-49.

31. Zampella, G.; Fantucci, P.; Pecoraro, V. L.; De Gioia, L. *J. Am. Chem. Soc.* **2005**, *127*, 953-960.

32. Slebodnick, C.; Pecoraro, V. L. *Inorg. Chim. Acta* **1998**, *283*, 37-43.

33. Li, C.; Zheng, P.; Li, J.; Zhang, H.; Cui, Y.; Shao, Q.; Ji, X.; Zhang, J.; Zhao, P.; Xu, Y. *Angew. Chem., Int. Ed. Engl.* **2003**, *42*, 5063-5066.

34. De la Pradilla, R. F.; Castellanos, A.; Fernandez, J.; Lorenzo, M.; Manzano, P.; Mendez, P.; Priego, J.; Viso, A. *J. Org. Chem.* **2006**, *71*, 1569-1575.

35. Hartung, J.; Drees, S.; Greb, M.; Schmidt, P.; Svoboda, I.; Fuess, H.; Murso, A.; Stalke, D. *Eur. J. Org. Chem.* **2003**, 2388-2408.

36. Ligtenbarg, A. G. J.; Hage, R.; Feringa, B. L. *Coord. Chem. Rev.* **2003**, *237*, 89-101.

Chapter 3

Spectroscopic Investigations of Protonated Peroxo-oxovanadium(V) Complexes: Elucidation of a Catalytic Intermediate

Introduction

As discussed in Chapter 1, peroxo-metal complexes are extremely efficient oxidation catalysts. Protonation of a side-on-bound peroxo activates the peroxide for nucleophilic oxidation by d^0 metal catalysts using Ti^{+4}, Mo^{+6}, W^{+6} and V^{+5}. Reduced-salen titanium(IV) complexes provide an interesting example of a proposed hydrogen bond activated peroxide[1] similar to what has been shown for *in silico* models of vanadium dependent haloperoxidases.[2] Reactivity studies with vanadium(V) tripodal amine compounds, including [$V^{+5}O(O_2)$Hheida], resulted in a proposal for the role of protonation in substrate oxidation.[3] Protonation plays a two-fold role in the activation of the complex by: 1) labilizing an oxo bond to facilitate the coordination of hydrogen peroxide,[4] and 2) activating the peroxide complex for oxo-transfer to the substrate (Figure 3.1).[3,5]

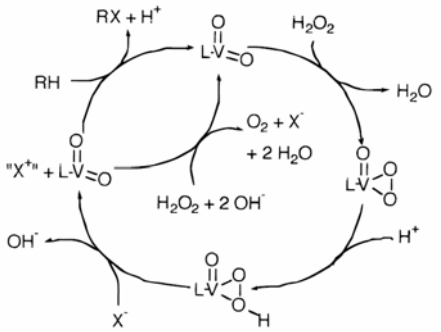

Figure 3.1: Proposed mechanism for halide oxidation by functional models of vanadium dependent haloperoxidases.[3]

While the proposed mechanism invokes a hydroperoxo species, the data available does not allow a specific assignment of the site of protonation nor the transition state geometry. DFT studies on the VHPO functional model, $[V^{+5}O(O_2)Heida]^{-1}$, discussed in Chapter 2 demonstrated that of the three most basic sites (oxo, peroxo, or carboxylate), protonation of the peroxo moiety was the energetically favored species with protonation of the oxo and the ligand carboxylate oxygens being higher in energy by 2.9 kcal/mol and 1.3 kcal/mol, respectively.[6] Transition states for substrate oxidation could only be located for oxo-transfer from the peroxo moiety. These results imply that protonation of the peroxo moiety is energetically favored and facilitates substrate oxidation; however, without experimentally identifying the protonated intermediates no definitive assignments regarding the role of protonation in catalysis can be made.

The intent of this work is to determine which of the protonated intermediates, discussed in Chapter 2, play a role in catalysis for the established functional model $K[VO(O_2)Hheida]$, using X-ray absorption near edge spectroscopy (XANES), FTIR, and Raman spectroscopies. XANES provides a sensitive probe of the electronic structure of transition metal complexes. The pre-edge feature, commonly assigned as a 1s→3d transition, can be used as a direct probe of electronic structure. This orbitally forbidden transition increases in intensity with the degree of metal 4p character that is hybridized with the 3d molecular orbitals. Previous work has shown metal-oxo complexes to have an abnormally large pre-edge feature.[7,8] As the degree of *d-p* hybridization is dependent on the geometry and the donor set,[9] a series of crystallographically characterized vanadium coordination complexes were explored to establish a trend in the pre-edge area with respect to V=O and $V\text{-}O_2$ bonding. This correlation allows us to examine if a peroxo-hydroxovanadium(+5) species, $[V(+5)(OH)O_2(Hheida)]$, is the catalytically relevant form of our functional model.

The XANES studies provide a direct probe of the metal-oxo bond but do not allow for the direct observation of changes in the peroxo or other ligand donors. Vibrational spectroscopies provide a complimentary analysis of the protonation state. The studies are aimed at identifying any protonated catalytic intermediates

for the oxidation of nucleophilic substrates by peroxo-oxovanadium(V) complexes.

Experimental Section

The following abbreviations are used in this chapter: **SALEN** = N,N'-Ethylenebis(salicylideneamine), **Hheida^{2-}** = N-(2-hydroxyethyl)iminodiacetate, **bpg^{-1}** = bis-pyridylgylcinate, **Tf^{-1}** = triflate, **XAS** = X-ray absorption spectroscopy, **XANES** = X-ray absorption near edge structure, **FTIR** = Fourier Transform Infrared Spectroscopy, **ATR** = attenuated total reflectance. All compounds used for vibrational spectroscopy are designated with the subscript (s) for solids and (acn) for acetonitrile solutions.

Synthesis

Triflic acid, hexafluorophosphoric acid, and 18-C-6 were purchased from Sigma Aldrich and used as received. Acetonitrile was degassed and passed through an alumina column. $H_2{}^{18}O_2$ was prepared from the autooxidation of $^{18}O_2$ with 9-ethylanthraquinol.[10] The following compounds were prepared as previously reported: VO(SALEN),[11] VCl_2SALEN,[12] VO(Hheida),[13] $VO(O_2)$BPG, and K[V(V)O(O_2)Hheida].[14] H[$VO(O_2)BPG]_2$Tf was prepared by a minor variation of a previously published procedure, slow evaporation of an acetonitrile solution yielded orange x-ray quality crystals.[3]

NH_4[VO_2Hheida]: V_2O_5 (5 mmol) was dissolved in H_2O (25 mL) by slow addition of NH_4OH while heating resulting a gray suspension, pH=9.4. N-2-hydroxyethyliminodiacetic acid (10.1 mmol) was added to the hot solution with stirring resulting in a yellow orange solution. The pH was adjusted to 5.0 with NH_4OH and the solution was filtered while hot. Ethanol (100ml) was added to the filtrate and stirred for 15 minutes. The resulting yellow solid was vacuum filtered, washed with cold ethanol, and dried *in vacuo*. Diffraction quality crystals

were obtained by recrystallization from water/ethanol mixtures at 23 C. Yield: 62% Elemental Analysis: **Found**(*Calc*) C – **26.10**(*26.13*), H – **4.75**(*4.83*), N- **10.05**(*10.15*), V – **17.6**(*18.5*) ESI^-/MS *m/z*: 258.5 (100.0%).

K[VO($^{18}O_2$)Hheida]: Substitution of $H_2{}^{18}O_2$ for normal isotopic abundance H_2O_2 yielded the ^{18}O substituted peroxide following the literature preparation.[14] $ESI\text{-}MS^-$ *m/z*: 278.4 (100%) 279.3 (0.6%), IR: $\nu_{C=O}$ 1631 cm^{-1}, $\nu_{V=O}$ 972 cm^{-1}, $\nu_{O\text{-}O}$ 872 cm^{-1}, and $\nu_{V\text{-}O2(asym)}$ 540 cm^{-1} ^{51}V NMR: -523 ppm.

H[VO($^{16}O_2$)Hheida]: K[VO($^{16}O_2$)Hheida] (1 mmol, 0.331 g) was dissolved in 10 mL $acetonitrile_{dry}$ under a positive pressure of N_2 with 18-C-6 (2 mmol) in a dry 50 mL schlenk flask. The resulting red solution was transferred into an inert atmosphere dry box. The solution was chilled in a liquid N_2 cold well until the solution began to freeze. HTf (1 mmol) was added to the cold solution and mixed thoroughly. The solution was allowed to stand for 1 hour at -30º C. The resulting orange-red precipitate was gravity filtered at -30º C and washed three times with 10 mL of cold $acetonitrile_{dry}$. The solid was transferred as an acetonitrile slurry to a product vial and dried *in vacuo*. ESI^-/MS *m/z*: 274.3 (100.0%), 275.3 (6.6%), FTIR: $\nu_{C=O}$ 1622 cm^{-1}, $\nu_{V=O}$ 963 cm^{-1}, $\nu_{O\text{-}O}$ 927 cm^{-1}, and $\nu_{V\text{-}O2(asym)}$ 571 cm^{-1}, ^{51}V NMR (ACN-d_3): -518 ppm.

H[VO($^{18}O_2$)Hheida]: Prepared in an analogous manner to H[VO(O_2)Hheida]. ESI^-/MS *m/z*: 278.2 (100.0%), 279.3 (9.3%), FTIR: $\nu_{C=O}$ 1628 cm^{-1}, $\nu_{V=O}$ 962 cm^{-1}, $\nu_{O\text{-}O}$ 879 cm^{-1}, and $\nu_{V\text{-}O2(asym)}$ 553 cm^{-1}

VOHheida•$2H_2O$[13] Elemental Analysis: **Found**(*Calc*) C – **25.81**(*25.91*), H – **4.71**(*4.71*), N- **4.93**(*5.04*), V – **17.2**(*18.3*)

VO(salen)[12] Elemental Analysis: **Found**(*Calc*) C – **57.61**(57.*45*), H – **4.24**(*4.36*), N- **8.44**(*8.41*), V – **13.6**(*15.29*)

VCl_2(salen)[12] Elemental Analysis: **Found**(*Calc*) C – **49.59**(49.51), H – **3.72**(*3.64*), N- **7.25**(*7.22*), V – **13.6**(*11.4*)

K[$VO(O_2)$Hheida][14] Elemental Analysis: **Found**(*Calc*) C – **21.56**(21.76), H – **2.06**(*3.35*), N- **4.03**(*4.23*), V – **14.4**(*14.59*)

Collection and Refinement of X-Ray Data

Suitable crystals of $NH_4[VO_2Hheida]$ (Figure 3.2) and $H[VO(O_2)bpg]_2Tf$ (Figure 3.3) were obtained by the methods described above. Crystals were mounted on a standard Bruker SMART APEX CCD-based X-ray diffractometer equipped with a low-temperature device and fine- focus Mo-target X-ray tube (λ = 0.71073 Å) operated at 2000 W power (50 kV, 30 m Å). The structures were solved and refined by Jeff W. Kampf, staff crystallographer in the chemistry department using a full-matrix least-squares refinement. All non-hydrogen atoms were refined anisotropically with hydrogen atoms placed in idealized positions. In the case of $H[VO(O_2)bpg]_2Tf$, the hydrogen involved in H-bonding was allowed to refine isotropically. All calculations were performed with the SHELXTL (version 6.12) software package, Additional information on the data collection and refinement are reported in Table 3.1.

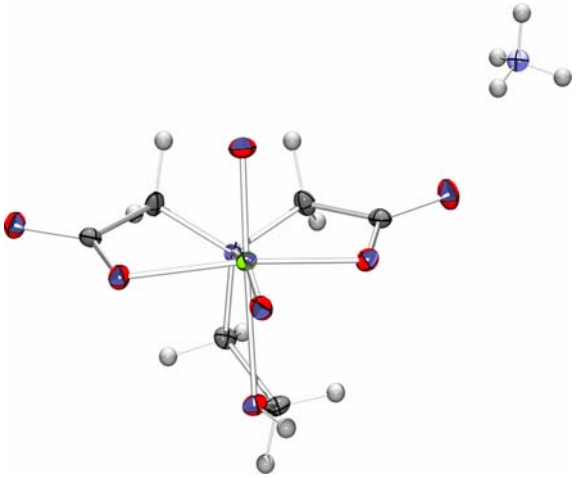

Figure 3.2: ORTEP diagram at 50% probability for $NH_4[VO_2Hheida]$.

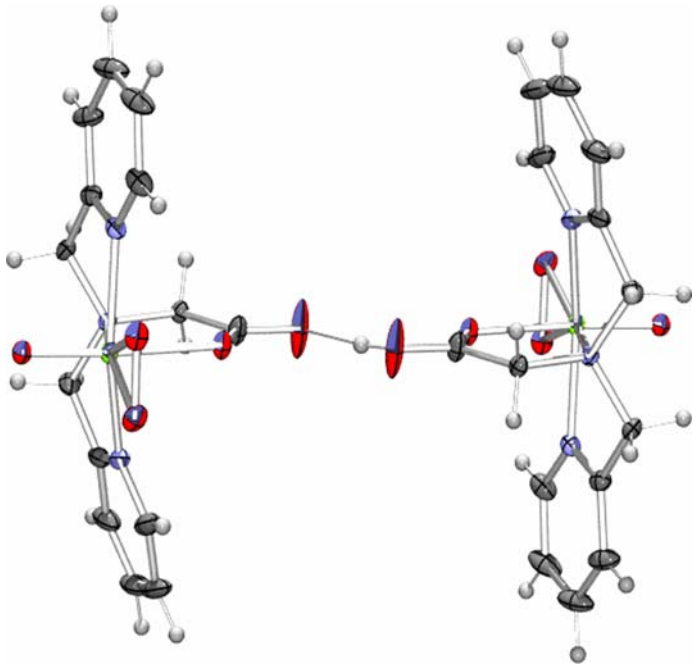

Figure 3.3: ORTEP diagram at 50% probability for $H[VO(O_2)bpg]_2Tf$. Triflate and acetonitrile are each disordered and have been omitted for clarity.

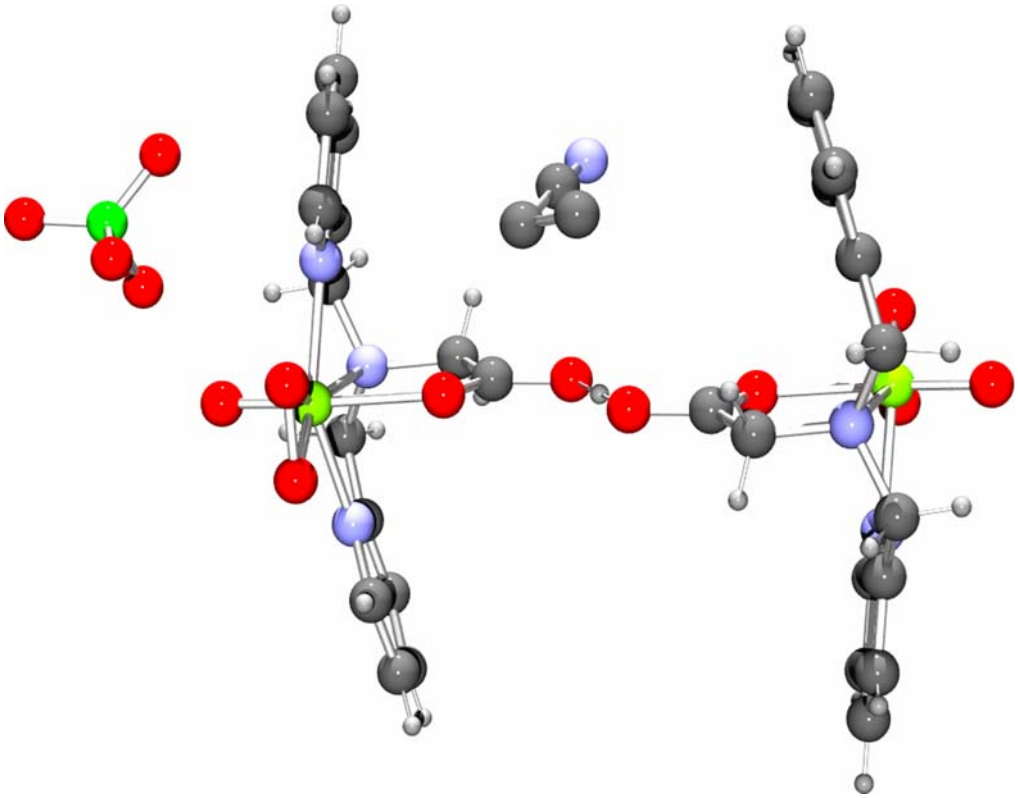

Figure 3.4: Ball and stick diagram of previously reported $H[VO(O_2)bpg]_2ClO_4$.[3]

Table 3.1: Structure Determination Summary

Compound	$NH_4[VO_2Hheida]$	$H[VO(O_2)bpg]_2Tf$
Empirical formula	$C_6H_{13}N_2O_7V$	$C_{33}H_{35}F_3N_8O_{13}SV_2$
Formula weight	276.12	942.63
Crystal Description	yellow block	orange block
Crystal system, space group	Monoclinic	Monoclinic
Space Group	P2(1)/c	P2(1)/c
Z	8	2
a (Å)	20.340(6)	13.6867(14)
b (Å)	7.644(2)	12.9132(13)
c (Å)	14.309(4)	12.4668(13)
α (deg)	90	90
β (deg)	109.437(7)	114.142(1)
γ (deg)	90	90
Volume ($Å^3$)	2098.0(10)	2010.7(4)
Temperature (K)	108(2)	85(2)
Data / restraints / parameters	7558 / 0 / 330	5700 / 79 / 348
Wavelength (Å)	0.71073	0.71073
Absorption coefficient (mm^{-1})	0.970	0.603 mm^-1
R	0.0693	0.0360
wR^2	0.2152	0.0984
Goodness-of-fit on F^2	1.083	1.103

X-ray absorption measurements

X-ray absorption data were collected at SSRL BL9-3, the spectra were normalized[13] and the pre-edge area fit using a pseudo-Voigt method. All samples were prepared from crystalline compounds with the exception VCl_2(salen). All solids were diluted with boronitride and stored at room temperature under N_2.

Solution Sample:

K[VO(O_2)Hheida]: K[VO(O_2)Hheida] (0.025 mmol) was dissolved in 10 mL acetonitrile. 0.5 mL of the stock solution was transferred to the XAS sample holder and flash frozen with liquid nitrogen. Catalytic activity was tested by monitoring the consumption of thioanisole at 290nm as previously described.[5] UV-Vis absorption (LCMT): λ_{max}: 448 ε: 420 M^{-1} cm^{-1}

H[VO(O_2)Hheida]*:* Hexafluorophosphoric acid (1eq, 2.5 umol) was added to 1 mL of K[VO(O_2)Hheida] (2.5 mM). A 0.5 mL aliquot was flash frozen in the XAS sample holder; the remaining 0.5 mL was tested for catalytic oxidation of thioanisole as previously described.[5] UV-Vis absorption (LCMT): λ_{max}: 450 nm ε: 341 M^{-1} cm^{-1}

Vibrational Spectroscopy

FTIR measurements were performed with both KBr pellets and attenuated total reflectance (ATR) using a Perkin-Elmer Spectrum BX FTIR. Solution measurements were carried with an ATR accessory with a ZnSe crystal. Solid state measurements were performed using standard KBr pellets. Spectrophotometric grade KBr was dried at 110º C prior to use. Hygroscopic samples were prepared in a dry box. FTIR-ATR solutions were prepared using an 18-C-6 stock solution in acetonitrile. All FTIR data was background substract using the appropriate KBr pellet or 18-C-6 acetonitrile solutions as appropriate. Normalization of the data was performed after background substraction. The ESI^-/MS of solution samples were performed before data collection to ensure the integrity of the sample. Attempts were made to numerically integrate the intensity of the IR spectrum to compare the protonated and unprotonated forms of [VO(O_2)Hheida]$^-$. However, contamination from acetonitrile and the triflate anion in the protonated samples prevented a valid comparison of integrated signal intensities between the unprotonated and protonated forms of the complex. Consequently, the vibrational transitions discussed in this chapter are reported based on the energy of the transition and the approximate line shape (b = broad, s = strong, w = weak).

All Raman spectroscopy was performed in collaboration with Prof. Nicolai Lehnert at the University of Michigan with the assistance of Mary Grace I. Galinato, Ph.D. Data collection was carried out using a Newport Ar/Kr Ion Laser

tunable from 350 nm to 676 nm with a Princeton instruments TriVista model 555AS spectrophotometer and a Spec-10 $N_{2(l)}$-cooled CCD detector. Raman spectra were collected at 77K in a custom quartz sample holder. Three different excitation wavelengths (413.55 nm, 457.98 nm, and 514.55 nm) with varying laser intensity (10 mW to 30 mW) were employed. Optimal signal to noise was obtained using a 514.55 nm excitation frequency with a 30 mW power. Exposure time and scan counts varied based on the intensity of the background scattering. Optimal exposure time for solid samples was 20 seconds with 49 acquisitions averaged for each spectrum. Solid samples were prepared from vacuum dried crystalline samples and ground thoroughly before placing the sample in a quartz EPR tube. Solution samples were prepared at varying concentrations, although only samples greater than 10 mM [V] had significant signal intensity. All samples were stored in liquid nitrogen immediately after sample preparation and stored in a dewar until data collection.

Other Instrumentation

Electrospray mass spectrometry was performed on a Micromass LCT Time-of-Flight mass spectrometer with Electrospray and APCI. Elemental analysis was performed by the University of Michigan Microanalysis Laboratory. ^{51}V NMR was carried out on a Varian MR400 400 MHz spectrophotometer with a Varian 5mm PFG AutoX Dual Broadband probe.

Results

Comments on Synthesis

All compounds can be prepared in a straightforward manner as reported in their respective references. Care needed to be in the preparation of $NH_4[VO_2Hheida]$ to ensure that all materials are filtered hot to remove any

uncomplexed vanadium pentoxide. Failure to do so can result in the formation of decavanadate.

The protonated complex H[VO(O_2)Hheida] is significantly less soluble in acetonitrile than the corresponding potassium salt. At concentrations higher than 2 mM, H[VO(O_2)Hheida] precipitates as an extremely hygroscopic red-orange solid. The resulting solid is stable at -30º C in a dry box for 24 hours. All H[VO(O_2)Hheida] measurements were made on solid samples no older than four hours and solutions were prepared immediately before data collection. KBr and the sample were ground in a dry box, loaded into the pellet press and dried for 30 minutes *in vacuo* prior to pressing the pellet.

X-ray Absorption Spectroscopy

Table 3.2: Pre-edge areas obtained from a pseudo-voigt fit for all compounds examined in this study. [a] = experimental error is estimated at ±40.

Compound	Ox. State	V=O	Donor Set	C N	Area[a]	V=O Dist (Å)
$VCl_2(SALEN)_{(s)}$	4	0	O_2N_2	6	239	---
$VO(SALEN)_{(s)}$	4	1	O_2N_2	5	600	1.586
$VO(Hheida)_{(s)}$	4	1	O_3N	6	387	1.601
$K[VO(O_2)Hheida]_{(s)}$	5	1	O_3N	7	496	1.602
$K[VO(O_2)Hheida]_{(acn)}$	5	1	O_3N	7	441	1.602
$H[VO(O_2)Hheida]_{(acn)}$	5	1	O_3N	7	440	---
$[NH_4VO_2Hheida]_{(s)}$	5	2	O_3N	6	729	1.657, 1.635Å

The x-ray absorption near edge structure spectra were collected for the compounds listed in Table 3.2. All data was referenced to vanadium foil and normalized following the procedure of Weng and co-workers.[15] The pre-edge intensity was fit using a pseudo-voigt method after normalization, the summary of which can be found in Table 3.2. Comparisons between VO(salen) and VCl_2(salen) were made to determine the contribution of a vanadium-oxo bond to the pre-edge intensity within similar ligand environments. VCl_2(salen) shows a 60% decrease in the intensity of the pre-edge feature when compared to VO(salen) (Figure 3.5). Hydrolysis of VCl_2(salen) can lead to the generation of

VO(salen). Therefore, VCl_2(salen) samples were stored with a desiccant until data collection. It is important to emphasize that the reported pre-edge area may contain some contribution from traces of VO(salen). An inspection of the reported pre-edge intensities for a variety of vanadium systems revealed a dramatic variance in the intensity of this spectral feature as it is strongly correlated to the identity of the donor set, geometry and presence of trans-ligands to the oxo.[9] Three oxovanadium complexes of Hheida were analyzed, oxovanadium(IV), peroxo-oxovanadium(V) and dioxovanadium(V). The oxovanadium(IV) pre-edge area is 12% less intense than the peroxo-oxovanadium(V) complex. In contrast, the dioxovanadium(V) pre-edge area is approximately 1.5 times larger than the corresponding oxovanadium(IV) and peroxo-oxovanadium(V) (Figure 3.6). Minimal variations were observed between solid and acetonitrile solubilized samples of peroxo-oxovanadium(V) Hheida (K[$VO(O_2)$Hheida]) (Figure 3.7). The protonated peroxo-oxovanadium(V) complex (H[$VO(O_2)$Hheida]) was catalytically competent for sulfide oxidation prior to flash freezing the sample in the XAS sample holder. No differences in the pre-edge areas or positions were observed between the unprotonated (K[$VO(O_2)$Hheida]) and protonated [H[$VO(O_2)$Hheida] complexes (Figure 3.8 and Figure 3.9).

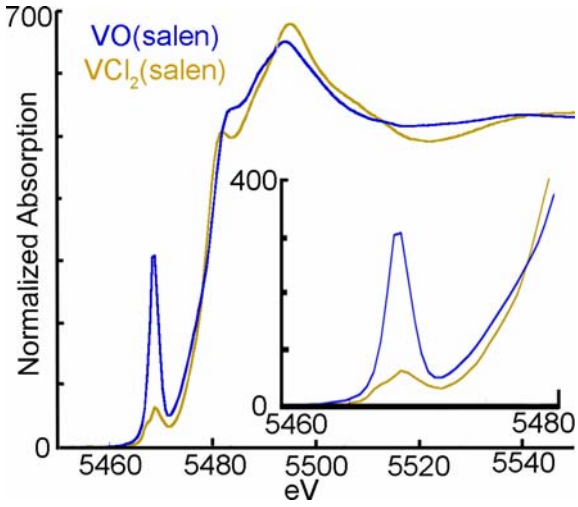

Figure 3.5: X-ray absorption near edge spectra comparing mono-oxo and non-oxo vanadium species with identical donor sets. Inset: expanded pre-edge region.

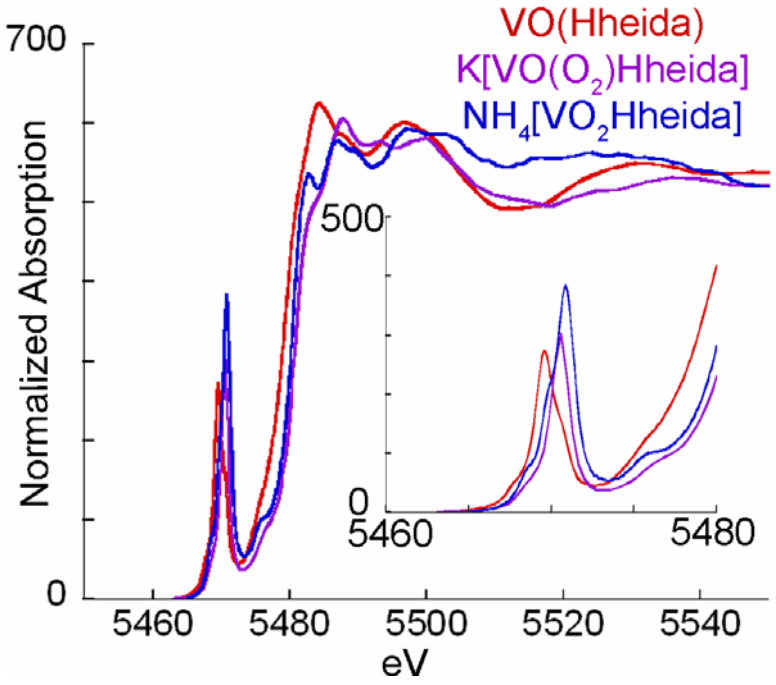

Figure 3.6: X-ray absorption near edge spectra comparing mono-oxo and dioxo vanadium species with identical donor sets. Inset: expanded pre-edge region.

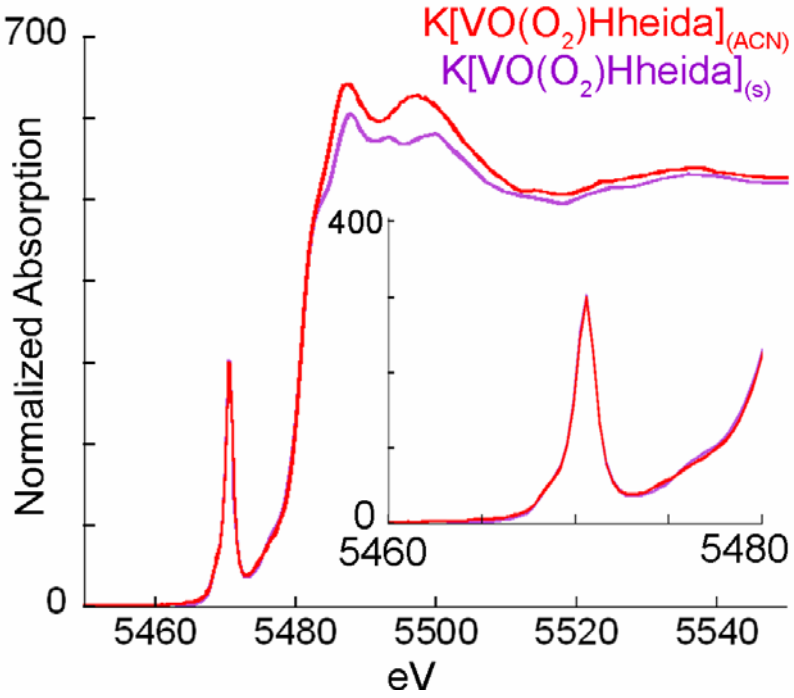

Figure 3.7: X-ray absorption near edge spectra comparing K[$VO(O_2)$Hheida] in the solid state and solubilized in acetonitrile with 2eq. 18-C-6 (2.5 mM [V]). Inset: expanded pre-edge region.

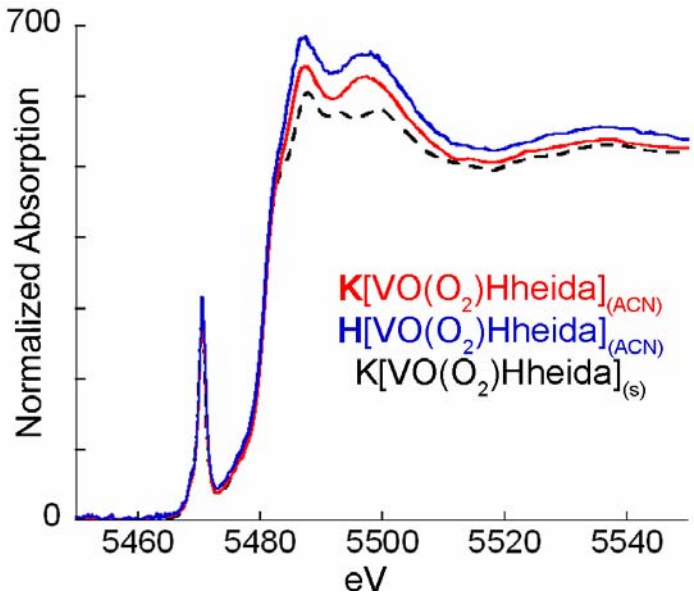

Figure 3.8: XANES spectra comparing K[VO(O_2)Hheida] in the solid state (black, dotted), solubilized in acetonitrile with 2eq. 18-C-6 (2.5 mM [V]) (red), after addition of 1 eq. of HPF_6 (blue).

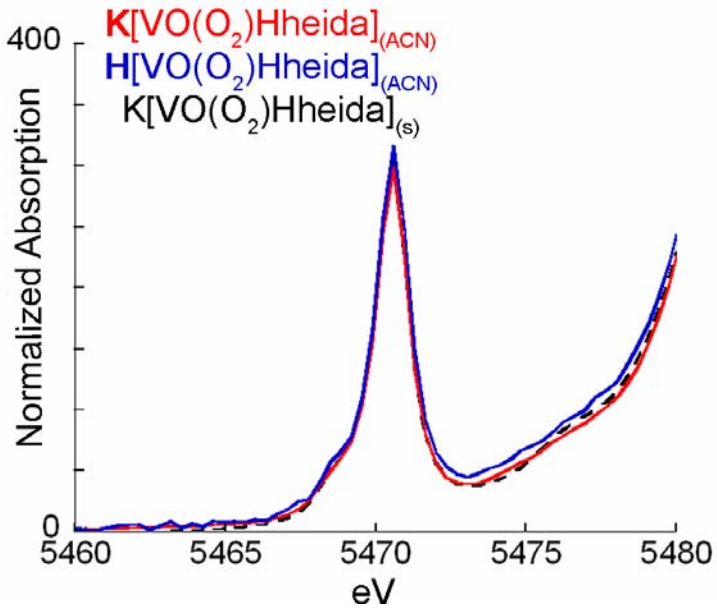

Figure 3.9: Pre-edge region of the XANES spectra of K[VO(O_2)Hheida] in the solid state (black, dotted), solubilized in acetonitrile with 2eq. 18-C-6 (2.5 mM [V]) (red), after addition of 1 eq. of HPF_6 (blue).

Vibrational Spectroscopy

Protonation of a carboxylate donor

The crystallographically characterized protonated carboxylate complex $H[VO(O_2)bpg]_2Tf$ (Tf = triflate) was used to determine the effects of ligand protonation the carboxylate stretching region. $H[VO(O_2)bpg]_2^+$ was previously reported as its perchlorate salt.[3] Given the potential hazards associated with metal perchlorate salts, the triflate salt was synthesized for these studies. The X-ray structure for $H[VO(O_2)bpg]Tf$ shows a strong hydrogen bond bridging the carboxylates of the ligand set (Figure 3.3), as was true for the perchlorate salt. As can be seen in Table 3.3 substitution of a triflate anion for perchlorate does not significantly change the bond distances of any of the first coordination sphere donors. The hydrogen-bonded dimer has a bond distance of 2.44 Å between the uncoordinated carboxylate oxygen atoms. The structure of $H[VO(O_2)bpg]_2Tf$ is identical to that of the previously reported perchlorate salt.

Isotope labeling of the peroxo-oxygen atoms with ^{18}O allowed for the assignment of peroxide stretching frequencies at $\nu_{V\text{-}O2(asym)}$ = 570 cm^{-1} and $\nu_{O\text{-}O}$ = 946 cm^{-1} (Figure 3.10). The remaining stretching modes were assigned as $\nu_{C=O}$ = 1627 cm^{-1} and $\nu_{V=O}$ = 930 cm^{-1}. Upon protonation of the carboxylate donor no shifts are observed in the peroxo vibrational bands, while a +11 cm^{-1} shift is observed in the $\nu_{V=O}$ (941 cm^{-1}) (Figure 3.11) and two bands appear in the $\nu_{C=O}$ stretching region (1711 and 1611 cm^{-1}) (Figure 3.12).

Table 3.3 Relevant bond distances for the Tf^- and ClO_4^- salts of $H[VO(O_2)bpg]_2^+$

Bond	Tf^- (Å)	ClO_4^- (Å)
V=O	1.604(5)	1.607(6)
$V\text{-}O_p$	1.861(5)	1.854(6)
$V\text{-}O_p$	1.863(5)	1.865(6)
$V\text{-}O_c$	2.139(5)	2.138(6)
$V\text{-}N_{py}$	2.137(6)	2.142(8)
$V\text{-}N_{py}$	2.145(5)	2.147(6)
$V\text{-}N_{tert}$	2.202(5)	2.207(6)
$C\text{-}O_{coord}$	1.242(8)	1.250(9)
$C\text{-}O_{uncord}$	1.264(8)	1.268(9)
O--H--O	2.442(12)	2.441(14)

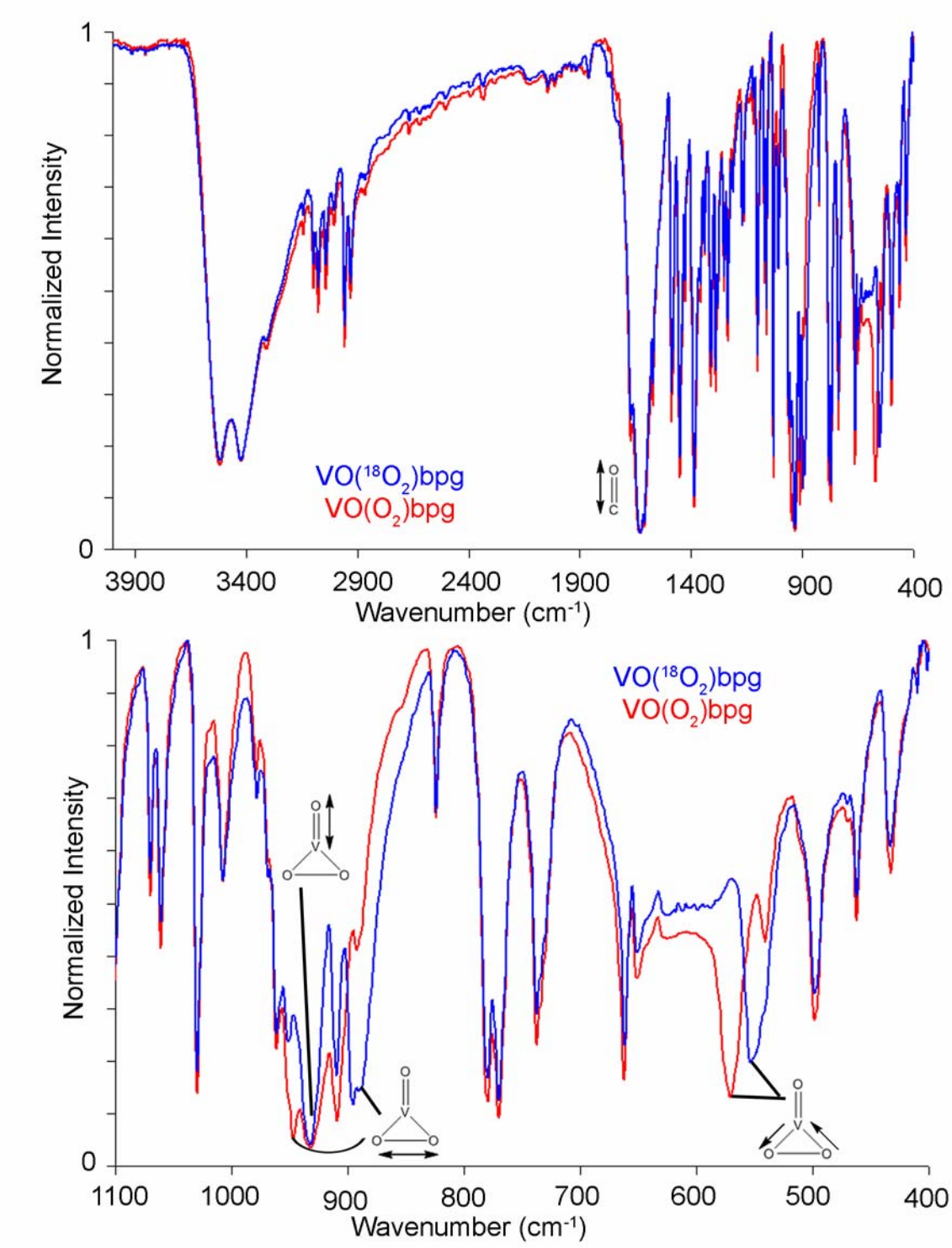

Figure 3.10: IR spectra of solid VO($^{18}O_2$)bpg (blue) and VO(O_2)bpg (red) over the full spectral range (top) and an expansion of the V=O and V-O_2 region (bottom)

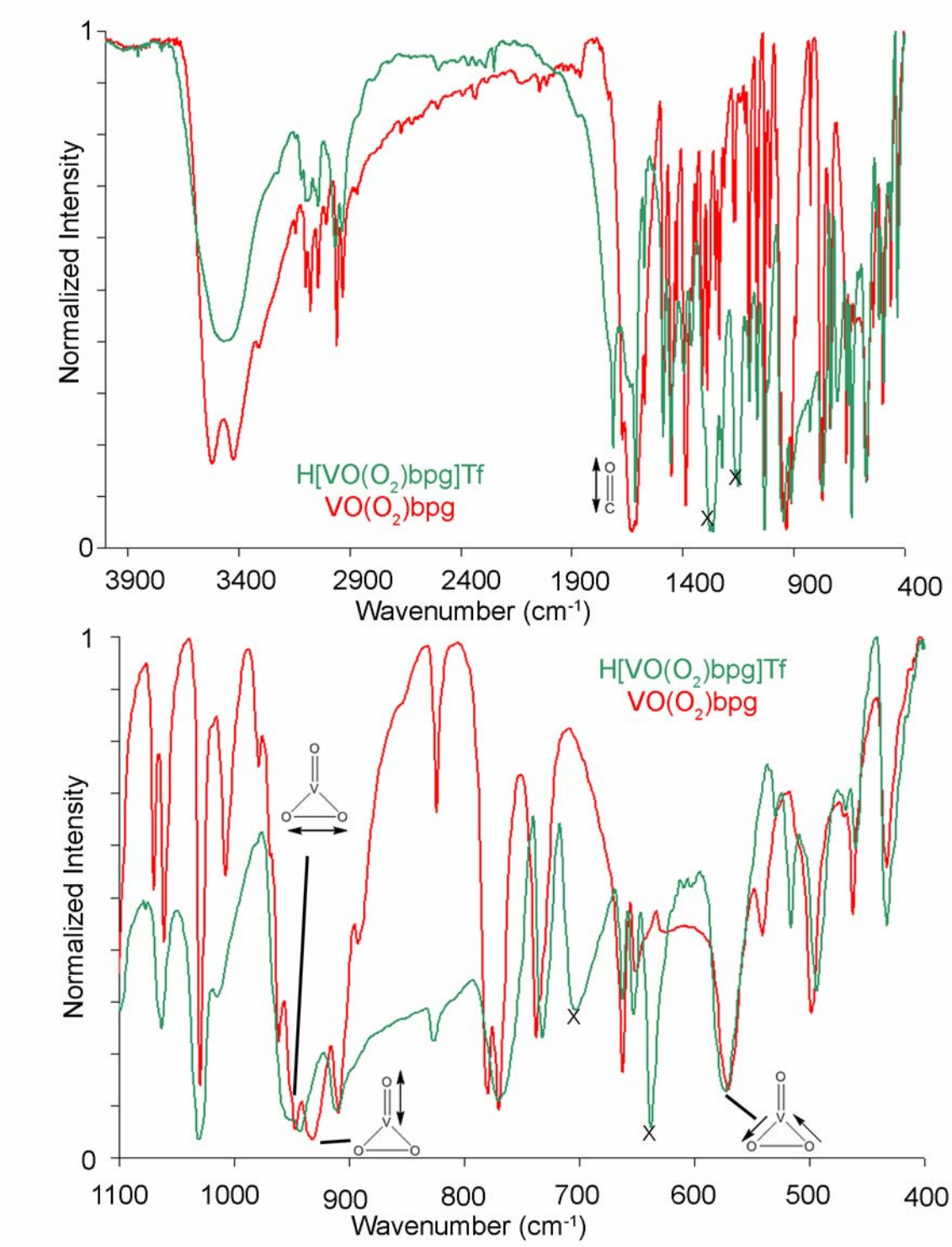

Figure 3.11: IR spectra of solid H[VO(O_2)bpg]Tf (green) and VO(O_2)bpg (red) over the full spectral range (top) and an expansion of the V=O and V-O_2 region (bottom). Peaks marked with an x arise from the triflate counterion.

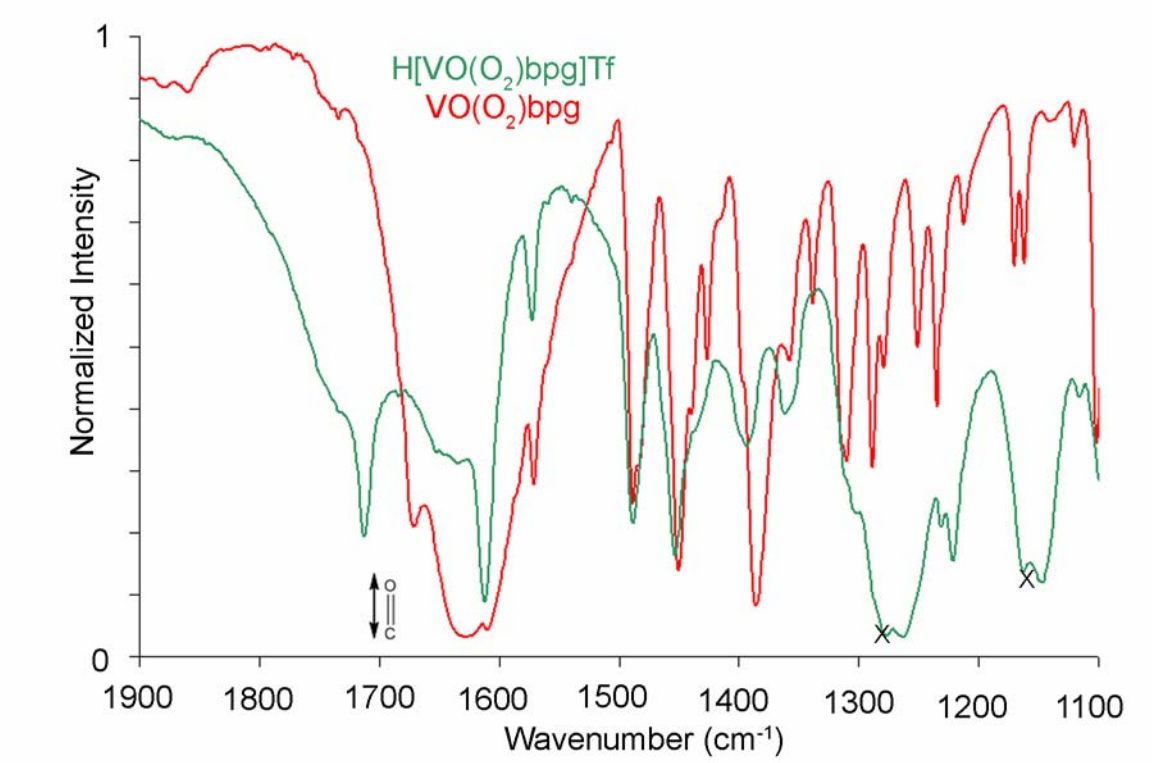

Figure 3.12: IR spectra of solid H[VO(O_2)bpg]Tf (green) and VO(O_2)bpg (red) in the carboxylate stretching region. Peaks marked with an x arise from the triflate counterion.

Identification of solution and solid state vibrational bands for K[VO(O_2)Hheida]

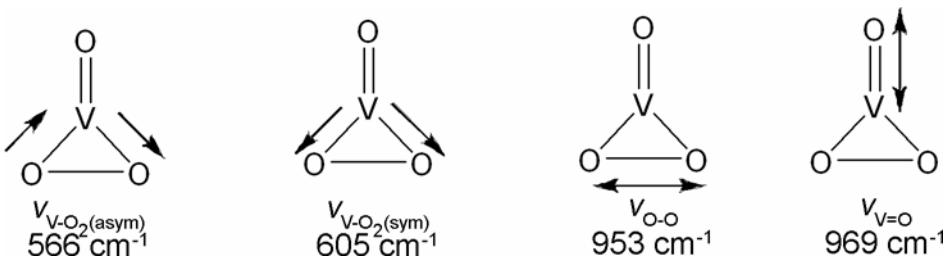

Figure 3.13: Calculated vibrational frequencies for the geometry-optimized [VO(O_2)Hheida]$^-$.

Vibrational frequencies for [VO(O_2)Hheida]$^-$ were obtained from frequency calculations of the geometry-optimized structure from Chapter 1. The gas phase calculated stretching frequencies for $\nu_{V=O}$, ν_{O-O}, $\nu_{V-O2(sym)}$, and $\nu_{V-O2(asym)}$ are

presented in Figure 3.13. Isotope labeling studies with hydrogen peroxide allowed for the definitive assignment of the peroxo-related vibrational bands (Figure 3.14) and a correlation was made with the calculated vibrational frequencies. The $\nu_{O\text{-}O}$, $\nu_{V=O}$, and $\nu_{V\text{-}O2(asym)}$ were assigned as 924 cm^{-1}, 972 cm^{-1}, and 568 cm^{-1}, respectively. The carboxylate stretching frequency appears at 1627 cm^{-1}, within the expected range for coordinated carboxylate donors. Dilute solution measurements of K[VO(O_2)Hheida] (2.5 mM [V], 5 mM 18-C-6) were possible using FT-IR with an ATR sample cell. Moderate shifts were observed in the V=O and peroxo stretches upon dissolution of the complex into acetonitrile-d_3 ($\nu_{C=O}$ = 1658 cm^{-1}, $\nu_{O\text{-}O}$ = 927 cm^{-1}, and $\nu_{V=O}$ = 963 cm^{-1}) (Figure 3.14). The $\nu_{V\text{-}O2(asym)}$ was not observed due to background absorption from the ZnSe crystal used in the ATR measurements. Deuterated acetonitrile was used to shift the solvent related vibrational bands out of the V=O and O-O stretching region. Background corrections were made by subtracting the spectrum of 2.5 mM 18-C-6 in acetonitrile-d_3. Minor variations in the observed vibrational bands for acetonitrile and 18-C-6 upon dissolution of K[VO(O_2)Hheida] resulted in glitches in the ATR spectrum as seen in Figure 3.15. Solution measurements of ^{16}O-^{16}O and ^{18}O-^{18}O isotopes confirmed the assignments of the vibrational bands assigned based on solid state measurements (Figure 3.16).

Attempts to utilize resonance enhancement of the Raman-active vibrations met with little success. The low extinction coefficient of the peroxo-vanadium charge transfer excitation (λ-max: 448 nm ε: 420 M^{-1} cm^{-1}) did not afford resonance enhancement at examined excitation wavelengths (413.15nm, 457.98, and 514.55 nm). The Raman spectra collected using an excitation frequency of 514.5 nm provided the best signal/noise ratio. Isotope labeling of peroxide for K[VO(O_2)Hheida] confirmed the presence of the peroxo and oxo vibrational bands ($\nu_{O\text{-}O}$ = 922 cm^{-1}, and $\nu_{V=O}$ = 973 cm^{-1}, $\nu_{V\text{-}O2(asym)}$ = 575) (Figure 3.17). Solution measurements using Raman spectroscopy were hindered by the low solubility of K[VO(O_2)Hheida] and the strong absorbance of acetonitrile. Vibrational band assignments could be made for 11.48 mM [V] solutions (Figure 3.18) and are consistent with the assignments made with FTIR-ATR.

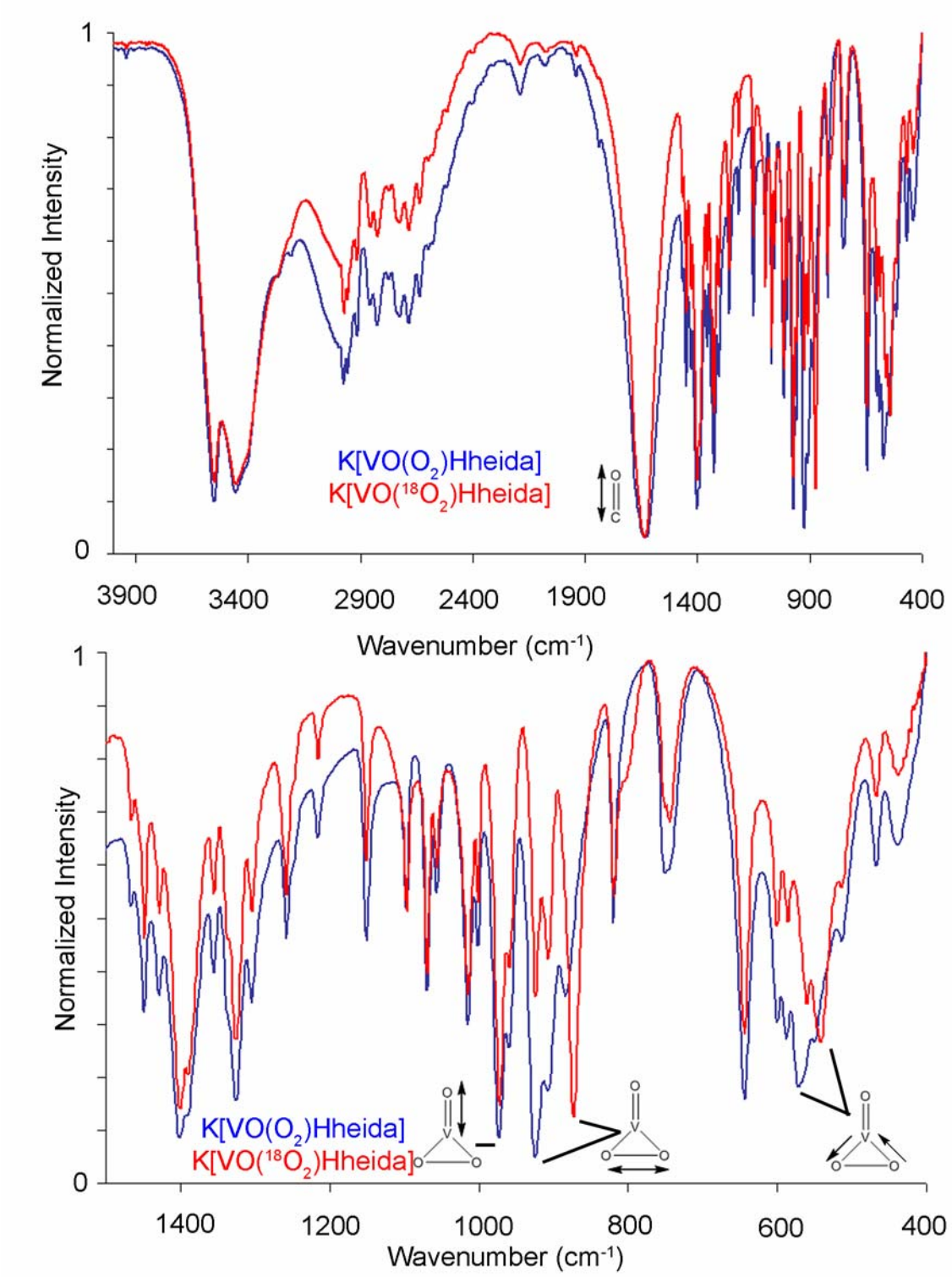

Figure 3.14: IR spectra of solid K[VO(O_2)Hheida] (blue) and K[VO($^{18}O_2$)Hheida] (red) over the full spectral range (top) and an expansion of the V=O and V-O_2 region (bottom)

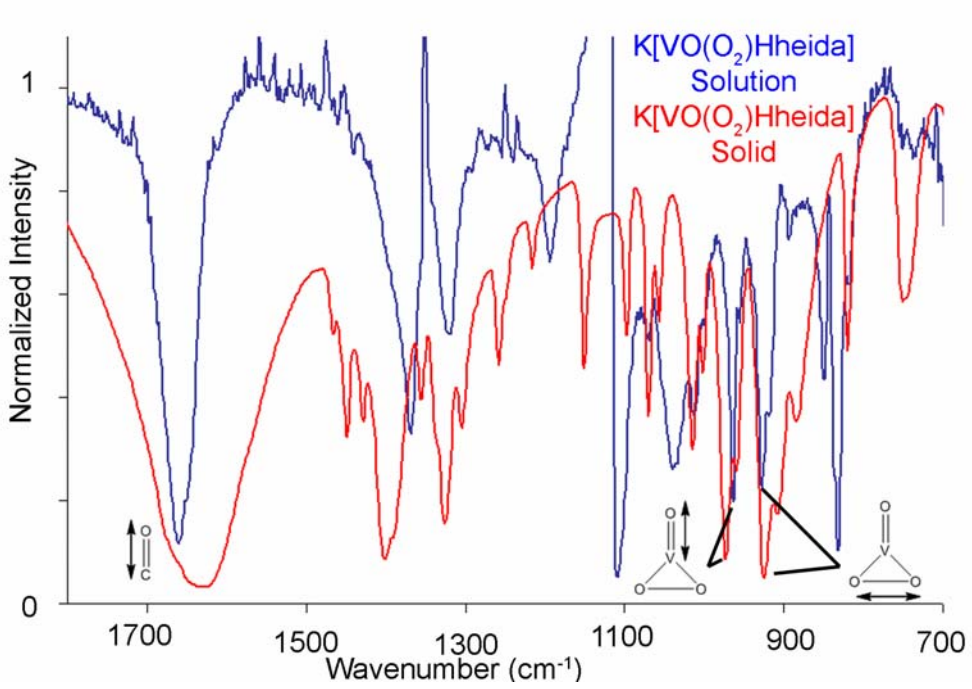

Figure 3.15: Normalized IR spectra comparing solution versus solid state species of K[VO(O_2)Hheida].

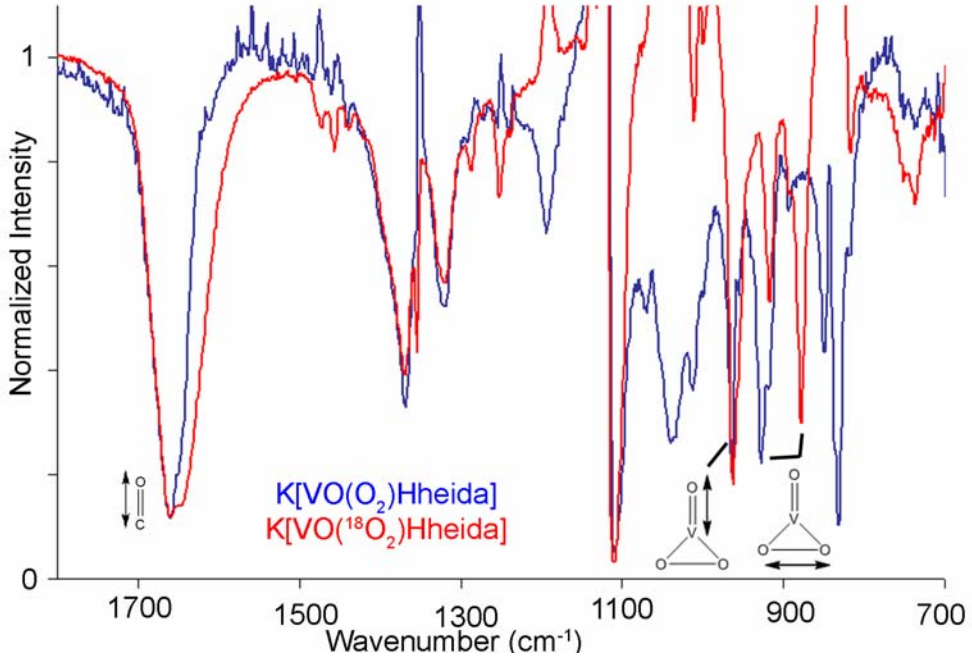

Figure 3.16: Normalized FT-IR:ATR spectra in 2.5mM acetonitrile-d_3 of K[VO(O_2)Hheida] (blue) and K[VO($^{18}O_2$)Hheida] (red). Glitches due to baseline subtraction of acetonitrile-d_3 and 18-C-6: 1353 cm^{-1}, 1121 cm^{-1}, 844 cm^{-1}, and 1732 cm^{-1}.

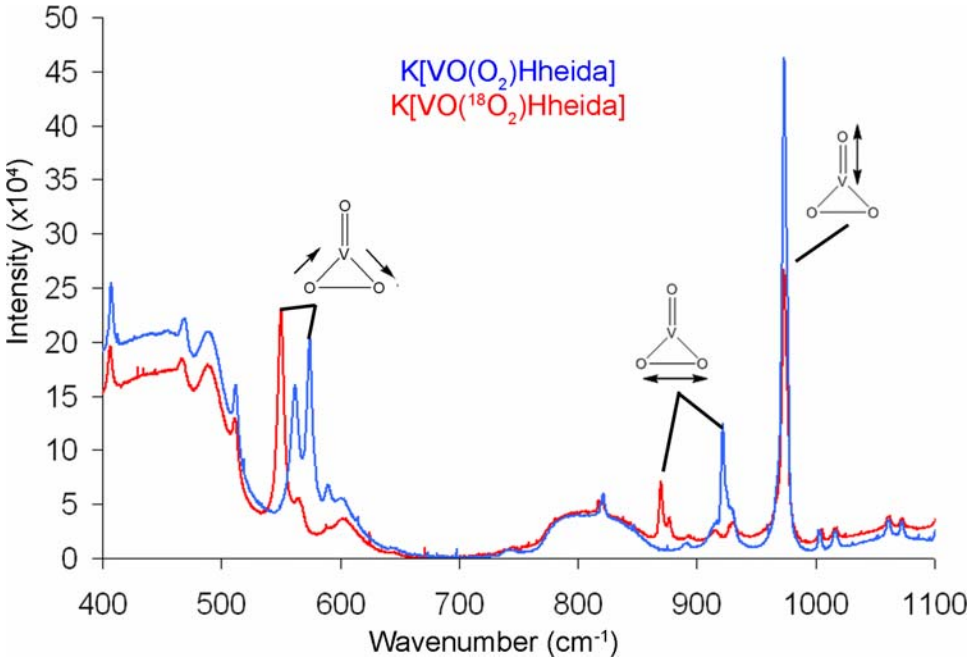

Figure 3.17: Raman spectra of solid K[VO(O_2)Hheida] (blue) and K[VO($^{18}O_2$)Hheida] (red).

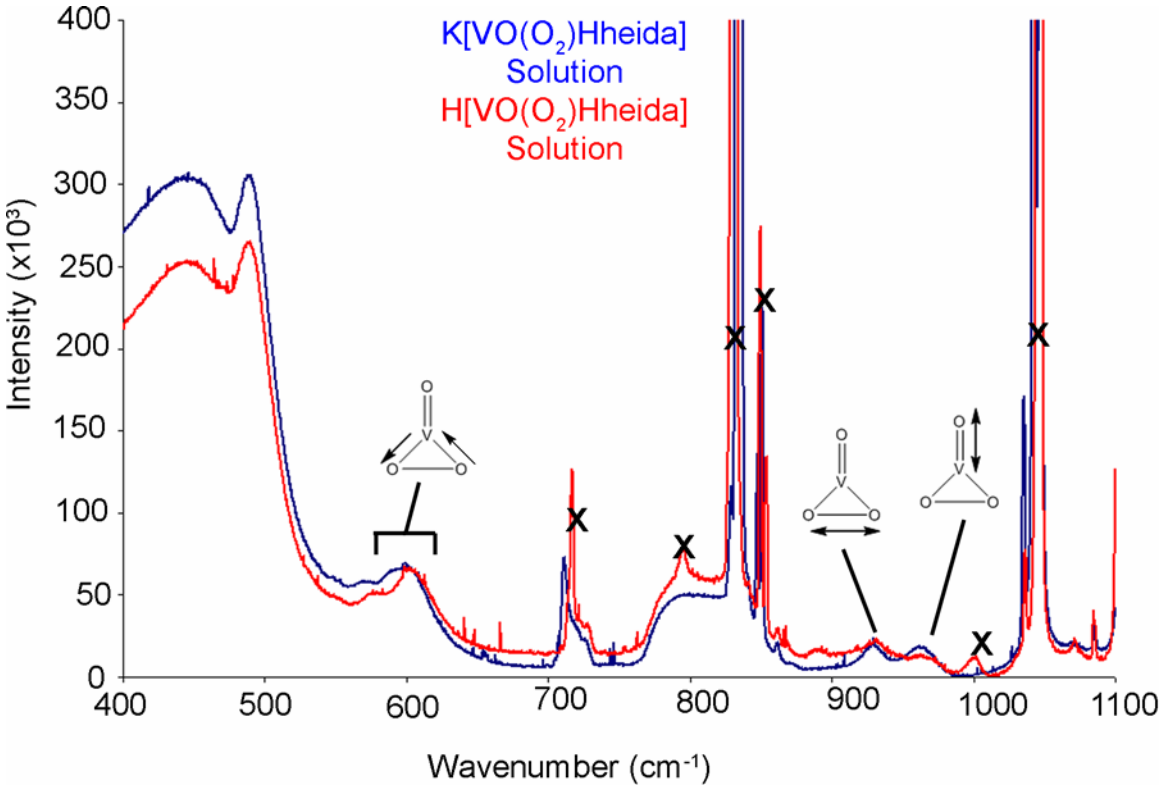

Figure 3.18: Raman spectra of 11.48 mM K[VO(O_2)Hheida] in acetonitrile-d_3 (blue) and 11.48 mM H[VO(O_2)Hheida] in acetonitrile-d_3 (red). Peaks marked with an **x** arise from acetonitrile and triflate.

Effects of protonation on the vibrational spectrum of $[VO(O_2)Hheida]^-$

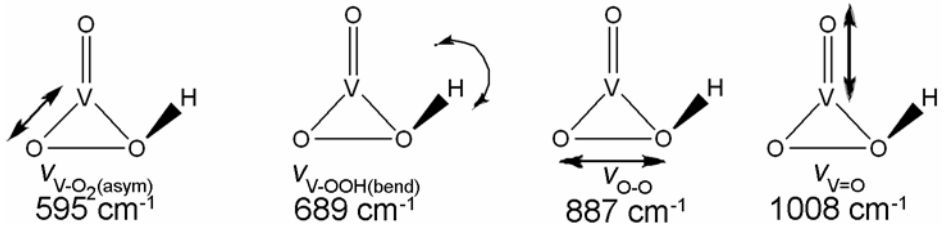

Figure 3.19: Calculated vibrational frequencies for the geometry optimized $[VO(OOH)Hheida]^-$.

Calculated vibrational modes for a hydroperoxo species were obtained from the frequency calculations of VO(OOH)Hheida performed in Chapter 2. Figure 3.19 depicts the changes in the vibrational frequencies for a hydroperoxo species. Within the calculated vibrational modes no symmetric V-O_2 stretching frequency could be located; however, a new O-O-H bending motion was found. Protonation of K[$VO(O_2)$Hheida] with triflic acid under anhydrous conditions generates H[$VO(O_2)$Hheida] which at concentrations higher than 2.5 mM precipitates as a solid. The isolation of H[$VO(O_2)$Hheida] allowed for the complete removal of the triflate anion by rinsing with cold acetonitrile as was evident by the absence of *m/z*: 149 in the negative ion mode mass spectrum.

The observed spectral changes do not correlate with the calculated vibrational modes for a fully protonated V(OOH) species. The carboxylate stretching region shows a slight broadening and a shift of -5 cm^{-1} upon protonation. The oxo and peroxo vibrational bands broaden and show shifts of similar magnitudes: $\Delta\nu_{V=O}$ = -9 cm^{-1}, $\Delta\nu_{O\text{-}O}$ = +3 cm^{-1}, and $\nu_{V\text{-}O2(asym)}$ = +3 cm^{-1}, all of which are within or close to the 2 cm^{-1} resolution of the instrument (Figure 3.20). Identical shifts were observed upon protonation of an ^{18}O-labelled peroxo complex (Figure 3.21). A new vibrational band appears upon protonation at 704 cm^{-1}. To probe whether this vibrational modes was attributable to proton bending motion as predicted by the calculations, $Dheida^{2-}$ and DTf were used to generate D[$VO(O_2)$Dheida]. No change is observed in the new vibration at 704 cm^{-1} upon

deuteration (Figure 3.22). Dilute acetonitrile solutions measurements were possible using the FTIR-ATR instrument. The $\nu_{C=O}$ stretching frequency broadens and the peak center shifts -55 cm^{-1} with respect to solubilized K[VO(O_2)Hheida] (Figure 3.23). In contrast, the $\nu_{V=O}$ and ν_{O-O} vibrations broaden but do not shift (Figure 3.23). The V=O and peroxo stretching for H[VO(O_2)Hheida] show identical shifts in acetonitrile and the solid state (Figure 3.24). A summary of vibrational frequencies for all compounds is available in Table 3.4.

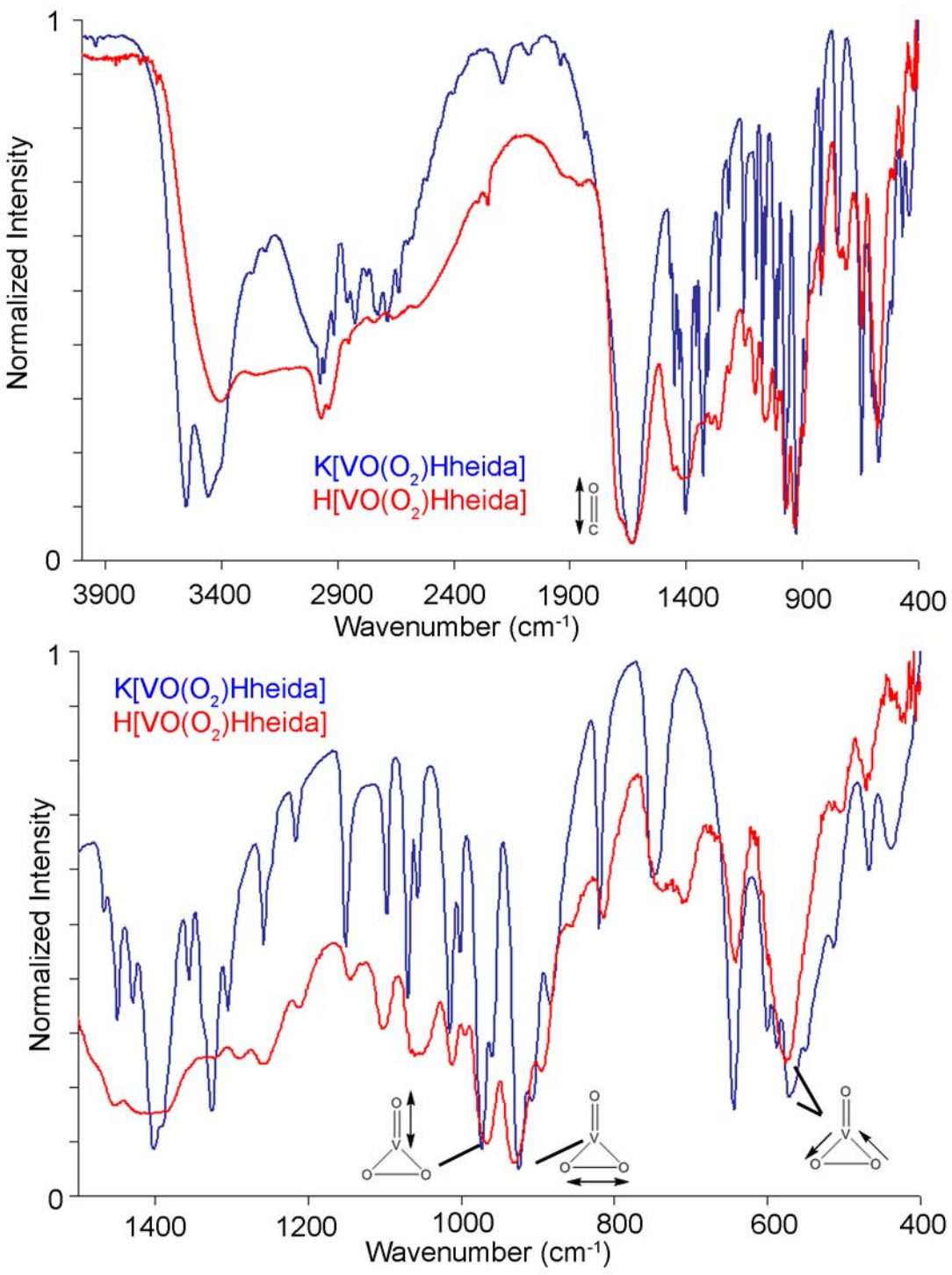

Figure 3.20: IR spectra of solid K[VO(O_2)Hheida] (blue) and H[VO(O_2)Hheida] (red) over the full spectral range (top) and an expansion of the V=O and V-O_2 region (bottom)

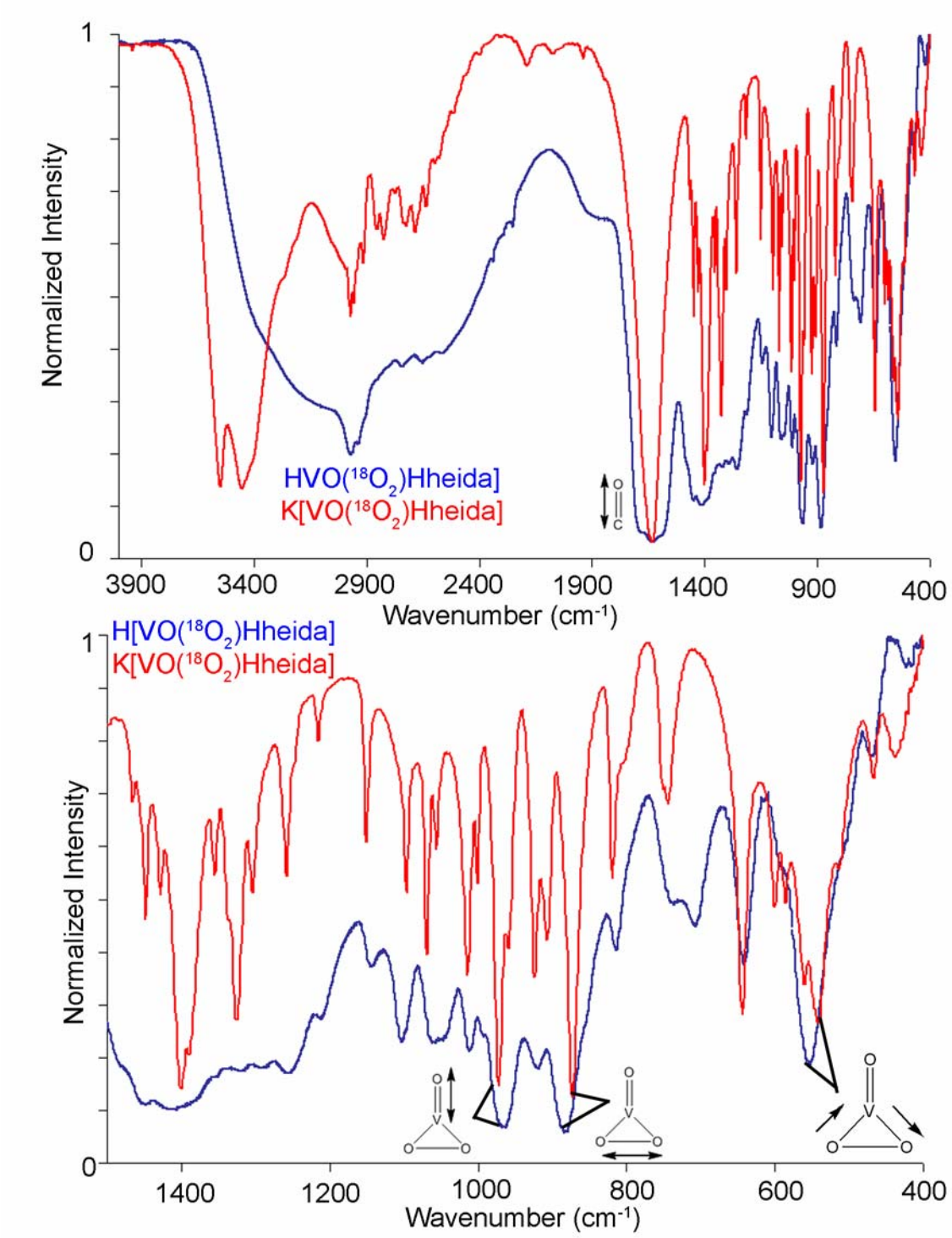

Figure 3.21: IR spectra of solid H[VO($^{18}O_2$)Hheida] (blue) and K[VO($^{18}O_2$)Hheida] (red) over the full spectral range (top) and an expansion of the V=O and V-O_2 region (bottom).

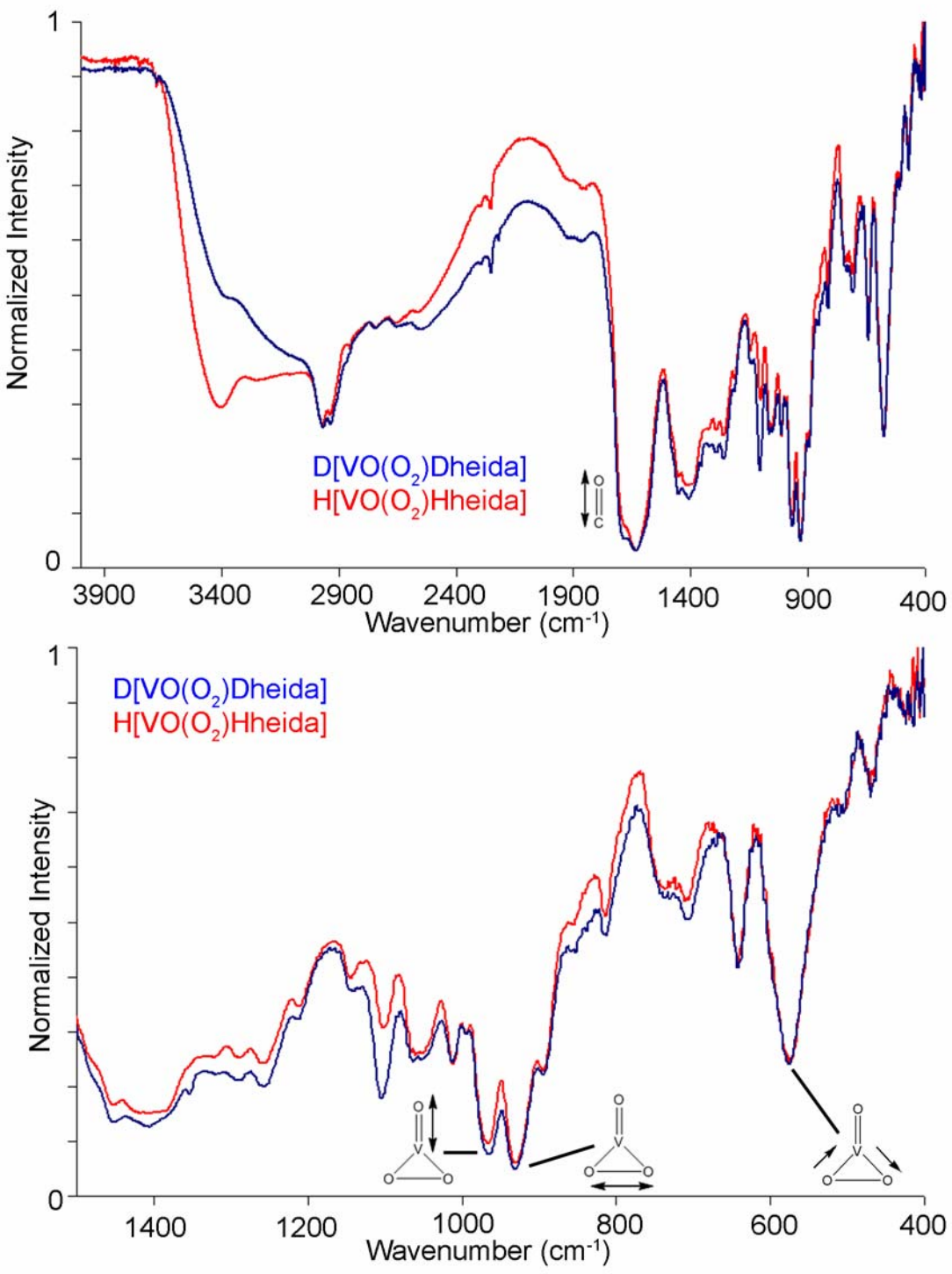

Figure 3.22: IR spectra of solid D[VO(O_2)Dheida] (blue) and H[VO(O_2)Hheida] (red) over the full spectral range (top) and an expansion of the V=O and V-O_2 region (bottom).

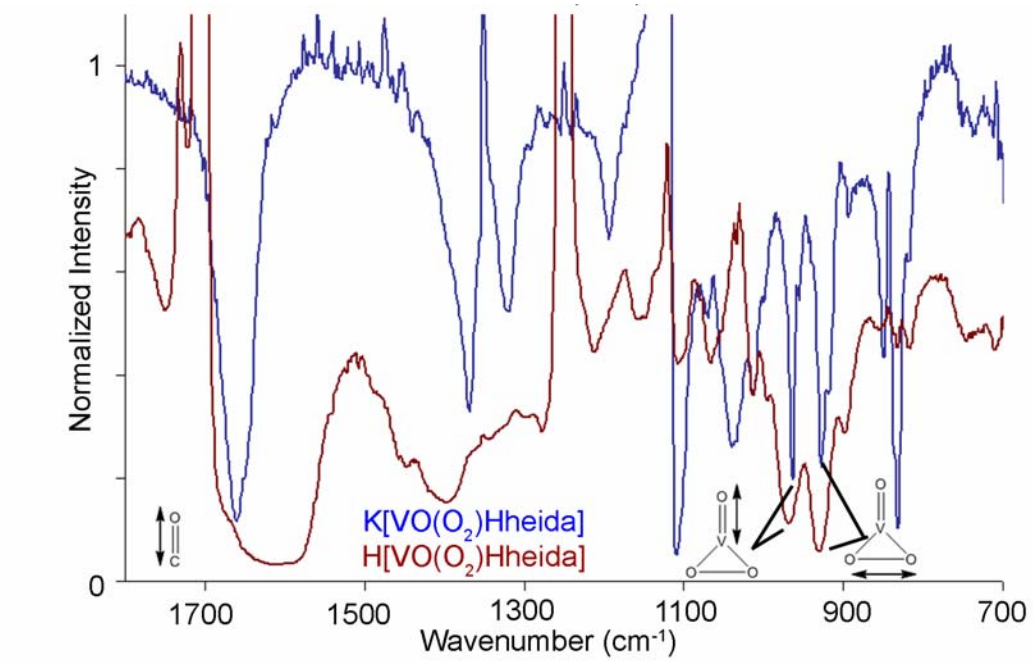

Figure 3.23: Normalized FT-IR:ATR spectra in 2.5mM acetonitrile-d_3 of K[VO(O_2)Hheida] and H[VO(O_2)Hheida]. Glitches due to baseline subtraction of acetonitrile-d_3 and 18-C-6: 1353 cm^{-1}, 1121 cm^{-1}, 844 cm^{-1}, and 1732 cm^{-1}.

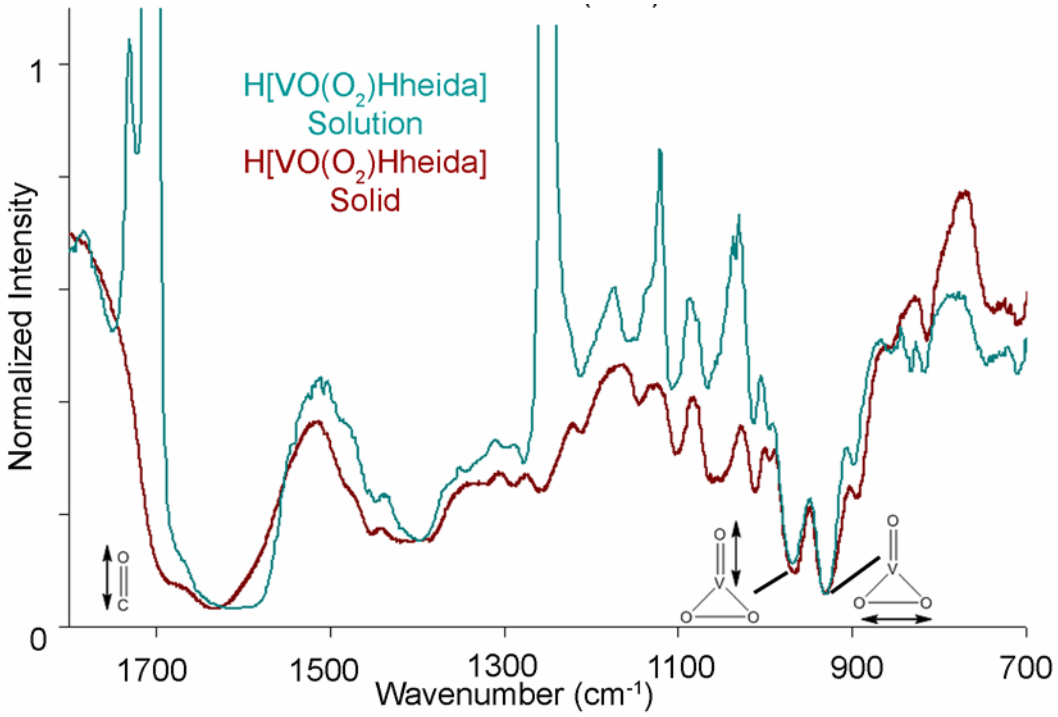

Figure 3.24: Normalized IR spectra comparing a 2.5mM solution versus solid state spectra of H[VO(O_2)Hheida].

Table 3.4: Observed vibrational bands for all compounds explored in this study. [a]Vibrational mode corresponds to a O-O-H bending motion. [b]Peak position is approximate due to spectral resolution.

Compound	IR/Raman	$^{16}O/^{18}O$ Peroxide	H/D	$\nu_{C=O}$ (cm-1)	$\nu_{V=O}$ (cm-1)	ν_{O-O} (cm-1)	$\nu_{V-O2(sym)}$ (cm-1)	$\nu_{V-O2(asym)}$ (cm-1)
$VO(O_2)bpg$	IR-KBr Pellet	^{16}O	---	1627	930	946	---	570
$VO(^{18}O_2)bpg$	IR-KBr Pellet	^{18}O	---	1627	930	895	---	552
Predicted Istope Shift		$^{16}O \rightarrow ^{18}O$			*890*	*892*		*545*
H$[VO(O_2)bpg]_2Tf$	IR-KBr Pellet	^{16}O	H	1711, 1611	941	946	---	571
$[VO(O_2)Hheida]^{-1}$	Calculated	^{16}O	---	---	969	953	605	557
K$[VO(O_2)Hheida]_{(s)}$	IR-KBr Pellet	^{16}O	---	1627	972	924	---	568
K$[VO(^{18}O_2)Hheida]_{(s)}$	IR-KBr Pellet	^{18}O	---	1631	972	872	---	540
Predicted Istope Shift		$^{16}O \rightarrow ^{18}O$			*930*	*871*		*543*
K$[VO(O_2)Hheida]_{(acn)}$	IR-ATR	^{16}O	---	1658	963	927	---	---
K$[VO(^{18}O_2)Hheida]_{(acn)}$	IR-ATR	^{18}O	---	1657	962	877	---	---
$[VO(OO\mathbf{H})Hheida]$	Calculated	^{16}O	H		1008	887	689[a]	595
H$[VO(O_2)Hheida]_{(s)}$	IR-KBr Pellet	^{16}O	H	1622	963	927	---	571
H$[VO(^{18}O_2)Hheida]_{(s)}$	IR-KBr Pellet	^{18}O	H	1628	962	879	---	553
D$[VO(O_2)Dheida]_{(s)}$	IR-KBr Pellet	^{16}O	D	1622	961	927	---	573
H$[VO(O_2)Hheida]_{(acn)}$	IR-ATR	^{16}O	H	1603	964	927	---	---
K$[VO(O_2)Hheida]_{(s)}$	Raman	^{16}O	---	---	973	922	---	575
K$[VO(^{18}O_2)Hheida]_{(s)}$	Raman	^{18}O	---	---	973	870	---	550
K$[VO(O_2)Hheida]_{(acn)}$	Raman	^{16}O	---	---	966	932	---	---[b]
H$[VO(O_2)Hheida]_{(acn)}$	Raman	^{16}O	H	---	966[b]	933[b]	---	---[b]

Discussion

X-ray absorption spectroscopy

The pre-edge feature in the X-ray absorption spectrum has previously been employed as a probe of metal ligand covalency.[9,16] In the case of metal-oxo complexes, this 1*s*-3*d* transition is abnormally large in comparison to non-oxo systems and is polarized along the M=O bond. The abnormally large pre-edge peak has been attributed to hybridization of metal centered 4*p* orbitals with the 3*d* orbitals, thereby relaxing the orbital angular momentum selection rule. Previous attempts to correlate the pre-edge intensity of vanadium complexes with oxo bonding showed a complex relationship that is dependent on geometry, donor set, and the presence of a trans ligand to the oxo bond.[9] This work focuses on correlating the pre-edge intensity with oxo bonding using crystallogrpahically characterized vanadium coordination compounds with identical donor sets and similar geometries.

Vanadium(IV) salen complexes were employed to test the correlation of oxo-bonding with pre-edge intensity. Oxovanadium(IV) salen is a penta-coordinated complex with the N_2O_2 donor set of the ligand occupying the equatorial plane of the molecule. The corresponding dicholoro species can be synthesized by the addition of dry HCl gas yielding VCl_2(salen). A comparison of $V^{+4}O$(SALEN) and $V^{+4}Cl_2$(SALEN) shows a 60% decrease in the pre-edge area, confirming the correlation between pre-edge area and V=O bonding. This is consistent with a reduction in the degree of π-bonding that consequently necessitates the mixing of metal centered 4*p* orbitals with 3*d* orbital set.

An estimation of the contribution of the peroxo moiety to the pre-edge feature was necessary to ensure that additional π-bonding form this donor does not significantly enhance the pre-edge area. The contribution of the peroxo donor to the pre-edge intensity was examined using $V^{+4}O$(Hheida), $NH_4[V^{+5}O_2$(Hheida)], and $K[V^{+5}O(O_2)$Hheida]. These complexes allow for a comparison of the effects of oxo and peroxo bonding on the pre-edge intensity. The *cis*-dioxo complex,

$NH_4[V(+5)O_2(Hheida)]$, showed the largest pre-edge area, consistent with the increased π-bonding due to the second metal-oxo bond. In comparison to the mono-oxovanadium(IV) complex the pre-edge area for the *cis*-dioxo is 1.88 times more intense. The V=O bond lengths obtained from the crystal structure of $[NH_4VO_2Hheida]$ are 1.657 Å and 1.635 Å, whereas for the VOHheida complex the V=O bond distance is 1.601 Å. Despite the higher oxidation state of the dioxovanadium(V) the V=O bonds are longer than the oxovanadium(IV) case. This indicates that the V=O bonds in the *cis*-dioxo species have less π-bonding character peroxo than the mono-oxovanadium(IV) species. Consequently, the area of the pre-edge feature for a VO_2 species should not double with respect to the mono-oxo case. Replacement of an oxo donor by a peroxo group reduced the pre-edge area by 32%. This decrease is consistent with the loss of the π-bonding associated with a displaced oxo donor. The mono-oxo and oxo-peroxo complexes, $V^{+4}OHheida$ and $[V^{+5}O(O_2)Hheida]^{-1}$, have similar pre-edge areas indicating that addition of a side-on bound peroxo donor coordinated cis to the V=O bond does not significantly affect the π-bonding associated with oxo donor, nor does it form molecular orbitals with significant 4p character.

Recent studies on Mn^{+5}=O species have estimated a 3-fold decrease in pre-edge area upon protonation of a Mn^{+5}=O.[16] This provides an estimate for the amount of change expected for a complete stoichiometric protonation of $K[VO(O_2)Hheida]$ to form $VOH(O_2)Hheida$. The approximate cumulative error associated with determining the pre-edge area is 10%. These two estimates provide a lower limit to amount of a protonated oxo species that is detectable. Given the 66% decrease in the pre-edge area upon protonation of an oxo bond and a 10% error in the pre-edge determination, the generation of 0.2 stochiometric equivalents of a V-OH species should be greater than the error associated with the pre-edge area determination. In order to determine if greater than 20% of V=O bond is protonated in the catalytically active species, spectra were collected for frozen solutions of $K[VO(O_2)Hheida]$ and $H[VO(O_2)Hheida]$. A comparison of the solid state and solution spectra of $K[VO(O_2)Hheida]$ revealed that changes in the pre-edge were within experimental error (Table 3.2). To

ensure the integrity of the K[$VO(O_2)$Hheida], both the red-shift in the charge transfer band of the UV-Visible spectrum and the catalytic oxidation of thioethers were tested prior to sample freezing. As is apparent from Figure 3.9, there is no appreciable change in the pre-edge area upon protonation of the complex. Given the sensitivity of the pre-edge area to the structure, we conclude that the degree of oxo-bonding to the vanadium center has not been altered, and thus less than 20% of a protonated oxo species is present in solution. This provides the first spectroscopic evidence that protonation of the oxo moiety does not occur significantly under catalytic conditions.

Vibrational Spectroscopy

The computational studies in chapter 2 found three sites of protonation for [$VO(O_2)$Hheida] that are close in energy. While a hydroperoxo species was the most stable, other energetically accessible protonation were found. A protonated oxo species was 2.9 kcal/mol higher energy and a protonated uncoordinated carboxylate oxygen was 1.4 kcal/mol higher in energy, than the most stable hydroperoxo species. As the calculation presented in Chapter 2 do not explicity account for solvation effects or hydrogen bonding, the energetic differences between protonation states are likely exaggerated. The X-ray absorption results above provide a strong indication that protonation of the V=O does not occur to a significant extent under catalytic conditions. The vibrational spectroscopic studies in this section are focused directly probing whether protonation of the uncoordinated carboxylate or the peroxo donor are viable catalytic intermediates and provide a complimentary spectroscopic verification of the results obtained from the XAS measurements.

To determine the effects of carboxylate protonation on the vibrational spectrum for peroxo-oxovanadium(V) complexes a crystallographically characterized example of a protonated carboxylate peroxo-oxovanadium(V) complex, H[$VO(O_2)$bpg]$_2$Tf was synthesized by a minor variation of the literature procedure.[3] The neutral $VO(O_2)$bpg complex contains two pyridyl in the

equatorial plane and one carboxylate donor in the equatorial plane. When protonated, $VO(O_2)$bpg crystallizes as a dimer with a bridging proton between the uncoordinated carboxylate oxygens. The *trans* influence of the oxo donor increases the electron density on the carboxylate thus making it more basic than a carboxylate coordinated *cis* to the oxo-moiety. For this study we employed triflic acid as our proton source and subsequently crystallized the triflate salt of the protonated dimer to ensure that changes in the counterion did not alter the formation of proton bridged dimer (Figure 3.3). The structure of $H[VO(O_2)bpg]_2Tf$ is identical to that observed for the perchlorate salt,[3] indicating that the identity of the counterion has little effect on the vanadium complex (Figure 3.4 and Table 3.3). Substitution of ^{18}O labeled peroxide resulted in shifts of $\Delta\nu_{O\text{-}O}$ = -51 cm^{-1} and $\Delta\nu_{V\text{-}O2(asym)}$ = -18 cm^{-1} which are consistent with the changes in the reduced mass as predicted for a simple harmonic oscillator $\Delta\nu_{O\text{-}O}$ = -54 cm^{-1} and $\Delta\nu_{V\text{-}O2(asym)}$ = -21 cm^{-1}. The carboxylate and V=O stretching frequencies fall within the expected range for vanadium complexes, $\nu_{C=O}$ = 1627 cm^{-1} and $\nu_{V=O}$ = 930 cm^{-1}.[17] Upon formation of the protonated bridge dimer complex there is dramatic reduction in the intensity of the carboxylate band resulting in two peaks at 1711 cm^{-1} and 1611 cm^{-1}. The formation of these two vibrational bands is consistent with protonation of a carboxylate donor reducing the delocalization of electrons across both oxygen. Protonation of the carboxylate weakens the carboxylate oxygen bond, thereby shifting the V=O vibrational frequency by 11 cm^{-1}. This is shift is consistent with an increase the oscillator strength of the V=O bond due to the reduce electron donating abilities of protonated trans carboxylate donor. No changes are observed in the peroxo stretching frequencies. Additionally, the observed changes in the carboxylate stretching frequency are consistent with the X-ray structure which has a proton bridging two carboxylate donors with a C=O--O=C bond distance of 2.44 Å. This information provides a discrete spectroscopic signature to assist in identification of protonated uncoordinated carboxylates in $[VO(O_2)Hheida]^-$.

Identification of solution and solid state vibrational bands for K[VO(O_2)Hheida]

The assignment of the vibrational bands associated with the peroxo donor was accomplished by ^{18}O labeling of the peroxo donor for both solid state and solution measurements. Upon substitution of ^{18}O peroxide two vibrational bands shifted $\Delta\nu_{O\text{-}O}$ = -52 cm^{-1} and $\Delta\nu_{V\text{-}O2(asym)}$ = -28 cm^{-1} which are consistent with the reduced mass predictions of $\Delta\nu_{O\text{-}O}$ = -53 cm^{-1} and $\Delta\nu_{V\text{-}O2(asym)}$ = -25 cm^{-1}. The V=O and carboxylate vibrations were assigned as $\nu_{C=O}$ = 1627 cm^{-1} and $\nu_{V=O}$ = 972 cm^{-1}. Assignments of the peroxo and oxo vibrational modes were made based on a frequency calculation of the geometry optimized [VO(O_2)Hheida]$^-$. Calculations demonstrate two stretching modes of the vanadium peroxide bound corresponding to a symmetric and an asymmetric stretch of V-O bond (Figure 3.13), where the former is a composite mode and includes vibrations of Hheida^{2-}. The calculated values correlate well with the observed V=O stretching frequency but deviate by 29 cm^{-1} and 14 cm^{-1} for the assigned $\Delta\nu_{O\text{-}O}$ and $\Delta\nu_{V\text{-}O2(asym)}$ (Table 3.4). As the values are calculated for a gas phase ion, they do not account for electrostatic interaction of a potassium counterion in the solid state. This can be seen in the changes of the bonding distances in the geometry optimized structure in Chapter 2. The absence of the third peroxo stretching frequency $\Delta\nu_{V\text{-}O2(sym)}$ in the spectra may be due to significant spectral overlap with other vibrational modes in the region of 500 cm^{-1} to 700 cm^{-1} region and a potentially weak intensity as this mode is highly coupled to vibrations of the ligand set. The observed vibrational bands and their assignments are consistent with what has been previously observed for a variety of oxo-peroxovanadium(V) complexes.

Dissolution of K[VO(O_2)Hheida] into acetonitrile results in 3 cm^{-1} to 9 cm^{-1} shifts in the assigned vanadium related vibrational modes. The V=O vibrational band shifts to lower energy while the O-O stretch shifts to higher energy, this is consistent with removal of the closely associated potassium ion in the solid state. The spectral range of the ZnSe crystal in the FTIR-ATR measurements prevented data collection below 700 cm^{-1}. It is important to note that the use of acetonitrile-d_3 was necessary to shift the vibrational bands associated with the

solvent out of the spectral range for the $\nu_{V=O}$ and ν_{O-O} vibrational bands. As was the case for the solid state measurements, substitution of ^{18}O-^{18}O generate the appropriate shift in the ν_{O-O} vibrational band of -50 cm^{-1} where the reduced mass approximation predicts -53 cm^{-1}. In contrast to the oxo and peroxo vibrational bands, the $\nu_{C=O}$ stretch shows a dramatic shift of +31 cm^{-1}. This shift indicates that in solution the C=O must have a higher force constant which correlates with a strong coordination bond of the carboxylate to vanadium. The potassium ion in the crystal structure of K[$VO(O_2)$Hheida] appears to be most closely associated with the uncoordinated carboxylate oxygen and the ionic interaction likely reduces the strength of the coordination bond to vanadium, consequently lowering the energy of this vibration.

As K[$VO(O_2)$Hheida] is C_1 symmetric, all vibrational modes are both IR and Raman active. The use of resonance raman spectroscopy provides a potentially useful tool to enhance those vibrations associated with the peroxo to vanadium charge transfer band. Unfortunately, due to the low molar absorptivity of the LMCT transition no significant resonance enhancement in either solution or solid state measurements was observed. The raman spectra of natural abundance and ^{18}O labeled peroxide confirmed the spectral assignments made using FTIR. As was the case for FTIR, the vibrational band associated with a symmetric stretch of the vanadium peroxide bond, $\Delta\nu_{V\text{-}O2(sym)}$, was not observed. The solid state raman measurements provide a better resolution of the peroxo and oxo stretching frequencies, in particular the composite vibrational modes observed overlapping the $\Delta\nu_{V\text{-}O2(asym)}$ were significantly lower intensity than the FTIR measurements. Dissolution of K[$VO(O_2)$Hheida] in acetonitrile-d_3 dramatically reduces the intensity of the observed vibrational bands. In particular the $\Delta\nu_{V\text{-}O2(asym)}$ is no longer a cleanly resolved vibrational transition. This is likely the result of lattice enhancements of the vibrational modes in the solids state. Further complications to the solution measurements involved the effective background substraction of the acetonitrile vibrational bands which dominated the spectrum at the saturated concentrations of 11.49 mM [V] employed in these

studies. Nonetheless, the observed vibrational bands are consistent with those observed for the FTIR-ATR measurements in dilute solutions (2.5 mM [V]).

Effects of protonation on the vibrational spectrum of [VO(O$_2$)Hheida]$^-$

The above sections have determined the changes expect for protonation of an uncoordinated carboxylate donor and assigned the vibrational bands for K[VO(O$_2$)Hheida] in both solution and the solid state. The protonated form of [VO(O$_2$)Hheida]$^-$ is significantly less soluble in acetonitrile than the corresponding potassium salt. The reduced solubility was exploited to isolate H[VO(O$_2$)Hheida] at low temperatures from acetonitrile solutions. The resulting red-orange solid is extremely hygroscopic and quickly decomposes unless kept in an anhydrous environment. The identity of H[VO(O$_2$)Hheida] was confirmed by the presence a single broad ^{51}V NMR resonance at -518 ppm.

Calculated vibrational modes for a hydroperoxo species show significant shifts in the peroxo and oxo transitions. The calculated frequencies for $\nu_{V=O}$, $\nu_{V\text{-}O2(asym)}$, and $\nu_{O\text{-}O}$ are 1008 cm^{-1}, 887 cm^{-1}, and 595 cm^{-1}, respectively (Figure 3.19). The composite vibrational mode $\nu_{V\text{-}O2(sym)}$ is not present in the hydroperoxo species, instead a composite ligand vibration and a O-H bend of the hydroperoxo proton appears at 689 cm^{-1}. It is important to note that these calculated vibrational modes do not take into account solvation or hydrogen bonding effects which can reduce the magnitude of the change in the vibrational mode. Therefore, the calculated frequencies should be treated as an upper limit to the amount of change expected. Solid state measurements of H[VO(O$_2$)Hheida] do not show these magnitude shifts. The $\nu_{V=O}$, $\nu_{V\text{-}O2(asym)}$, and $\nu_{O\text{-}O}$ vibrations shift by -9 cm^{-1}, 3 cm^{-1} and 3 cm^{-1} respectively. The carboxylate stretching frequency shifts by only -5 cm^{-1}. The shift in the carboxylate stretch does not reproduce the dramatic change in intensity and the appearance of two carboxylate related stretching frequencies observed for H[VO(O$_2$)bpg]$_2$Tf. These results definitively rule out the possibility of a fully protonated carboxylate moiety contributing significantly to the reactivity of [VO(O$_2$)Hheida]$^-$.

A new vibrational band appears at 704 cm^{-1} which may be indicative of the composite vibrational mode with an O-O-H bending component observed in the calculated vibrational frequencies. This new vibrational mode is not affected by isotopic labeling of peroxide nor does it shift when deuterium is substituted for a proton. The lack of isotopic shifts prevents any definitive assignment of this new vibrational mode.

Dilute solution FTIR-ATR measurements of H[$VO(O_2)$Hheida] show identical peroxo and oxo vibrational bands to the solid state measurements, however a significant broadening of the carboxylate band occurs in solution. The triflate anion present in solution measurements has a vibrational transition at 1604 cm^{-1}, the broadening of the carboxylate band in solution is most likely due to overlap with the triflate vibrational band. The strong correlation of the peroxo and oxo stretching frequencies between solution and solid state indicate that the dilutent used in the solid state measurements, KBr, does not affect the protonation states. The observed vibrational shifts of the peroxo and oxo donors for H[$VO(O_2)$Hheida] are identical to those observed for dilute solutions of K[$VO(O_2)$Hheida]. This is consistent with formation of a variety of species protonated species in which the magnitude and intensity of the vibrational modes is reduced due to hydrogen bonding intereactions. Additionally, the O-H stretching region of H[$VO(O_2)$Hheida] contains a very broad vibrational band spanning over 1000 cm^{-1} as would be expected for a weak H-bonding interaction.

Understanding the reactivity of Oxo-peroxovanadium complexes

The calculated energies for seven protonated forms of $[VO(O_2)Hheida]^-$ were presented in Chapter 2. The protonated forms consist of four different possible protonation locations corresponding to the peroxo moiety, one on the oxo, and two possibilities for protonation of each of a single carboxylate's oxygens. Using the relative energy differences presented in Chapter 2, a Boltzmann distribution at 298 K was calculated (Table 3.5). It is important to note that protonated carboxylate oxygens were only

Table 3.5: Boltzmann distribution of potential protonation sites based on calculated energies at 298K

Protonation Site	ΔE_{scf} (kcal/mol)	Degeneracy	$e^{(-Ei/kT)}$	N_i/N
$H_{(up)}$-O-O	0	1	1	0.598
$H_{(down)}$-O-O	0.619	1	0.351	0.210
O-O-$H_{(up)}$	1.336	1	0.104	0.0626
Uncoord. COOH	1.353	2	0.203	0.121
V-OH	2.937	1	0.00702	0.00420
O-O-$H_{(down)}$	3.105	1	0.00528	0.00316
Coord. COOH	6.608	2	2.85×10^{-5}	1.70×10^{-5}

calculated for one of the carboxylate donors in $Hheida^{2-}$. As the energy difference between protonation of either of the two carboxylates should be negligible, these species were treated as doubly degenerate in the calculation of the Boltzmann distribution. Based on the calculated energy differences at 298 K a mixture of protonated species should be present. As would be expected the three lowest energy protonation states were hydroperoxo species differing in the orientation of the proton with respect to the V=O. The hydroperoxo forms account for 87% of the vanadium species present. The next dominant species is protonation of the uncoordinated carboxylate oxygen which accounts for another 12% of the total population. As the gas phase calculations do not account for solvation effects or hydrogen bonding the energy differences between protonated species are likely overestimated. In Chapter 2 the estimated error in the calculated energies is 2 kcal/mol. While the trends are still accurate, the actual difference in energy is likely to much smaller than the calculations predict, consequently, the hydroperoxo species is less populated while the other protonated species are increased in population. As the intensity of the vibrational transition is proportional to the concentration of that species, the intensity of the vibrational bands for any one species would be to low to detect.

Interestingly, the lower detection limit estimated for the XAS measurements was 20% protonation of the V=O bond. The lack of change in the pre-edge area is consistent with the Boltzmann distribution, in which only 0.4% of a $VOH(O_2)Hheida$ should exists. The distribution of protonated species is also consistent with the observed vibrational changes. A single protonated species

would have caused a significant perturbation of the observed vibrational bands, which was not observed. The population distribution indicates that multiple protonated species exist at the temperature our measurements were collected at. The timescale of vibrational spectroscopy is significantly faster than the diffusion limit, in which case exchange effects on the spectra can be ruled out. The presence of multiple protonated species all having slightly different vibrational frequencies dramatically reduces the intensity of any one vibrational band. Additionally, the magnitude of the shift in the vibrational bands upon protonation of any donor can be dramatically affected by solvation and more importantly H-bonding. Therefore the small perturbations observed in the vibrational bands are consistent with a variety of protonated species existing simultaneously as predicted by the Boltzmann distribution.

The results provide new insight into the mechanism for substrate oxidation with $[VO(O_2)Hheida]^-$, previous proposals have suggested protonation of the peroxo moiety activates the ground state complex for oxidation. Previous work has shown that a small perturbation of the peroxo-vanadium charge transfer band and the ^{51}V NMR resonance occur upon protonation. Considering in totality that a proton interacts with the vanadium complex, the spectroscopic studies presented in this chapter and the energetics presented in Chapter 2, we can now shed new light on the mechanism of oxidation. A more accurate description of the system involves a variety of protonated species in solution; however, only one species, the hydroperoxide, is activated. The activation of the complex occurs in the transition state as opposed to forming a single low energy intermediate. This correlates well with the observed reactivity for $VO(O_2)$bpg and $VO(O_2)$Hheida. The bpg complex has been shown to be the least catalytically active for bromide oxidation and is inactive with respect to sulfide oxidation. The crystallographically characterized protonated carboxylate dimer of $VO(O_2)$bpg, suggests that protonation of the carboxylate donor is the most energetically favored protonation state. The reduce activity of $VO(O_2)$bpg can be partially explained by the competitive protonation of the carboxylate reducing the amount of catalytically activated hydroperoxo species. $[VO(O_2)Hheida]^-$ on the other

hand is an extremely efficient bromide and sulfide oxidation catalyst. The lack of carboxylate protonation as observed by the vibrational studies is consistent with reduced basicity of a carboxylate donor *cis* to the V=O bond when compared to a *trans* carboxylate as is the case for $VO(O_2)$bpg. The lack of carboxylate protonation increases the population of protonated hydroperoxo species thereby enhancing the reactivity of the complex.

Conclusion

The spectroscopic investigation contained herein show that a discrete protonated intermediate is not present upon addition of a proton to the VHPO functional model $K[VO(O_2)Hheida]$. The X-ray absorption studies indicate that greater than 20% of a protonated oxo species does not exist under catalytic conditions. The vibrational spectroscopies for complexes in both the solution and solid state are inconsistent with the formation of a single protonated intermediate. The proton appears to be weakly bonded to multiple sites of the vanadium complex as is evident by the small shifts in the vibrational frequencies and the broadening of the linewidth. The apparent pKa of $H[VO(O_2)Hheida]$ in acetonitrile is 6.0 (HBr pK_a = 5.5)[3] and the small energy difference between the protonated isomers as calculated in chapter 2 are both consistent with the proposal that multiple protonated species are present.

The spectroscopic studies presented above provide further support for the role of a basic hydrogen bonding residue in the active of VHPOs directing the protonation of key oxygen ligand to carry out catalysis. Lys353 in the crystal structure of peroxide bound VClPO is positioned to interact with the distal oxygen of the side-on bound peroxo.[18] Computational studies have shown this hydrogen bonding interaction to reduce the barrier to activation for nucleophilic substrate oxidation.[2] Approach of the substrate induces polarization of the peroxo moiety transferring the proton from the lysine residue to the peroxo moiety. Based on the vibrational studies contained in this chapter, $[VO(O_2)Hheida]^-$ may undergo a

similar process with the proton being weakly associated to the vanadium species as opposed to residing on a basic hydrogen bonding functionality.

Hydrogen bonding has also been implicated in the activation of peroxo-titanium(IV) reduced salen complexes, in which a secondary amine forms a hydrogen bond with the coordinated peroxo moiety. Without this hydrogen bond donor, peroxo-titanium(IV) are not catalytically active for nucleophilic substrate oxidation. Another interesting comparison can be drawn with diperoxo-Mo(VI) and W(VI) systems, where computational studies have shown that a proton bridging the equatorial peroxo ligands lowers the barrier to activation for olefin epoxidation.[19] Hydrogen bond donors, whether intermolecular, as is the case for VHPOs,[2,18] and intramolecular, for Ti(IV),[20] Mo(VI),[19] and W(VI)[21] can activate peroxo metal complexes for catalytic oxidations.

The results contained herein provide significant insight into the interaction of protons with perox-metal complexes. These studies have expanded the understanding of the role of protonation in the activation of K[VO(O_2)Hheida] for substrate oxidation and reinforces the proposed role of the hydrogen bond donors in VHPOs. Additionally, this work provides the basis for developing new ligand sets for peroxo-metal catalysts that either hydrogen bond with the peroxo moiety or differentiate the pKa's of the donor sets to reduce the number of competitive protonation.

References

1. Matsumoto, K.; Sawada, Y.; Katsuki, T. *Synlett* **2006**, 3545-3547.

2. Zampella, G.; Fantucci, P.; Pecoraro, V. L.; De Gioia, L. *J. Am. Chem. Soc.* **2005**, *127*, 953-960.

3. Colpas, G. J.; Hamstra, B. J.; Kampf, J. W.; Pecoraro, V. L. *J. Am. Chem. Soc.* **1996**, *118*, 3469-3478.

4. Hamstra, B. J.; Colpas, G. J.; Pecoraro, V. L. *Inorg. Chem.* **1998**, *37*, 949-955.

5. Smith, T. S.; Pecoraro, V. L. *Inorg. Chem.* **2002**, *41*, 6754-6760.

6. Schneider, C. J.; Zampella, G.; Greco, C.; Pecoraro, V. L.; De Gioia, L. *Eur. J. Inorg. Chem.* **2007**, 515-523.

7. Weng, T.-C.; Hsieh, W.-Y.; Uffelman, E. S.; Gordon-Wylie, S. W.; Collins, T. J.; Pecoraro, V. L.; Penner-Hahn, J. E. *J. Am. Chem. Soc.* **2004**, *126*, 8070-8071.

8. Penner-Hahn, J. E.; Benfatto, M.; Hedman, B.; Takahashi, T.; Doniach, S.; Groves, J. T.; Hodgson, K. O. *Inorg. Chem.* **1986**, *25*, 2255-2259.

9. Weidemann, C.; Rehder, D.; Kuetgens, U.; Hormes, J.; Vilter, H. *Chem. Phys.* **1989**, *136*, 405-412.

10. Sitter, A. J.; Terner, J. *J. Labelled Compd. Radiopharm.* **1985**, *22*, 461-465.

11. Bonadies, J. A.; Carrano, C. J. *J. Am. Chem. Soc.* **1986**, *108*, 4088-4095.

12. Bonadies, J. A.; Butler, W. M.; Pecoraro, V. L.; Carrano, C. J. *Inorg. Chem.* **1987**, *26*, 1218-1222.

13. Hamstra, B. J.; Houseman, A. L. P.; Colpas, G. J.; Kampf, J. W.; LoBrutto, R.; Frasch, W. D.; Pecoraro, V. L. *Inorg. Chem.* **1997**, *36*, 4866-4874.

14. Colpas, G. J.; Hamstra, B. J.; Kampf, J. W.; Pecoraro, V. L. *J. Am. Chem. Soc.* **1994**, *116*, 3627-3628.

15. Weng, T. C.; Waldo, G. S.; Penner-Hahn, J. E. *Journal of Synchrotron Radiation* **2005**, *12*, 506-510.

16. Yano, J.; Robblee, J.; Pushkar, Y.; Marcus, M. A.; Bendix, J.; Workman, J. M.; Collins, T. J.; Solomon, E. I.; George, S. D.; Yachandra, V. K. *J. Am. Chem. Soc.* **2007**, *129*, 12989-13000.

17. Butler, A.; Clague, M. J.; Meister, G. E. *Chem. Rev.* **1994**, *94*, 625-638.

18. Messerschmidt, A.; Prade, L.; Wever, R. *ACS Symp. Ser.* **1998**, *711*, 186-201.

19. Gisdakis, P.; Yudanov, I. V.; Roesch, N. *Inorg. Chem.* **2001**, *40*, 3755-3765.

20. Yudanov, I. V.; Gisdakis, P.; Di Valentin, C.; Rosch, N. *Eur. J. Inorg. Chem.* **1999**, 2135-2145.

21. Di Valentin, C.; Gisdakis, P.; Yudanov, I. V.; Roesch, N. *J. Org. Chem.* **2000**, *65*, 2996-3004.

Chapter 4

Rational Design of Asymmetric Sulfoxidation Catalysts

Introduction

Vanadium coordination complexes are effective sulfoxidation catalysts and attempts to develop asymmetric catalysts have yielded a variety of promising results. Vanadium Schiff-base complexes, originally developed by Nakajima and co-workers in 1986,[1] are effective asymmetric sulfoxidation catalysts. These systems were later optimized by Bolm and co-workers as *in situ* derived catalysts.[2] Typical conditions involve a chiral Schiff base derived from an amino alcohol and salicylaldehyde, the most effective of which is the Schiff base generated from *tert*-leucinol and 3,5-di-*tert*-butylsalicylaldehyde with $VO(iPrO)_3$. The catalytic vanadium species is generated *in situ* in a biphasic system ($CHCl_3/H_2O$) employing hydrogen peroxide as the terminal oxidant. The Bolm-type systems are capable of generating a near quantitative yield of alkyl aryl sulfoxides from thioether starting materials. Under optimized conditions, enantiomeric excesses can reach as high as 85%.[2] In the case of disulfide starting materials, the Bolm system can provide chiral sulfoxide products with a 97% ee.[3] Functional models for vanadium-dependent haloperoxidases have also been employed as asymmetric sulfoxidation catalysts. In contrast, chiral amino-alcohols complexes of oxovanadium(V) have been shown to only achieve <37% enantioselectivity with the use of cumyl hydroperoxide as the terminal oxidant. Many factors control the stereoselectivity of a reaction; in particular, the geometric constraints imposed upon the transition state can impart a preferential approach of the substrate or differentiate the barriers to activation.

Modern computational methods can provide additional insight into the factors controlling the reactivity of transition metal catalysts. In particular, the geometric constraints of the transition state allow for the design of ligands to limit the number of stereochemical outcomes for a reaction. The studies presented in this chapter are focused on the rational design of an asymmetric catalyst based on the transition geometries calculated for the achiral sulfoxidation catalyst, K,VO(O_2)Hheida][4] in Chapter 2. This work provides insight into the factors that control the stereoselectivity of sulfoxidation by tripodal amine vanadium complexes through reactivity and spectroscopy.

Experimental Methods

CAUTION: Metal peroxo complexes can be explosive. Although no complexes explored have behaved as if they are explosive, care should be taken to minimize the amount of complex generated, maintain low temperatures, and test for shock sensitivity. Acetonitrile and dichloromethane were degassed and passed through an alumina column prior to use. Methanol and ethanol were distilled prior to use. All other reagents were purchased from Sigma-Aldrich as reagent grade or better and used as recieved.

N,N-diacetate-(1S,2R-norephedrine), diethylester (1): (1S,2R) Norephedrine (33 mmol) and Na_2CO_3 (69 mmol) were added to 250 mL of degassed acetonitrile$_{dry}$. Bromoethyl acetate (69 mmol) was added as an acetonitrile solution dropwise over 1 hour. The resulting suspension was stirred at room temperature for 18 hours. After cooling to room temperature, the suspension was vacuum filtered and filtrate was concentrated *in vacuo*. The resulting colorless oil was purified via flash column chromatography using silica gel and 4:1 pentane/ethylacetate. The resulting colorless oil will crystallize if thoroughly dried *in vacuo*. Yield: 8.11 g (76%) ^{1}H NMR ($CDCl_3$): 7.27(m), 4.73(d), 4.13(q), 3.52(q, ^{2}J=17 Hz), 3.13(q of d), 1.21(t), 0.80(d). ^{13}C NMR ($CDCl_3$): 173.0, 141.4,

128.1, 126.9, 126.0, 73.9, 63.6, 61.0, 53.9, 14.3, 11.1. ESI^+-MS: 362.0 (100%), 324.1.

N,N-diacetate-(1S,2R-norephedrine), dipotassium salt (2): 1 (10 mmol) was added to 25 mL distilled methanol. Potassium hydroxide (20.1 mmol) was added to the methanolic solution and stirred for 2 hours at room temperature. The solution was cooled to 0 °C and triturated with diethyl ether. The resulting white solid was vaccum filtered and rinsed with diethyl ether. The potassium salt can be recrystallized from ethanol and diethyl ether. Yield: 3.33 g (97%) ^{1}H NMR (CD_3OD): 7.30 (d), 7.24 (d), 7.14 (t), 3.93(d), 3.24(d), 3.10(q of d), 0.86(t). ESI^- /MS *m/z*: 362.0 (100%), 324.1. ^{13}C NMR (CD_3OD): 180.61, 144.55, 128.89, 127.66, 127.38, 75.31, 63.85, 57.92, and 10.15. FTIR: 3363 (b) cm^{-1}, 1587 cm^{-1} (s) 1557 cm^{-1} (s), 1401 (s) cm^{-1}, 761 (s) cm^{-1}, 740 (s) cm^{-1}, 708 (s) cm^{-1}, 629 (s) cm^{-1}, 554 (s) cm^{-1}.

N-[(*1R*)1-phenyl-2-hydroxyethyl iminodiacetate), dipotassium salt (4): (*1S*)-2-amino-1-phenylethanol (9.8mmol) was added to 125 mL $acetonitrile_{dry}$ with bromoethylacetate (19.7 mmol) and Na_2CO_3 (20 mmol). The slurry was stirred at 100 °C for 8 hours. The white solids were vacuum filtered and the filtrate was concentrated *in vacuo*. The crude oil was purified via a silica gel column with 80% pentane and 20% ethyl acetate. The 2.33 g of colorless oil was transferred to distilled methanol, where KOH (7.55 mmol) was added to the solution. Two hours of stirring at room temp yielded a white opaque slurry. The white solid was washed with cold isopropanol/diethyl ether and dried invacuo. Yield: 2.35 g (72%) ^{1}H NMR (CD_3OD): 7.36 (d), 7.31 (d), 7.22 (t), 4.81 (dd, J=2.07 Hz, 10.40 Hz), 3.66(d, J^2=16.05), 3.108(d, J^2=16.05), 2.71(dd, J=2.13.18 Hz, 10.65 Hz), 2.57 (dd, J=2.4 Hz, 13.29 Hz). ^{13}C NMR (CD_3OD): 179.65, 144.87, 129.30, 128.29, 127.16, 72.496, 65.532, 61.34. FTIR: 3302 cm^{-1}, 3086 cm^{-1}, 1724 cm^{-1}, 1619 cm^{-1}, 1352 cm^{-1}, 893 cm^{-1}, 696 cm^{-1}.

N,N-diacetate-(L-alaninol), dipotassium salt (5): Procedure is identical to that of **4**.

(*1S,2S*) 2-amino-1-*t*-butyl-propan-1-ol (6): N,N-dibenzyl 2-amino-1-*t*-butyl-propan-1-ol (7) was synthesized according to literature procedures[5] starting from L-alanine. Hydrogenolysis of **7** (8 mmol) in distilled ethanol with $Pd(OH)_2$ (20% on carbon, wet, 300 mg) was performed in a Parr hydrogenator at 63 psi H_2 for 4 days. The resulting solution was filtered and concentrated, affording **6** as a white solid. Yield: 0.724 g (68%). ^{1}H NMR ($CDCl_3$): 3.19 (q of d), 3.15 (d), 3.08 (d), 0.93 (s). ESI^+/MS *m/z*: 132.3.

N,N-diacetate-((*1S,2S*) 2-amino-1-*t*-butyl-propan-1-ol), diethyl ester (8): **(*1S,2S*) 2-amino-1-*t*-butyl-propan-1-ol** (**6**) (5.7 mmol) was added to a $acetonitrile_{dry}$ suspension of Na_2CO_3 (10 mmol). Bromoethylacetate was added dropwise over 1 hour and heated at reflux for 5 hours. The resulting white suspension was filtered and concentrated to a yellow oil. Silica gel chromatography with an 80:20 mixture of pentane/ethyl acetate resulted in **8** as a colorless oil. Yield: 1.45 g (83%) ^{1}H NMR ($CDCl_3$): 4.27 (q) 3.66 (d), 3.49 (d), 3.40 (d), 3.06 (q of d), 1.27 (t), 1.08 (d), 0.93 (s).

N,N-diacetate-((*1S,2S*) 2-amino-1-*t*-butyl-propan-1-ol), dipotassium salt (9): KOH (5 mmol) was dissolved in distilled methanol and added to **8** (2.5 mmol). The resulting pale yellow solution was stirred for 6 hours. The resulting white suspension was concentrated *in vacuo* and triturated with diethyl ether. Yield: 0.78 g (97%) ^{1}H NMR (CD_3OD): 3.45 (s), 3.25 (d), 3.15 (d), 3.10 (m), 1.07 (d), 0.93 (s). ^{13}C NMR (CD_3OD): 180.12, 78.45, 57.08, 56.54, 36.22, 27.2, 12.5. ESI^+/MS *m/z*: 324.1 (100%), 362.0 (11%). ESI^-/MS *m/z*: 246.2 (100%), 284.2 (75%) FTIR: 3373 cm^{-1} (b), 2955 cm^{-1} (s), 1588 cm^{-1} (b), 1401 cm^{-1} (s), 990 cm^{-1} (s), 718 cm^{-1} (s).

VO(Hnorida) (8): Vanadyl sulfate (1 mmol) was dissolved in 20 mL of degassed H_2O under N_2 resulting in a deep blue solution. Addition of **2** (1 mmol) while purging with N_2 immediately precipitates a pale blue solid. The slurry was stirred for 2 hours under N_2 and vacuum filtered. The resulting blue solid was rinsed with degassed H_2O and dried *in vacuo*. Yield: 0.255 g (77%) ESI^-/MS *m/z*: 330.9 (100%), 331.9 (8%), 662.8 (30%), 663.9 (3%). FTIR: 3132 (b) cm^{-1}, 2386 (b) cm^{-1}, 1890 (b) cm^{-1}, 1580 (s) cm^{-1}, 1392 (s) cm^{-1}, 972 (s) cm^{-1}, 806 (w) cm^{-1}, 742 (w) cm^{-1}, 698 (w) cm^{-1}, 650 (w) cm^{-1}, 630 (w) cm^{-1}.

K[VO(O_2)Hnorida] (9): V_2O_5 (0.5 mmol, 0.0908 g) was added to 5 mL of H_2O and the resulting yellow slurry cooled to 0 C. H_2O_2 ($50\%_{(aq)}$, 2 mL) was added dropwise to the yellow slurry in a darkened room. The orange-red slurry was stirred for 3 hours at 0 °C in a darkened room affording a dark red solution pH ≈ 2. **2** (1.0 mmol, 0.344 g) was added in 6 equivalent portions allowing each addition of ligand to completely solubilize. The red solution was allowed to stir for 4 hours at 0 °C and then stored 4 °C overnight. Distilled ethanol (50 mL) was added and allowed to stand at 4 °C for 6 hours. The yellow-orange precipitate was filtered and the filtrate was added dropwise over 15 minutes to a vigorously stirring diethyl ether (100 mL) at 0 °C. The resulting orange-red slurry was allowed to stand for 8 hours at -20 C after which the supernate was decanted off affording a hygroscopic red oil. Trituration with diethyl ether yields the vanadium complex as it's potassium salt. The compound can be recrystalized from distilled methanol and ether solutions. X-ray diffraction quality crystal can be obtained from slow solvent evaporation of a 1:1:1 mixture of water, ethanol, and isopropanol at room temperature in an NMR tube. Yield: 0.133 g (33%). ESI^-/MS: 364.4 (100%), 266.3 (23%) FTIR: 3426 (b) cm^{-1}, 1622 (b) cm^{-1}, 1388 (s) cm^{-1}, 954 (s) cm^{-1}, 926 (w) cm^{-1}, 870 (s) cm^{-1}, 630 (s) cm^{-1}, 562 (s) cm^{-1}.

VO(Hpheida): The complexation reaction is identical to that of **8**. X-ray diffraction quality crystals were obtained from water/diethyl ether diffusion at 4 °C.

K[VO(O_2)Halida] (10): V_2O_2 (2.5 mmol) was suspended in 5 mL H_2O and cooled to 0 °C. H_2O_2 (50%$_{(aq)}$, 1 mL) was added to the cold suspension and stirred for 3 hours in a darkened room. **5** was added as a solid to the red solution and the pH was adjusted to 3.72 with triflic acid. The resulting red solution was stored overnight at 0 °C. Ethanol was added twice in 60 mL portions and the solution was stored for 12 hours at 0 C affording a red oil. Triturating the oil with diethyl ether yields a red orange solid. Yield: 0.868 (53%) ESI$^-$/MS *m/z*: 288.5 (100%) 289.4 (6.5%). FTIR: 3437 (b) cm^{-1}, 1642 (b) cm^{-1}, 1384 (s) cm^{-1}, 952 (s) cm^{-1}, 926 (s) cm^{-1}, 779 (s) cm^{-1}, 640 (s) cm^{-1}, 566 (s) cm^{-1}.

Kinetics Studies

All kinetics studies were performed on an Ocean Optics SD2000 fiber optic spectrophotometer with a 1 cm quartz cuvette. THe UV-Vis spectrum (220 nm – 500 nm) was collected every 0.1 s after initiation of the reaction with triflic acid. Solid samples no older than 4 days were used to prepare stock solutions, and metal containing stock solutions were kept no longer than 2 hours to minimize complex degradation. Hydrogen peroxide solutions were titrated potassium permanganate. Triflic acid solutions were titrated with standardized sodium hydroxide. The order of addition for all kinetic experiments is [V], [H_2O_2], [Substrate], followed by [HTf]. The background absorbance at 290 nm from [V] was subtracted prior to the addition of substrate.

Determination of enantiomeric excess for thioether oxidation

Typical reaction conditions employed K[VO(O_2)Hnorida] solubilized in the appropriate solvent with 18-C-6, 100 mM peroxide, 100 mM *p*-tolyl methyl sulfide, and one equivalent of triflic acid. Reaction progress was monitored by TLC and quenched upon complete consumption of thioanisole with saturated $NaHCO_3$. Each reaction was extracted with dichloromethane and concentrated. ^{1}H NMR was used to determine the ratio of thioether/sulfoxide/sulfone by integrating the

aromatic region of the spectrum. The crude product mixture was purified on a silica gel pipet column (75 pentane:25 ethyl acetate) to remove traces of the catalysts and unreacted thioether.

The enantiomeric excess of *p*-tolyl methyl sulfoxide was determined using a Chiracel OB analytical normal phase column on a HP600 instrument by HPLC analysis with 50/50 Hexane to 2-propanol mobile phase at a flow rate of 0.5 mL/min. The *S*-enantiomer of *p*-tolyl methyl sulfoxide elutes at 10.2 min and the *R*-enantiomer at 16.9 min. Absolute configuration assignments were made by comparison to the commercially available enantiopure sulfoxide. The absorbance of p-tolyl methyl sulfoxide was monitored at 260 nm and the resulting chromatogram was integrated to obtain the peak areas.

Collection and Refinement of X-Ray Data

Suitable crystals of K[$VO(O_2)$Hnorida] (Figure 4.1) and $VO(O_2)$pheida (Figure 4.2) were obtained by the methods described above. Crystals were mounted on a standard Bruker SMART APEX CCD-based X-ray diffractometer equipped with a low-temperature device and normal- focus Mo-target X-ray tube (λ = 0.71073 Å) operated at 2000 W power (50 kV, 40 m Å). The structures were solved and refined using a full-matrix least-squares refinement by Jeff W. Kampf, staff crystallographer in the University of Michigan Chemistry Department. All non-hydrogen atoms were refined anisotropically with hydrogen atoms placed in idealized positions. All calculations were performed with the SHELXTL (version 6.12) software package, Additional information on the data collection and refinement are reported in Table 4.1.

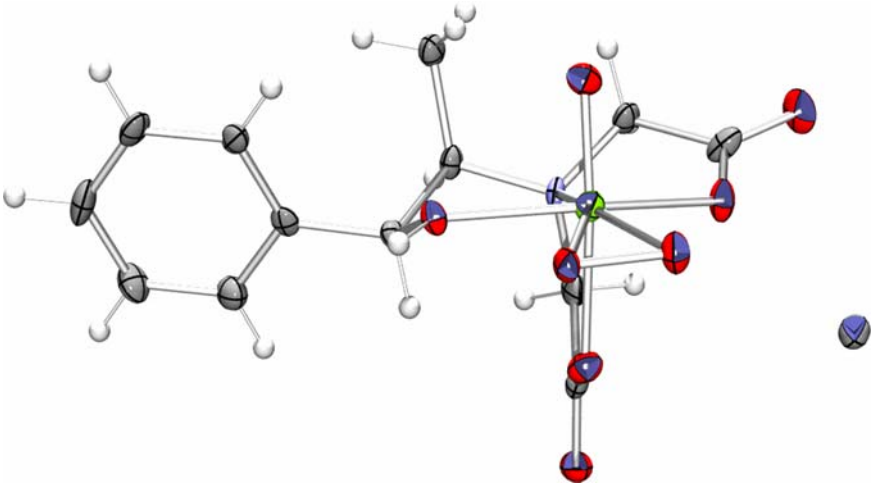

Figure 4.1: ORTEP diagram at 50% probability for K[VO(O_2)Hnorida]•2H_2O. Grey = Carbon, Red = Oxygen, Light Blue = Nitrogen, Grey w/ blue cutout = Potassium.

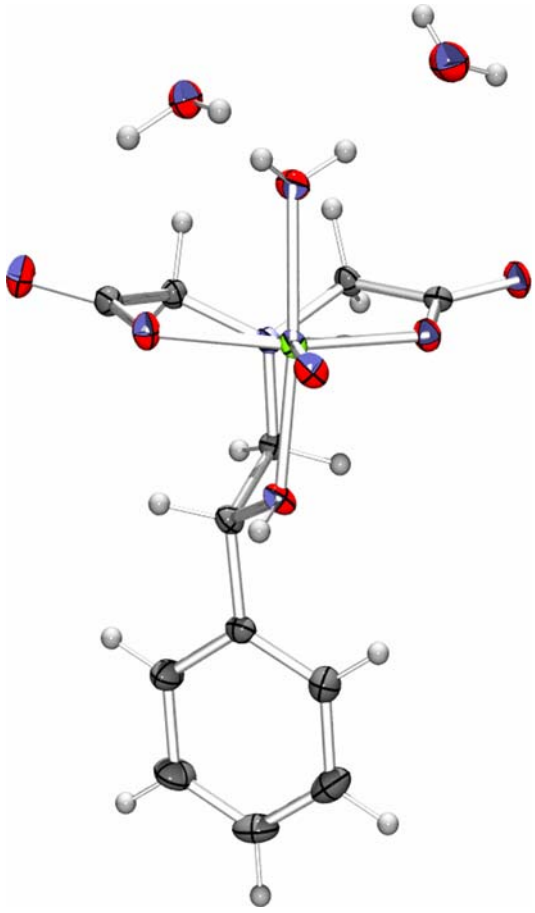

Figure 4.2: ORTEP diagram at 50% probability for VOHpheida•3H_2O. Grey = Carbon, Red = Oxygen, Light Blue = Nitrogen.

Table 4.1: Structure Determination Summary

Compound	K[VO(O_2)Hnorida]	VOHpheida
Empirical formula	$C_{26}H_{31}K_2N_2O_{18}V_2$	$C_{12}H_{19}NO_9V$
Formula weight	839.61	372.22
Crystal Description	Orange needles	Blue needles
Crystal system, space group	Monoclinic	Monoclinic
Space Group	P2(1)	PS(1)
Z	2	2
a (Å)	7.5783 (7)	7.0013 (12)
b (Å)	27.774 (3)	6.8124 (12)
c (Å)	7.9128 (7)	16.890 (3)
α (deg)	90	90
β (deg)	98.845	99.171 (3)
γ (deg)	90	90
Volume ($Å^3$)	1645.7(3)	795.3 (2)
Temperature (K)	123(2)	150(2) K
Data / restraints / parameters	5622 / 1 / 466	3803 / 1 / 236
Wavelength (Å)	0.71073	0.71073
Absorption coefficient (mm^{-1})	0.905	0.669
R	0.0470	0.0217
wR^2	0.0843	0.0587
Goodness-of-fit on F^2	1.014	1.060

Other Instrumentation

Electrospray mass spectrometry was performed on a Micromass LCT Time-of-Flight mass spectrometer with Electrospray and APCI. Elemental analysis was performed by the University of Michigan Microanalysis Laboratory. ^{51}V NMR was carried out on a Varian MR400 400 MHz spectrophotometer with a Varian 5mm PFG AutoX Dual Broadband probe. ^{1}H and ^{13}C NMR were collected on a Varian Inova500 500 MHz spectrophotometer.

Results

Comments on Synthesis

Vanadium complexes bearing benzylic alcohols in these studies are susceptible to ligand oxidation. In fact, vanadium pentoxide has been employed as a mild selective oxidant for secondary alcohols in the presence of dioxygen.[6]

Due to this possible side reactivity it is important to maintain anaerobic conditions when manipulating the oxovanadium(IV) complexes in solution. Once isolated as dry solids the vanadium(IV) complexes can be stored for several weeks at -40 °C under an inert atmosphere. Solution samples of VO(Hnorida) and VO(Hpheida) are rapidly oxidized when exposed to oxygen or hydrogen peroxide. The possible generation of hydroxyl radicals from the one electron oxidation of vanadium(IV) by hydrogen peroxide complicates the use of these precursors for reactivity studies due to the potential oxidation of the ligand set.

In the case of peroxo-oxovanadium(V) complexes, care must be taken to minimize the counterion concentrations during complexation to avoid co-precipitation of salts. Oxo-peroxovanadium(V) complexes are generally stable in aqueous solution at a pH = 2 – 4. Therefore, when utilizing the dipotassium ligand salts it is necessary to generate an acidic peroxovanadate solution to minimize the addition of acid necessary to achieve the optimal stable pH range for these complexes. This can be accomplished by reacting V_2O_5 with excess hydrogen peroxide. Aqueous speciation studies have shown that at pH < 2 the dominant species is a monoperoxo-oxovanadium(V) complex, whereas in mildly acidic conditions (2 < pH < 6), the diperoxo-oxovanadium(V) species dominates.[7] Additionally, vanadium(V) solutions can assist in the photocatalyzed disproportionation of hydrogen peroxide, which is an extremely exothermic process.[7] By lowering the temperature of the reaction and minimizing the amount of extraneous light, the disproportionation reaction can be avoided.

The details of the asymmetric ligand, K_2Hnorida, presented above will be explored in detail in the discussion section later in this chapter. K[VO(O_2)Hnorida] is stable for several weeks at -40 °C, but at room temperature the complex decomposes to a complex mixture of vanadium(IV) species. ESI^- /MS and ^{1}H NMR that suggest the oxidation of the benzylic alcohol of the ligand becomes oxidized to the corresponding ketone. All solid samples employed for kinetic or catalytic studies were stored no longer than 4 days prior to data collection. Stock solution samples were prepared immediately prior to data collection and discarded within 2 hours of preparation.

The studies presented in this chapter focus on understanding the reactivity of K[VO(O_2)Hnorida]. These studies highlight the potential of the class of peroxo-vanadium catalysts and highlight some challenges associated with the first generation ligand design, in particular the stability of the complex under catalytic conditions. Initial work has begun on the design of a second generation asymmetric ligand set to overcome ligand decomposition issues. Figure 4.3 depicts the synthetic scheme to achieve an asymmetric *t*-butyl substituted ligand. The third synthetic step is a stereoselective organolithium addition[5] and serves as a facile method of obtaining diastereomerically pure protected amino alcohols with a variety of Grignard and organolithium reagents. This work provides the synthetic background necessary for future derivatization of asymmetric tripodal amine vanadium complexes for chiral catalysis.

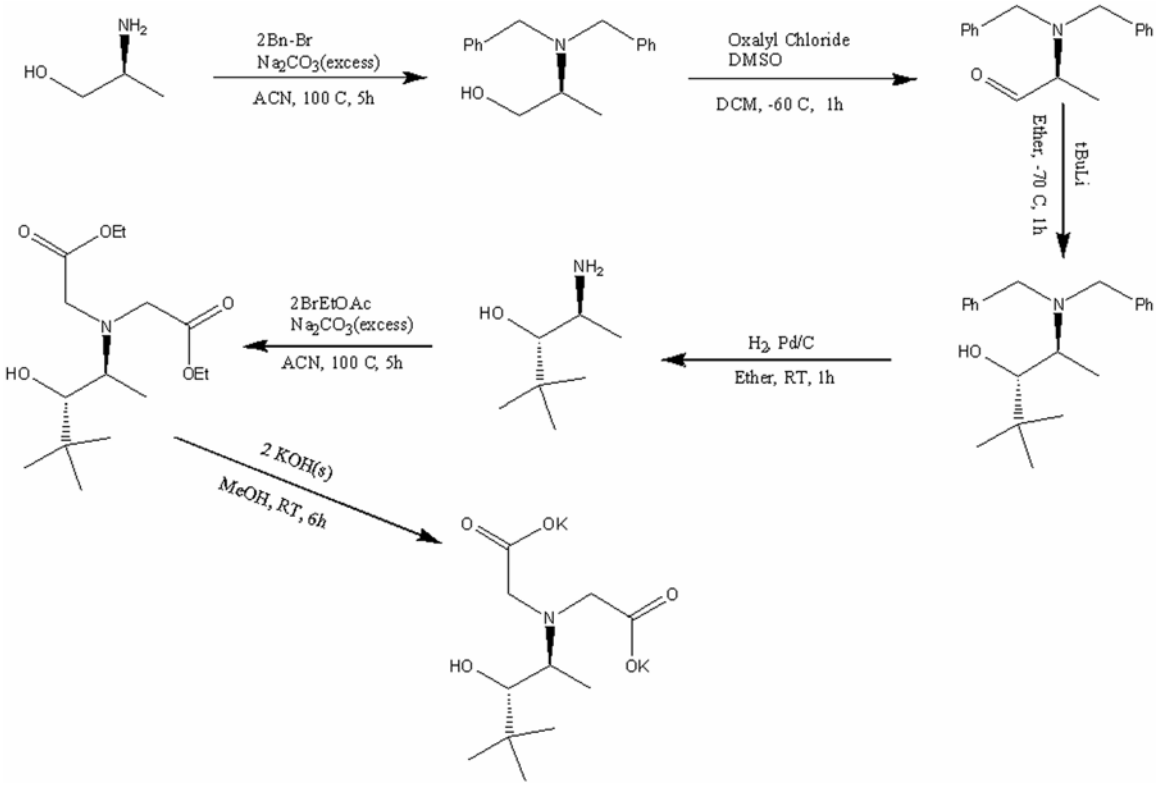

Figure 4.3: Synthetic scheme for the asymmetric synthesis of **9**.

Stereoselectivity of thioether oxidation for K[VO(O_2)Hnorida

The stereoselectivity of thioether oxidation was explored under a variety of conditions (Table 4.2). Vanadium complexes were solubilized using two equivalents of 18-C-6 to chelate the potassium counterion under turnover (excess peroxide with 1 equivalent of triflic acid). The effects of the turnover number, solvent, terminal oxidant and temperature were explored. All reactions carried out with hydrogen peroxide resulted in racemic sulfoxide. Additionally, low enantioselectivities were observed with organic peroxides in acetonitrile. At low temperatures in dichloromethane with organic peroxides a 13% - 19% enrichment of *(R)* – *p*-tolyl methyl sulfoxide was observed.

Solution speciation of K[VO(O_2)Hnorida]

The details of the asymmetric ligand, K_2Hnorida, will be presented in detail in the discussion section later in this chapter. As mentioned above, K[VO(O_2)Hnorida] is not stable for longer than 2 hours and this decomposition process is accelerated in the presence of hydrogen peroxide. In order to solubilize the complex, 18-C-6 is used to chelate the potassium ion, for ^{1}H NMR measurements a pre-saturation of the methylene protons from 18-C-6 was performed. For the ^{1}H-^{1}H COSY spectrum, software suppression of the peak resulting from 18-C-6 was employed in lieu of a presaturation technique.

The x-ray crystal structure of K[VO(O_2)Hnorida] (Figure 4.1) contains the typical side-on bound peroxo donor *cis* to the oxovanadium bond. In contrast to K[VO(O_2)Hheida, the carboxylate donors are not coordinated *trans* to each other in the equatorial plane; instead, the carboxylates are *cis* with one ligand bound *trans* to the V=O bond. Relevant bond distances are presented in Table 4.3. While the solid state structure provides insight into what structures may be possible, the presence of crystal packing forces and potential differential

Table 4.2: Summary of reactivity data for sulfoxidation. %ee = ([S]-[R])/([S]+[R]) * 100%

Catalyst	% Catalyst Loading	Temp (C)	[S]/[SO]/[SO2]	Substrate equivalents (time, h)	*Peroxide*	*H+*	*Solvent*	*%ee*
Hnorida	2.5	25.00	2/94/4	400 (1)	H_2O_2	1 eq.	ACN	0.9%
Hnorida	2.5	25.00	0/52/48	400 (1)	H_2O_2 (1.5X)	1 eq.	ACN	1.6%
Hnorida	2.5	25.00	2/94/4	400 (24)	H_2O_2	---	ACN	2.1%
Halida	2.5	25.00	3/92/4	400 (4)	H_2O_2	1 eq.	ACN	-2.1%
Hheida	2.5	25.00	5/92/3	400 (4)	H_2O_2	1 eq.	ACN	2.7%
Halida	2.5	25.00	10/84/6	400 (4)	tBuOOH	1 eq.	ACN	-0.3%
Hheida	2.5	25.00	3/86/10	400 (4)	tBuOOH	1 eq.	ACN	3.0%
Hnorida	2.5	25.00	0/94/6	400 (4)	tBuOOH	1 eq.	ACN	-2.4%
Hnorida	2.5	25.00	4/93/3	400 (24)	tBuOOH	---	ACN	-3.1%
Hnorida	2.5	25.00	3/89/8	400 (12)	H_2O_2	1 eq.	EtOAc	0.3%
Hnorida	2.5	25.00	69/27/4	400 (12)	H_2O_2	1 eq.	Tol	0.8%
Hnorida	2.5	25.00	4/92/4	400 (12)	H_2O_2	1 eq.	DCM	0.7%
Hnorida	2.5	25.00	0/93/7	400 (4)	tBuOOH	1 eq.	DCM	-11.0%
Hnorida	2.5	25.00	2/86/12	400 (24)	tBuOOH	---	DCM	1.8%
Hnorida	1	25.00	ND	1000 (18)	tBuOOH	---	DCM	0.6%
Hnorida	1	25.00	6/89/5	1000 (3)	tBuOOH	1 eq.	DCM	-7.2%
Hnorida	1	0.00	3/96/1	1000 (15)	tBuOOH	1 eq.	DCM	-13.7%
Hnorida	10	0.00	ND	100 (12)	tBuOOH	1 eq.	DCM	-14.2%
	---	25	46/45/9	1000 (12)	tBuOOH	1 eq.	DCM	0.1%
Hnorida	1	25.00	0/93/7	1000 (36)	CmOOH	1 eq.	DCM	-0.6%
Hnorida	1	0.00	1/91/8	1000(36)	CmOOH	1 eq.	DCM	-19.1%
	---	25	33/51/16	1000 (36)	CmOOH	1 eq.	DCM	0.3%
Hnorida	N/A	25.00	1/97/2	1 (5)	---	1 eq.	DCM	0.3%
Hnorida	N/A	25.00	5/94/1	1 (36)	---	---	DCM	26.3%

solubilities require the consideration of alternative binding modes of the ligand in solution. An alternative coordination mode for K[$VO(O_2)$Hnorida involves the equatorial coordination of both carboxylate oxygen atoms similar to that observed for K[$VO(O_2)$Hheida]. A third possibility is that the weakest donor, the alcohol dissociates from the complex. All three potential coordination modes along with the proton labeling for the ligand are depicted in Figure 4.4.

Table 4.3. Relevant bond distances for peroxo-oxovanadium(V) complexes

	$[VO(O_2)Hheida]^{-1}$	$[VO(O_2)Hnorida]^{-1}$
V=O	1.60	1.60
V-O$_p$	1.87	1.87
V-O$_p$	1.86	1.86
V-OH	2.24	2.08
V-O$_c$	2.04	2.14
V-O$_c$	2.05	2.05
V-N	2.19	2.20
O-O	1.43	1.43

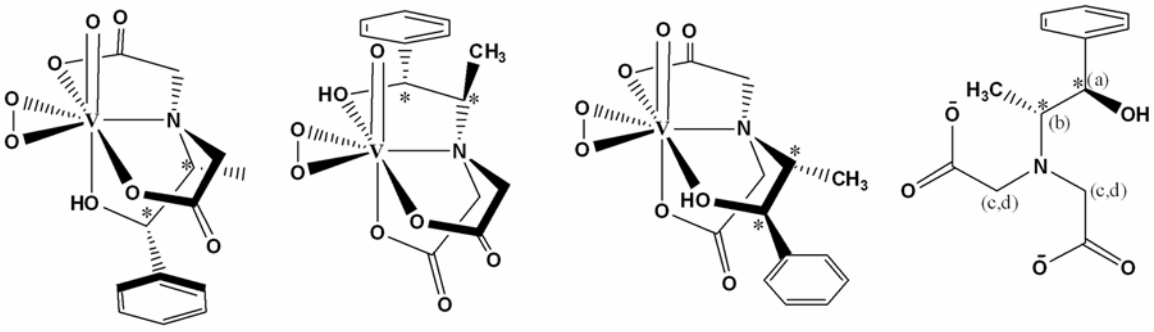

Figure 4.4: Three possible coordination modes for HNorida $^{2-}$ (A,B,C) and the proton assignments for correlation with the NMR spectra (D). Stereocenters are marked with an asterisk.

Freshly prepared solutions in the absence of hydrogen peroxide show one ligand containing species in solution as is evident by ^{1}H NMR (Figure 4.5). The ^{1}H-^{1}H COSY spectrum of K[$VO(O_2)$Hheida] of a freshly prepared solution in acetonitrile is presented in Figure 4.6. The cross peaks of the ^{1}H-^{1}H COSY spectrum correlate with observed coupling constants for the protons on the α-

and β-carbons to the hydroxyl group. Additionally, the methylene protons of the carboxylate show J^2 couplings and are resolved into three doublets, where two methylene protons coincidentally overlap at 3.93 ppm. This confirms that free rotation of the carboxylate donors has been limited and is consistent with coordination of the ligand set to vanadium. ^{51}V NMR shows a single resonance at -520 ppm. These results are in agreement with the negative mode mass spectral analysis of the same solution sample where the dominant *m/z*: 364.3 can be assigned as the $[VO(O_2)Hnorida]^-$ ion.

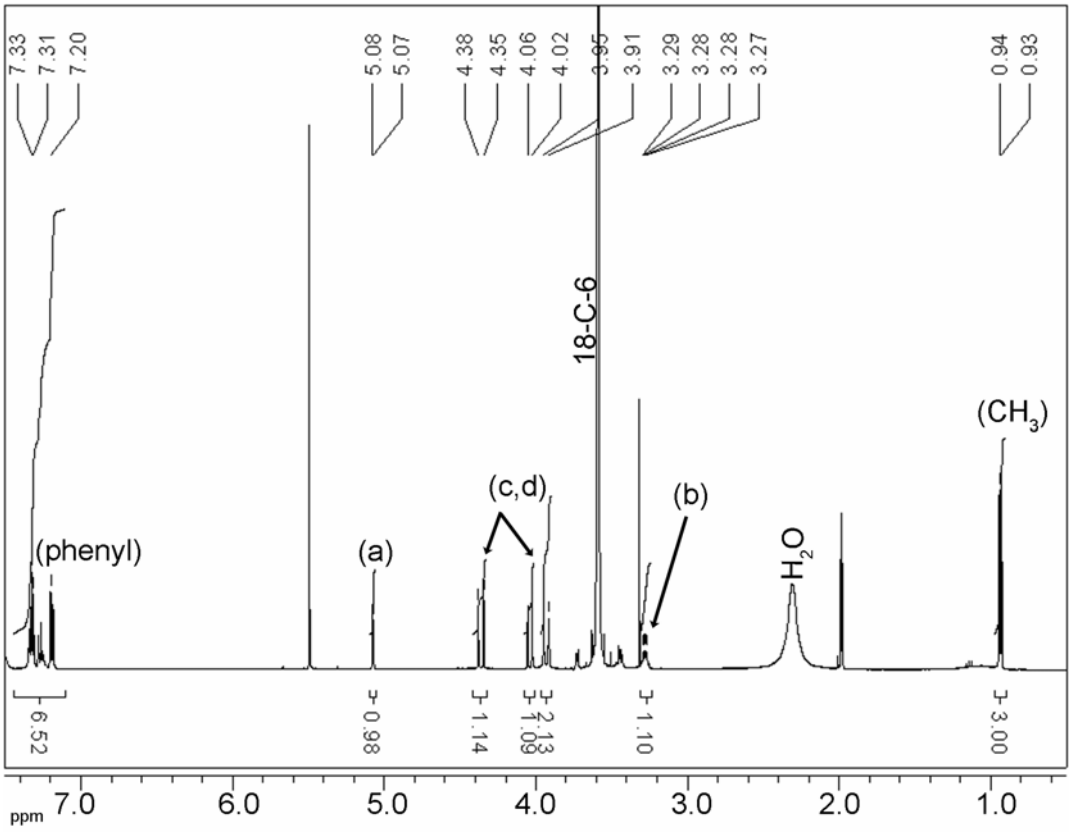

Figure 4.5: ^1H NMR Spectrum in acetonitrile-d_3 of K[$VO(O_2)$Hnorida].

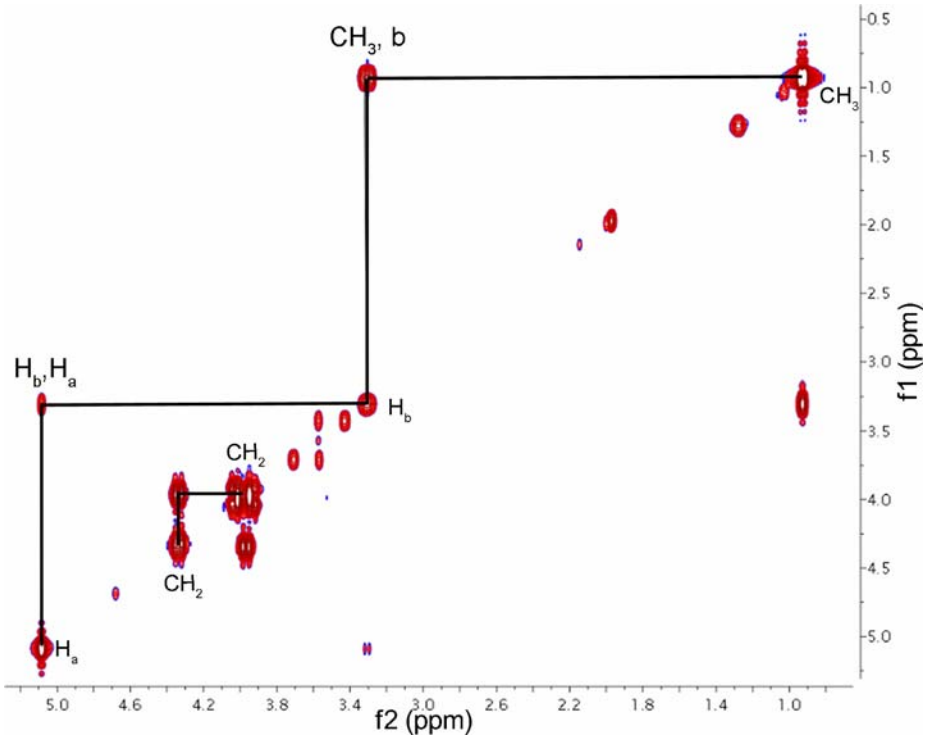

Figure 4.6: ^{1}H-^{1}H COSY Spectrum in acetonitrile-d_3 of K[VO(O_2)Hnorida].

As previously mentioned, K[VO(O_2)Hnorida] decomposes in solution within a few hours. The ^{1}H NMR of K[VO(O_2)Hnorida] in acetonitrile without peroxide after standing for 2.5 hours is presented in Figure 4.7. The methyl protons of the ligand set provide a well resolved spectroscopic handle for assessing the number of possible ligand containing species in solution. The appearance of eight new doublets in the 1.8 ppm – 0.5 ppm region indicate that a variety of ligand-containing species form upon decomposition. The aromatic region of the spectrum shows the same multiplet present in a freshly prepared sample along with the appearance of a two doublets and triplet between 8.0 and 7.6 ppm. These new aromatic peaks are consistent with the formation of an aromatic ketone from the two electron oxidation of the benzylic alcohol of the ligand. The ^{51}V NMR contains two dominant species, one corresponding to the original [VO(O_2)Hnorida]$^{-}$ complex at -520 ppm, and new resonance at -504 ppm (Figure 4.8). The downfield shift is consistent with a reduction in shielding of the vanadium nuclei, which may be attributed to either the lower donating ability of a ketone versus an alcohol or a vacant coordination site.

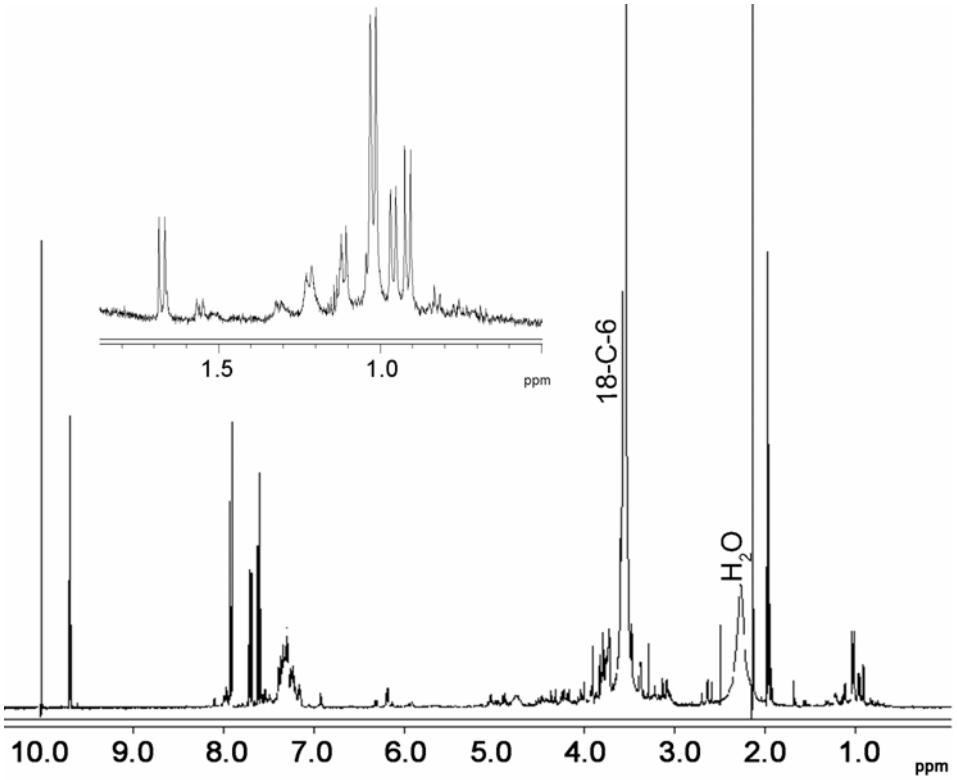

Figure 4.7: ^{1}H NMR Spectrum in acetonitrile-d_3 of partially decomposed K[VO(O_2)Hnorida]. Inset: expansion of methyl region

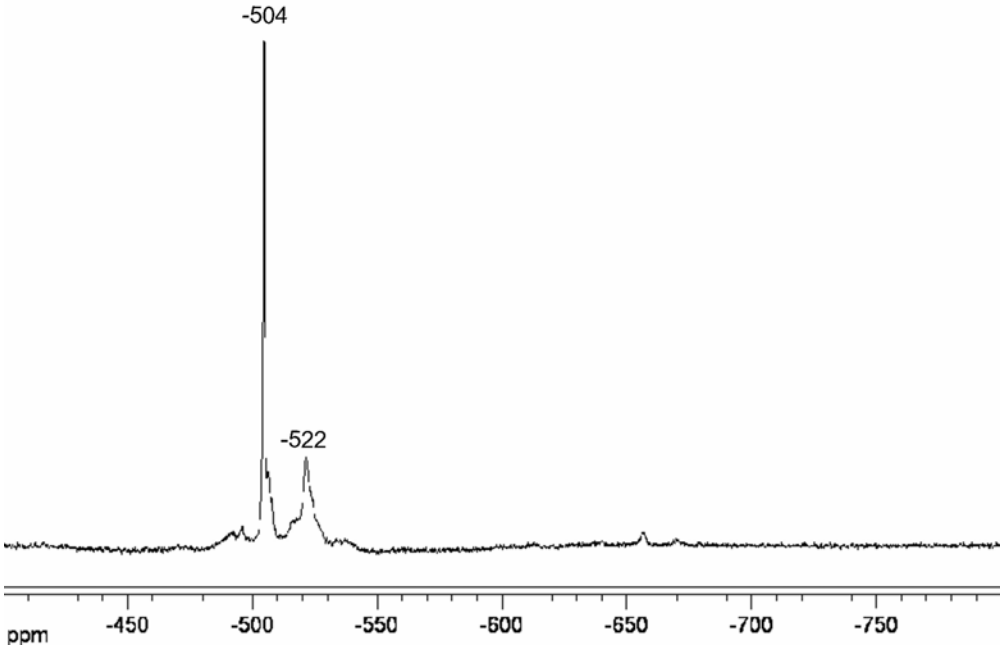

Figure 4.8: ^{51}V NMR Spectrum in acetonitrile-d_3 of partially decomposed K[VO(O_2)Hnorida].

In the presence of additional hydrogen peroxide, a similar ligand decomposition process occur with K[$VO(O_2)$Hnorida]. Immediately after dissolution of the vanadium in an acetonitrile solution containing 10 equivalents of hydrogen peroxide, new peaks appeared in the ^1H NMR spectrum (Figure 4.9). Two new methyl peaks appeared in the methyl region of the spectrum. The dominant doublet at 0.90 ppm corresponded to the peroxo-oxovanadium(V) species. In the ^1H-^1H COSY spectrum, a number of new cross-peaks appeared over the course of the COSY experiment (approximately 1 hour for data collection). There are more CH_3-H_b cross peaks than there are H_a, H_b couplings, indicating that the H_a proton has been eliminated. Additionally, the resolved protons show cross coupling with each other. The splitting and cross peaks in the ^1H NMR and COSY are consistent with the formation of an aromatic ketone (Figure 4.9 and 4.10). The ^1H NMR of the sample after the COSY experiment has a prominent water peak at approximately 2.5 ppm. The ^{51}V NMR of K[$VO(O_2)$Hnorida] with increasing concentrations of the hydrogen peroxide is presented in Figure 4.11. A single ^{51}V resonance is present in the absence of hydrogen peroxide at -520 ppm. The addition of a 10-fold excess of hydrogen peroxide generates a new vanadium species at -683 ppm which falls within the range of diperoxo vanadate species. Additional equivalents of hydrogen peroxide increase the intensity of the peak with respect to the K[$VO(O_2)$Hnorida] resonance and induces a slight upfield shift.

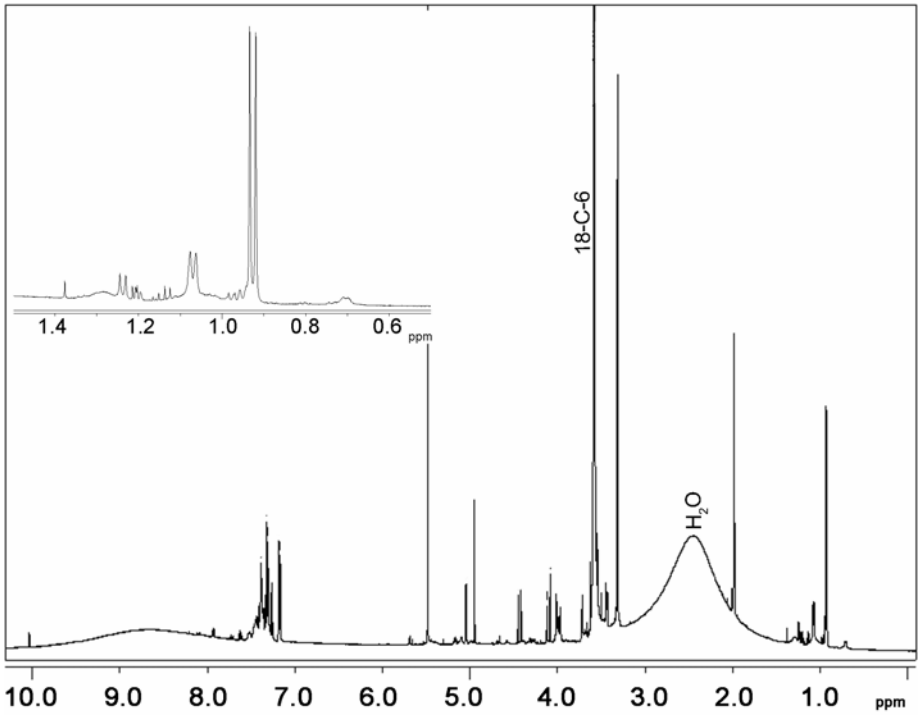

Figure 4.9: ^{1}H NMR Spectrum in acetonitrile-d_3 of K[VO(O_2)Hnorida] with 10 equivalents of H_2O_2. Inset: Expansion of the methyl region.

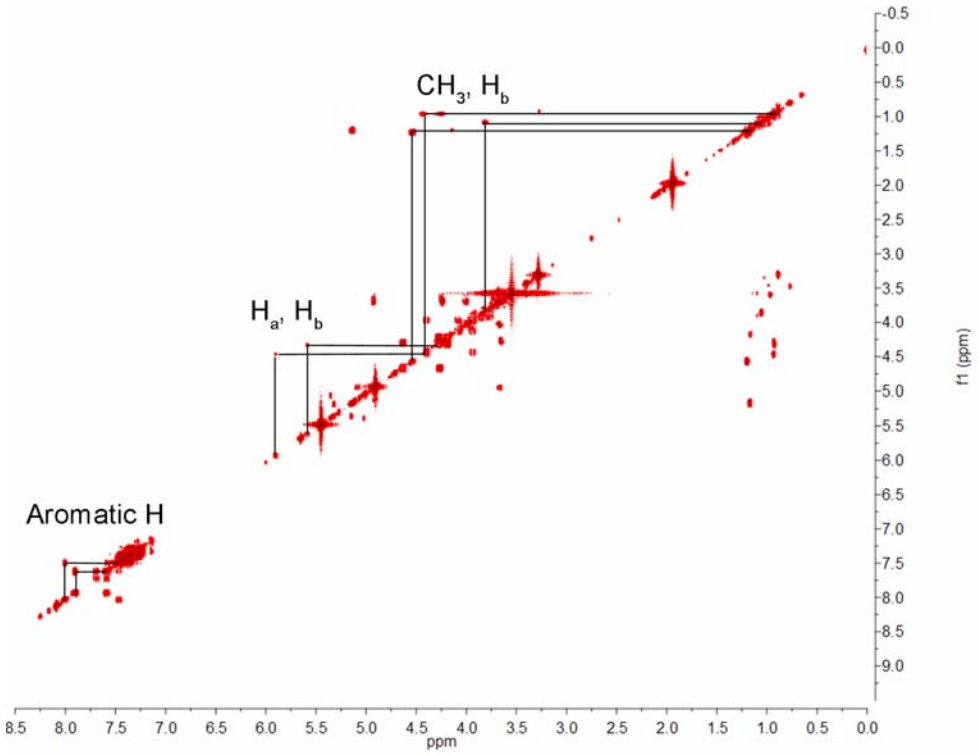

Figure 4.10: ^{1}H-^{1}H COSY spectrum in acetonitrile-d_3 of K[VO(O_2)Hnorida] with 10 equivalents of H_2O_2.

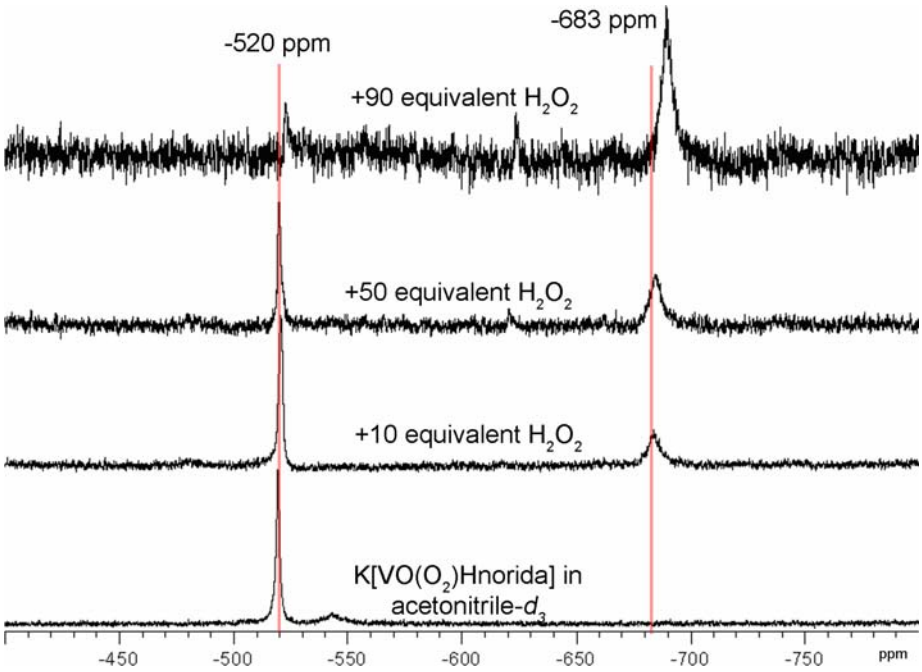

Figure 4.11: ^{51}V NMR spectrum in acetonitrile-d_3 of K[VO(O_2)Hnorida] with increasing equivalents of H_2O_2.

Kinetics of thioether oxidation

The formation of a new vanadium species upon addition of peroxide prompted an evaluation of the kinetics for thioether oxidation by K[VO(O_2)Hnorida]. The difference extinction coefficient between *p*-tolyl methyl sulfide and *p*-tolyl methyl sulfoxide at 290 nm is $\Delta\varepsilon$ = -0.81 mM^{-1} cm^{-1}. This provides a viable spectroscopic handle to monitor the oxidation of a thioether to sulfoxide. The choice of thioether used in this study was based on the ability to chirally resolve the resulting sulfoxides using a chirally derivatized normal phase HPLC column. Variations in the sulfide concentration at high peroxide concentrations are shown Figure 4.12. The initial rate varies regularly with increasing thioether concentration and the $t_{1/2} \approx 50$ seconds, is identical for all three concentrations tested. As the reactions proceed there is an increase in the rate of thioether oxidation as is evident by the increase in the curvature of line for

The dependence of the rate of the reaction on peroxide in presented in Figure 4.13. The reactions were performed at 200 mM vanadium, 2 mM thiother, and

200 mM triflic acid. The order of addition for all kinetic experiments is vanadium, hydrogen peroxide, thioether, and the reaction was initiated with a stock solution of triflic acid. A lag phase is present for sulfoxidation at $[H_2O_2] < 100 \times [V]$.

The proton dependence of thioether oxidation for K[VO(O_2)Hnorida is presented in Figure 4.14. The maximum rate was observed for one equivalent of H^+ and no reactivity was observed on these timeframes in the absence of H^+. Addition of 2 equivalents of H^+ increases the lag phase in the initial rate of thioether oxidation.

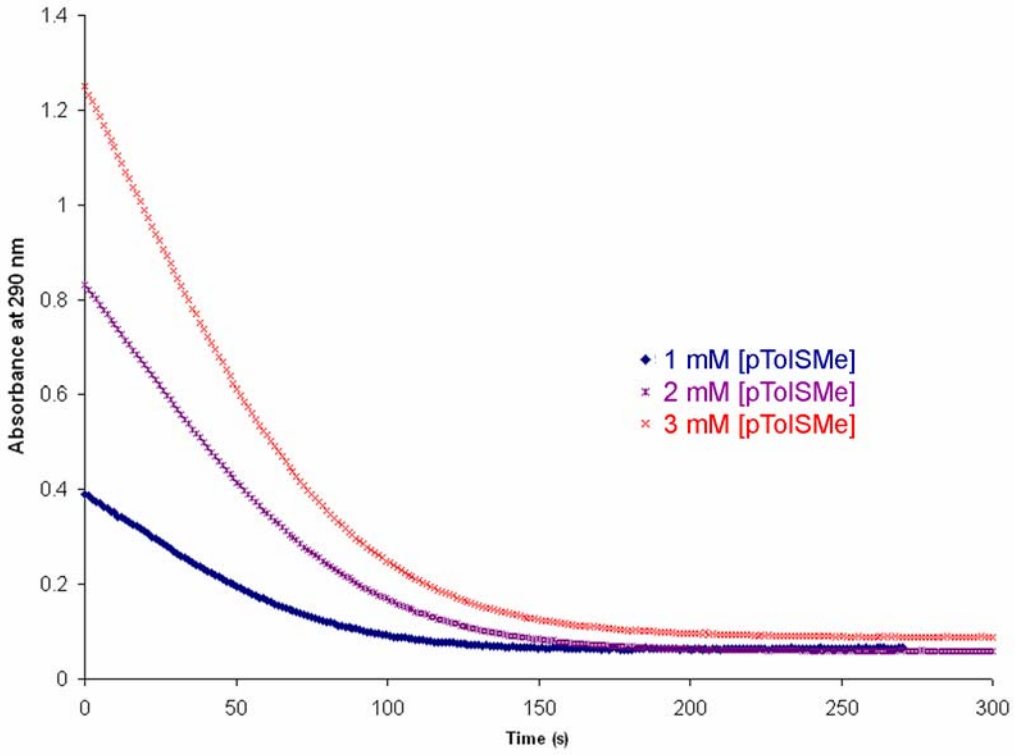

Figure 4.12: Sulfide dependence of thioether oxidation by K[VO(O_2)Hnorida]. Conditions (in order of addition): 0.2 mM [V], 0.4 mM [18-C-6], varying [pTolSMe], 50 mM [H_2O_2], and 0.2 mM [HTf] in acetonitrile.

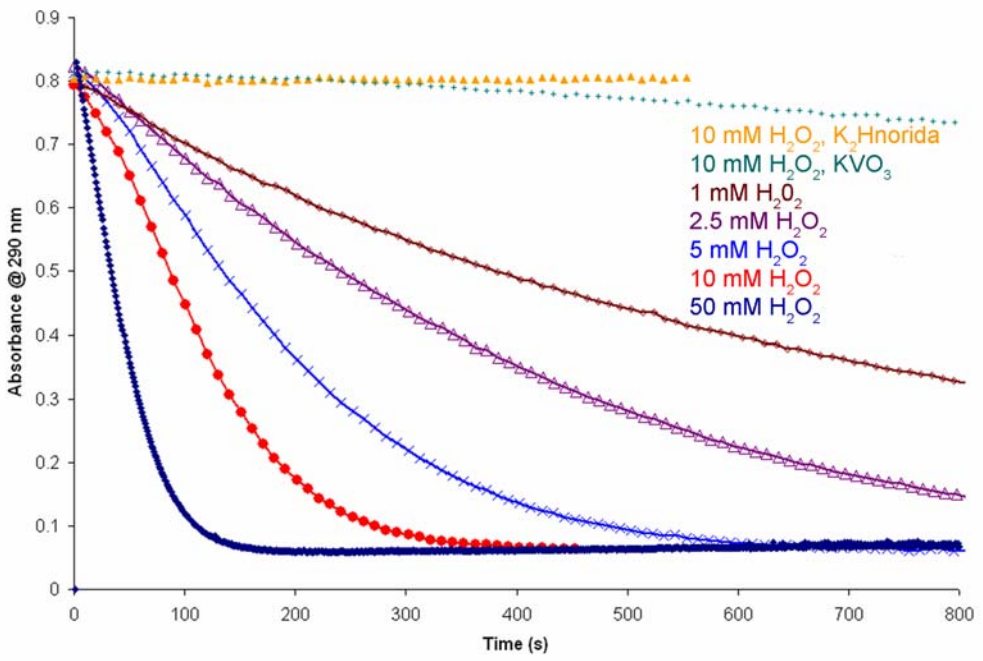

Figure 4.13: Dependence of thioether oxidation on peroxide concentration. All samples are K[VO(O_2)Hnorida] unless otherwise stated. Conditions (in order of addition): 0.1 mM [V], 0.2 mM [18-C-6], 2 mM [pTolSMe], varying [H_2O_2], and 0.1 mM [HTf] in acetonitrile.

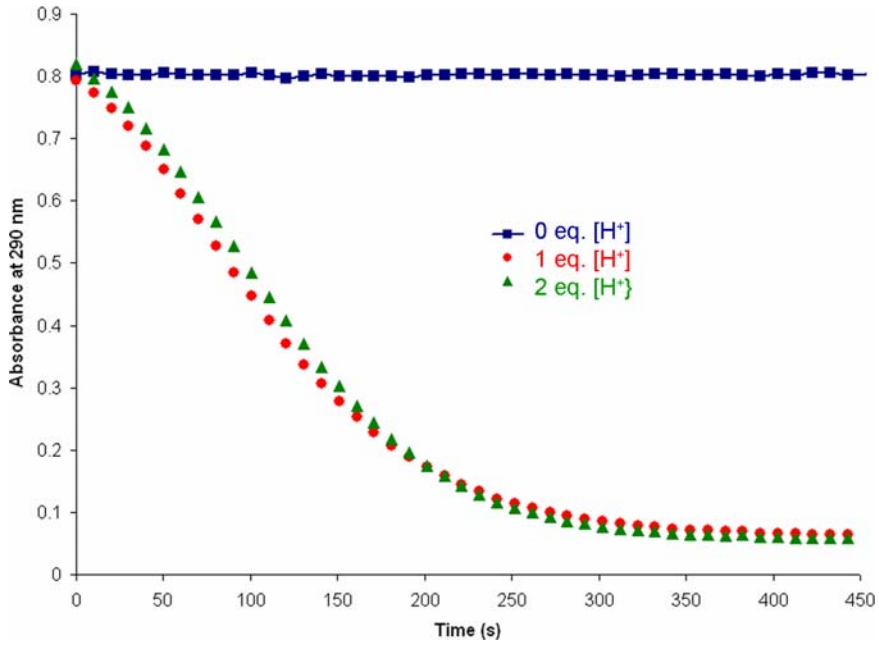

Figure 4.14: Proton dependence of thioether oxidation by K[VO(O_2)Hnorida]. Conditions (in order of addition): 0.1 mM [V], 0.2 mM [18-C-6], 2 mM [pTolSMe], 10 mM [H_2O_2], and varying mM [HTf] in acetonitrile.

Discussion

Asymmetric ligand design and complexation

The stereoselectivity of a catalyst can be attributed to energetic differences in the barrier to activation due to a variety of factors including, but not limited to, sterics, stability of pre-transition state adducts, hydrogen bonding of the substrate, preferential approach of the substrate to the reaction center, and substrate coordination to a Lewis acid. In the case of Sharpless-type epoxidation catalysts, coordination of the allylic alcohol to the metal center enforces a single geometry for the transition state; consequently, the enantioselectivity is very high.[8] While this methodology is highly effective, it limited to the substrates that contain an allylic alcohol. An alternative approach applies steric interactions in a chiral manner so as to induce a preferential approach of the substrate towards the reaction center. This is the case for a variety of asymmetric salen-type catalysts, such as the Mn(salen)[9] and Ti(salan)[10] discussed in Chapter 1. The van der Waals and steric interactions of the prochiral substrate with the chirally derivatized ethylene diamine backbone limit the possible approaches of the substrate to the reaction center, thereby reducing the number of possible stereochemical outcomes for the reaction. The preferential approach model is particularly applicable to the design of a chiral ligand for coordinatively saturated complexes.

Previous work has demonstrated that K[VO(O_2)Hheida] is a highly efficient sulfoxidation catalyst.[4] This work has focused on derivatizing the ligand set without modifying the electronics of the donor atoms to assess the effects of steric interactions on the stereoselectivity. The transition state geometries calculated in chapter 2 for VO(OOH)Hheida, demonstrate that both halide and sulfide oxidation undergo an S_N2-like oxo transfer process through a linear transition state.[11] Additionally, protonation of the peroxo moiety reduces the barrier to activation. Given the linear nature of the transition state and the pseudo-σ_V that bisects the O-O bond of the complex, there are two possible

approaches of the substrate to the hydroperoxo moiety, and each has two possible stereochemical outcomes (Figure 4.15). By breaking the pseudo-σ_V through the introduction of chiral steric bulk on the ligand set, a preferential approach of a thioether should induce some stereoselectivity for the oxo-transfer process.

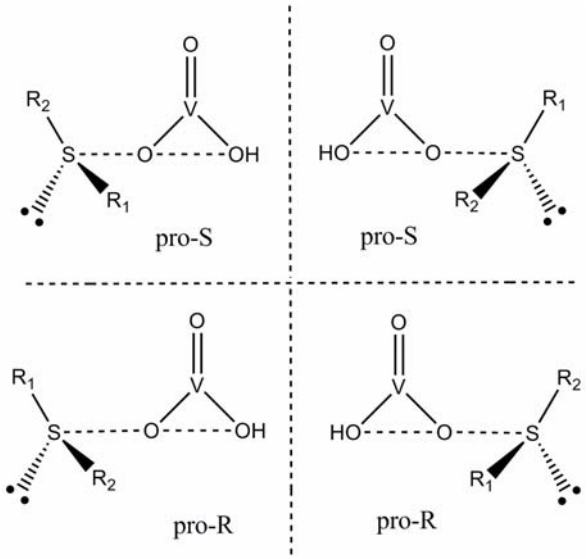

Figure 4.15: Four possible orientations of a pro-chiral sulfide in a linear transition state.

There are four sp^3-hybridized carbons in the $Hheida^{2-}$ architecture. As the hydroxy ethyl arm is positioned *trans* to the V=O and perpendicular to the peroxide donor, derivatization of this arm could break the pseudo-σ_V symmetry of the complex. Additionally, the C1 position of this donor arm is the closest potential source of chirality to the peroxo moiety. Three ligands were synthesized to explore the effects of derivatization of the hydroxyethyl arm of $Hheida^{2-}$ (Figure 4.16). The first iteration of ligand design involved placing a phenyl on the C1 carbon creating a chiral center near the peroxo moiety. The oxovanadium(IV) structure (Figure 4.2) of this ligand ($Hpheida^{2-}$) is identical to that observed for VO(Hheida). The V=O bond is *trans* to the nitrogen donor in the axial positions. The carboxylate donors are *trans* to each other with the hydroxyl group and water molecule filling the equatorial plane. Not surprisingly, the 5-membered chelate ring conformation of the hydroxyethyl arm positions the

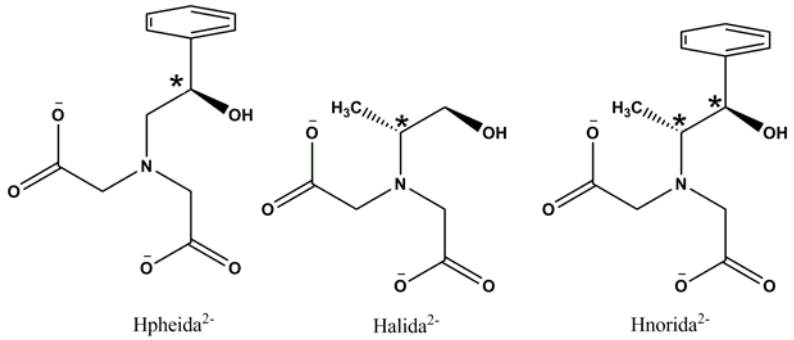

Figure 4.16: Ligands synthesized for asymmetric sulfoxidation.

bulkiest substituent, the phenyl group, as far away from the rest of the complex as possible. Attempts to isolate the peroxo-oxovanadium(V) complex of $Hpheida^{2-}$ were not successful; however, as the ligand binding mode for the oxovanadium(IV) complex is identical to that observed for VO(Hheida) it is reasonable to predict that $[VO(O_2)Hpheida]^-$ would be very similar to $[VO(O_2)Hheida]^-$. In this case, the phenyl group would not be located near either side of the peroxo moiety and, therefore, would have minimal effect on the enantioselectivity of the reaction.

Computational studies on Schiff-base type peroxo-oxovanadium(V) catalysts have shown that chiral derivatization of ligand positions positioned away from the reaction center can have a profound effect on chelate ring conformations.[12] The chelate ring conformation forces the stericically hindering functionalities closer to the reaction center, and consequently, dramatically enhancing the stereoselectivity. This information underscores the observation that the lowest energy ring conformation was adopted for VO(Hpheida). By controlling the ring conformation, we can place steric bulk closer to the reaction center and, thus, have a greater effect on the enantioselectivity. The second ligand synthesized for these studies was the N,N-diacetate derivative of norephedrine ($Hnorida^{2-}$). Norephedrine is a 1,2-aminoalcohol with a phenyl substituent on the C1 position and a methyl group on the C2 position. The (1S,2R) diastereomer places both sterically encumbering groups in a *cis*-conformation within a 5-membered chelate ring. Based on the binding mode of $[VO(O_2)Hheida]^{2-}$, the lowest energy ring conformation would place the phenyl

group near the hydroxyl in an equatorial position and methyl group in a pseudo-axial position within the chelate ring. The steric interactions of the methyl group with the methylene carbons of the carboxylate arms may destabilize the chelate ring conformation and force the phenyl group to orient more towards one side of the peroxo moiety. Complexation of $Hnorida^{2-}$ as a peroxo-oxovanadium(V) complex led to a surprising structural change in which the hydroxyl donor coordinates in the equatorial plane and a carboxylate coordinates *trans* to the V=O bond (Figure 4.1). This fortuitous coordination mode discriminates the left and right hand side of complex and has the potential to impart a preferential approach of the sulfide towards the peroxo ligand.

Our collaborators at the Unvieristy of Milano-Biccoca, Prof. Luca DeGioia and Giuseppe Zampella, have calculated the energetic differences for the three possible coordination modes of $HNorida^{2-}$ and the corresponding pro-S and pro-R transitions with methyl phenyl sulfide. Interestingly, the equatorial coordination of the hydroxyl group determined in the X-ray crystal structure is not the lowest energy confirmation. Coordination of the hydroxyl group in the axial position *trans* to the oxo is more stable by 6.3 kcal/mol. The reason for this difference is likely correlated to differences in solubility and crystal packing forces that favor the equatorial coordination mode. This information provided the basis to estimate the enantioselectivity for $[VO(O_2)Hnorida]^-$. By taking into account the barrier to activation and the differences in ground state energies for pro-R and pro-S transition states, we can estimate the enantiomeric excess for Hnorida with hydrogen peroxide using a Boltzmann analysis (Table 4.4). The data available only accounts for the left hand approach of sulfide to the sulfoxide. The enantiomeric excess based on this approach is 99% in favor of the R enantiomer. In the absence of the transition states accounting for a right side approach of the sulfide, a reasonable estimate of the effects on the %ee can be made using two assumptions: 1) the barrier to activation for both pro-R and pro-S transitions are nearly equal in magnitude to the barrier to activation for a left side approach and 2) the lack of steric bulk oriented on the right hand side of the molecule would lead little energetic discrimination between the pro-R and pro-S transition (i.e. the

oxidation is racemic for a right side approach of the sulfide). Based on these assumptions the %ee is 59%.

Table 4.4: Barriers to activation calculated by Giuseppe Zampella for K[VO(O_2)Hnorida] with H_2O_2. All energies are in kcal/mol. [a] = Estimated values accounting for a Right side approach of the substrate to the peroxo moiety.

Coord Mode/Approach	Stereochem	$\Delta G^{\ddagger}$	Ground State	Adjusted Barrier	Ni/N
Axial/Left	R	11.6	0	11.6	0.600
Eq. Left/Left	R	10.7	9.5	20.2	7.86×10^{-8}
Axial/Right[a]	R	11.6	0.6	12.2	0.198
Axial/Right[a]	S	11.6	0.6	12.2	0.198
Axial/Left	S	14.6	0	14.6	0.002
Eq. Left/Left	S	9.7	9.5	19.2	4.96×10^{-7}

A third ligand derivative was prepared after the completion of the enantioselectivity studies discussed below to explore the effects of C2 derivatization on the stereoselectivity of thioether oxidation. The N'N – diacetate of L-alaninol (Halida^{2-}) was isolated as the peroxo-oxovanadium(V) form as is evident by the FTIR and ESI$^-$/MS. Crystals suitable for x-ray diffraction were not obtained, and consequently, a discussion of the solid state structure in the context of [VO(O_2)Hnorida]$^-$ is not possible. The structural determination of this complex as well as a detailed reactivity studies, could provide interesting insight into the factors controlling the reactivity of chiral tripodal amine type complexes and will be discussed in the future work in Chapter 5.

Enantioselectivity of asymmetric sulfoxidation by designed chiral catalysts

Prof. Luca DeGioia and Giuseppe Zampella, Ph.D calculated the transition states for the peroxo- and *t–butyl peroxo* and energetics for the three potential coordination modes of Hnorida^{2-}. The most stable coordination mode is identical to that of [VO(O_2)Hheida]$^-$, in which the carboxylate oxygen atoms bind in the equatorial plane. Transition states were also calculated for the hydroperoxo species; however, approach of the sulfide from the right hand side of the complex is not yet calculated. Based on the calculated barriers to activation for Pro-R and

Pro-S transition states, the enantiomeric excess is 99% in favor of the R enantiomer. Assuming that the right-hand approach of the thioether to the complex yields a racemic sulfoxide, the resulting %ee would be reduced to 56%. The barriers to activation for the *t*-butylperoxo species for all coordination modes with predict an 88% enantiomeric excess in favor of the *R*-enantiomer. As was the case for the hydroperoxo species, these calculations do not account for the right hand side approach of the sulfide to the complex. Assuming the right hand side approach to the complex results in a racemic sulfoxide, the resulting %ee is 44%. These calculations accurately predict the stereochemical outcome of the reaction; however, they do not accurately reproduce the %ee. As was the case for the energetics of protonation presented in chapter 3, these activation barriers represent the largest possible difference. Small differences in the activation barriers will result in a lower enantioselectivity.

The ligand design strategies employed described above are aimed at biasing the approach of sulfide to the reactive ligand, peroxide. The proof of concept for the ligand designed above is to perform an asymmetric sulfoxidation. These studies focus on exploring the experimental conditions necessary to carry out asymmetric sulfoxidations. As an environmentally benign and inexpensive oxidant, hydrogen peroxide is the optimal choice to carry out asymmetric oxidative catalysis. The lack of steric bulk in hydrogen peroxide requires that the stereoselectivity in the transition state arises exclusively from interactions of the catalyst and substrate. As an alternative approach, the use of organic peroxides provide extra steric bulk when coordinated to the catalyst, thereby potentially reducing the number of stereochemical outcomes for the reaction. Table 4.2 summarizes the data obtained from the stereoselective oxidation of *p*-tolyl methyl sulfoxide under a variety of conditions.

As would be expected, the achiral complex [$VO(O_2)$Hheida] yields racemic sulfoxide under typical reactivity conditions (acetonitrile, hydrogen peroxide, one equivalent of H^+). The use of a *t*-butyl hydroperoxide has no affect on enantioselectivity of the reaction. These results are consistent with the pseudo-σ_V symmetry of the complex that allows for approach of the substrate to either

side of the peroxo moiety. The transition state geometry calculated in Chapter 2 was used to model the geometric constraints of a pro-R and Pro-S transition state for a prochiral sulfide (Figure 4.17). There are no significant steric clashes in either orientation of the thioether, and this correlates well with the lack of stereoselectivity for this reaction.

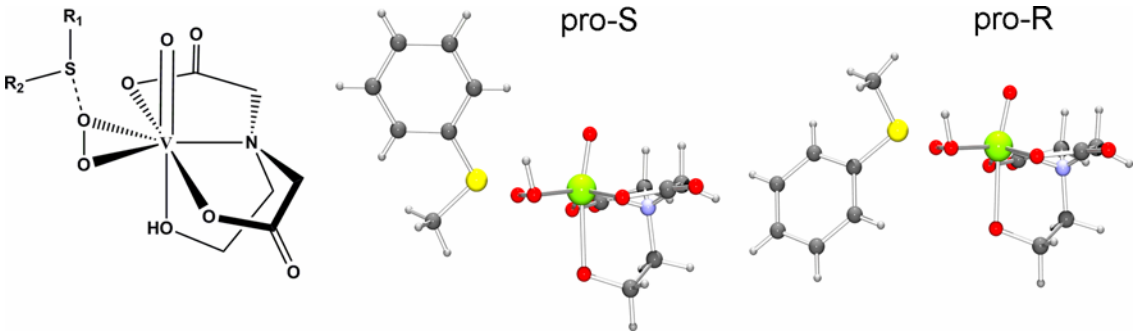

Figure 4.17: Stereochemical orientations of methyl phenyl sulfide in the transition state calculated for VO(OOH)Hheida

The asymmetric catalysts K[VO(O_2)Hnorida] shows no enantioselectivity in acetonitrile with hydrogen peroxide or organic peroxides. The lack of selectivity for sulfoxidation can be explained by a number of factors. One of which is the partial dissociation of ligand set. In the absence of peroxide, ESI^-/MS, ^1H NMR, and ^1H-^1H COSY indicate that the ligand is still coordinated to the vanadium center; however, the methylene protons of the carboxylate donor shows three peaks with J^2 coupling that may be consistent with a fully coordinate ligand or to dissociation of the hydroxyl arm. The discussion of the solution speciation of K[VO(O_2)Hnorida] is presented in detail later in this chapter. The ^{51}V NMR shows a single vanadium species in the expected range for monoperoxo-oxo complex. Upon addition of hydrogen peroxide, a new ^{51}V resonance appears in the expected range for a diperoxovanadate.[7,13] Diperoxovanadates have been shown to carry out sulfide oxidation in acetonitrile/ethanol mixtures.[14] In addition, previous studies have shown that enantioselectivity of disulfide oxidation with Bolm-type oxidation systems and hydrogen peroxide, is highly solvent dependant.[3] The selectivity of the reaction tracks roughly with the miscibility of

the solvent with water. The typical biphasic reaction conditions limit the concentration of hydrogen peroxide in the organic layer, thereby limiting the generation of a variety of peroxo-vanadate species. Reducing the rate of hydrogen peroxide addition to the solution further enhanced the stereoselectivity of disulfide oxidation. The ^{1}H and ^{51}V NMR spectra of K[VO(O_2)Hnorida] in acetonitrile are consistent with the formation of a diperoxovanadate species, that has been reported to carry out sulfide oxidation in a non-stereoselective manner.[14]

The lack of enantioselectivity for thioether oxidation with H_2O_2 can be attributed to the formation of non-selective oxidants. The computational models used to design the ligand and to estimate the enantioselectivity of this reaction do not account for the complex instability under the reaction conditions used. Care must be taken in synthesis of the catalysts in order to avoid potential instability under the reaction conditions used.

The strong solvent dependence on the enantioselectivity for Bolm-type sulfoxidation systems prompted investigation dependence of stereoselectivity on the enantioselectivity of K[VO(O_2)Hnorida]. The biphasic conditions employed for the use of hydrogen peroxide with ethyl acetate, dichloromethane, and toluene all resulted in racemic sulfoxide. In the presence of the strong oxidant, cumyl hydroperoxide, no enantioselectivity is observed for sulfoxidation, despite the greater steric bulk of the cumyl group. At room temperature, cumyl hydroperoxide is capable of carrying out the sulfoxidation reaction in the absence of vanadium. The generation of a non-selective oxidant through ligand oxidation and the background rate of sulfoxidation by cumyl hydroperoxide contribute to the loss of enantioselectivity at room temperature. The use of *t*-butyl hydroperoxide increased the enantioselectivity to 11% in favor of the (R)-sulfoxide. It is important to note that in the absence of an additional equivalent of proton, no enantioselectivity was observed. In the absence of a proton, the rate of reaction drops dramatically from approximately 4 hours to 24 hours. This reduction in the rate of sulfoxidation is consistent with the proton dependence of [VO(O_2)Hheida]$^{-}$, where the proton serves to activate the complex for oxidation

and assists in the binding of peroxide to the vanadium co-factor. The slow sulfoxidation reaction with K[VO(O_2)Hnorida] allows for non-selective oxidants such as an oxidized ligand complex of Hnorida^{2-} or sulfoxidation with t-butyl hydroperoxide to dominate the stereoselectivity.

The presence of excess hydrogen peroxide facilitates the decomposition of K[VO(O_2)HNorida]. In the absence of hydrogen peroxide, this complex is capable of stoichiometric sulfoxidation at a very slow rate, 36 hours for a single turnover. The single turnover experiments with K[VO(O_2)Hnorida] show a 26.3 %ee in favor of the (S)-sulfoxide in the absence acid, confirming that the designed catalyst is capable of asymmetric oxidations. This result also lends further support to the hypothesis that in the presence of hydrogen peroxide, non-selective oxidants are being generated and dominate the reactivity. The slow rate of oxidation be explained by the absence of H^+ necessary to activate the complex. It is likely that an intramolecular H-bond between the ligand and the peroxo moiety serves to partially activate the complex (Figure 4.18a). The only H-bond donor in the ligand set is the alcohol proton. In order for the alcohol proton to form a hydrogen bond with the peroxo moiety the N-hydroxyethyl arm must bind in the equatorial position. The possible diastereomeric confirmations associated with the equatorial coordination of the N-hydroxyethyl arm of the ligand set is likely responsible for the low enantioselectivity. Despite the low enantioselectivity, the single turnover experiment further supports the role of H-bonding interactions in the activation of metal peroxo complexes, such as $Ti^{+4}O_2$(salan)[15] and VHPOs.[16,17] Additionally, hydrogen bonding with the peroxo ligand may be exploited in a variety of d^0 metal-peroxo complex to facilitate the preferential approach of a substrate.

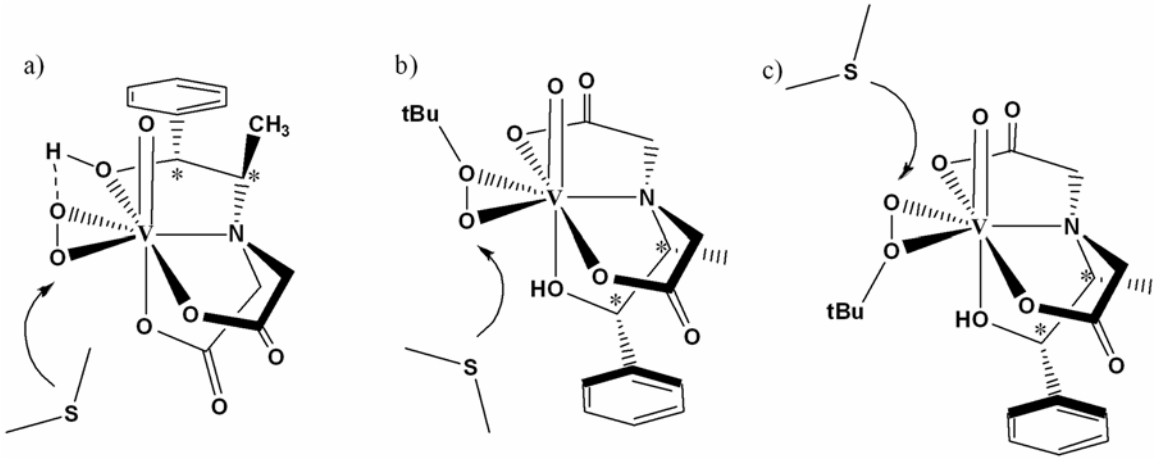

Figure 4.18: Most stable coordination mode capable of forming a hydrogen bond with the peroxo moiety of K[VO(O_2)HNorida] (a). The most stable coordination modes for *t*-butylperoxide K[VO(O_2)HNorida] and the approach of dimethyl sulfide to the reactive oxygen (b and c). All calculations for K[VO(O_2)HNorida] were performed by Prof. Luca DeGioia and Giuseppe Zampella, Ph.D.

In contrast to the single turnover experiment, the catalytic reaction with organic peroxides generates the *R*-sulfoxide. Based on the calculations for VO(OO*tButyl*)Hnorida, axial coordination of N-hydroxyethyl arm is the energetically favorable form of the complex (Figure 4.18b and c). In contrast to the single turnover experiment, which requires the equatorial coordination mode of the ligand, the *t-butyl* species favors the axial coordination mode. The difference in binding modes for these two cases may explain the difference in the enantiopreference for between the single turnover reaction and the catalytic *t-butylperoxide* reaction.

No enantioselectivity is observed under turnover conditions with hydrogen peroxide and one equivalent of acid. The energetic difference between protonation of the left or right hand side peroxo-oxygen atom is small; consequently, both protonated forms would exist in solution resulting in the sulfide approach from both sides of the peroxo moiety. This lack of preferential approach to the complex results in both *R*- and *S*-sulfoxide being formed.

The use of dicholoromethane, instead of acetonitrile, enhanced the stereoselectivity of sulfoxidation by K[VO(O_2)Hnorida] with *t*-butyl hydroperoxide as the terminal oxidant. The competitive sulfoxidation of the terminal oxidant coupled with potential generation of non-selective vanadium species prompted

the exploration of low temperature reaction conditions. Lowering the temperature of the reaction to 0 °C enhanced the stereoselectivity for both organic peroxides employed in these studies. The *t*-butyl hydroperoxide %ee increased to 14% in favor of the (S)-enantiomer and cumyl hydroperoxide imparts a 19% ee in favor of the (S)-enantiomer. A large number of possible coordination modes exist for cumyl peroxide binding to vanadium. Recent studies have shown that cumyl peroxide binds in an end-on fashion to sterically encumbered aminoalcoxides and the conformational flexibility reduces the enantioselectivity of sulfoxidation.[18] This conformational flexibility provides a potential explanation for the relatively low enantioselectivities observed for asymmetric sulfoxidation with K[VO(O_2)Hnorida] with organic peroxides.

Solution speciation and reactivity of K[VO(O_2)Hnorida]

The focus of the studies presented to this point has been on the design of an asymmetric sulfoxidation catalysts that is based on calculated transition states for a model system. To this end, I have identified factors that may control the stereoselectivity of the reaction and focused on developing a ligand set to impart a preferential approach of the substrate towards the reaction center. The resulting ligand is capable of stereoselective oxidations in a stoichiometric fashion and obtains marginal %ee for the catalytic process in the presence of an organic peroxide. Non-selective oxidants appear to play a significant role in the sulfoxidation system design above. Solution speciation studies and kinetics measurements discussed here provide additional support for the role of non-selective oxidants in the asymmetric sulfoxidation reactions.

Given the strong solvent dependence on the stereoselectivity on solvent, an understanding of the potential solution species in acetonitrile provides insight into the competing factors for stereoselectivity. The ^{1}H NMR of a freshly prepared K[VO(O_2)Hnorida] in acetonitrile shows a single set of resonances that are assigned on the basis of their coupling constants and ^{1}H-^{1}H COSY spectrum. The three doublets that exhibit J^2 coupling in the ^{1}H NMR correspond to the

diastereotopic methylene protons of the carboxylate arms. The potassium salt of K_2Hnorida exhibits two diastereotopic doublets. Based on the proton NMR, the carboxylates of Hnorida^{2-} are coordinated to the metal center; however, based on the splitting of the peaks, a distinction cannot be made between a *trans*-carboxylate configuration similar to [VO(O_2)Hheida]$^-$ or the *cis*-carboxylate configuration observed in the crystal structure of K[VO(O_2)Hnorida]. Coordination of the chirally derivatized hydroxyethyl chelate arm can not be determined on the basis of the ^{1}H NMR or COSY spectra. The insolubility of the K_2Hnorida in acetonitrile prevents a correlation of the chemical shifts for the protons on the hydroxyethyl arm with the peroxo-oxovanadium(V) complex. K[VO(O_2)HNorida] shows a single ^{51}V NMR resonance at -520 ppm, which is in the range expected for with peroxo-oxovanadium(V) species. These results are consistent with the formation of a single VO(O_2)L species.

Dissolution of K[VO(O_2)Hnorida] does not cause the loss of ligand or the generation of other vanadium(V) species. However, over time a slow ligand oxidation step is apparent and the splitting of the aromatic protons of a partially decomposed complex shows the formation of an aromatic ketone (Figure 4.7). This observation is consistent with oxidation of the benzylic alcohol of Hnorida^{2-} generating an acetophenone functional group. Additionally, multiple new doublets appear in the chemical shift range for the chiral methyl group (0.8 ppm – 1.8 ppm). This decomposition process leads to multiple ligand species in solution. The ^{51}V NMR of the partially decomposed product shows a new dominant peak at -504 ppm and a lower intensity peak at -522 (Figure 4.8). Multiple low intensity and broad peaks overlap with the two major resonances. The downfield shift of the of ^{51}V resonance is consistent with the reduction of electron density on the vanadium, this could arise from the oxidation of the ligand and the loss of the peroxide moiety. This decomposition provides a partial explanation for the lack of enantioselectivity in acetonitrile. The oxidation of the ligand set removes the chirality of the C1 position, thereby eliminating the majority of the chiral steric bulk (Figure 4.19). Additionally, the two-electron oxidation of a benzylic alcohol to a ketone generates one equivalent of H^+ per

oxidized ligand, thereby changing the proton concentration of the system and potentially facilitating further decomposition.

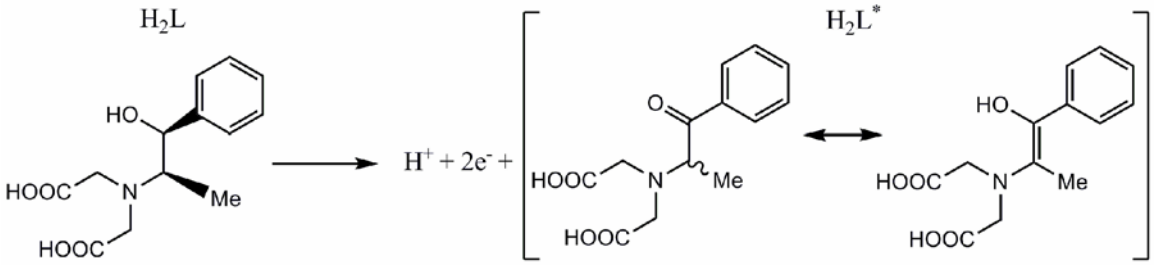

Figure 4.19: Oxidation of H_3norida.

In addition to ligand decomposition, the presence of 10 equivalents of hydrogen peroxide in an acetonitrile solution of K[VO(O_2)Hnorida] causes a substantial change in the number of vanadium and ligand-containing species in solution. Upon addition of hydrogen peroxide, a new peak appears at -683 ppm, consistent with the formation of a diperoxo-oxovanadium(V) species that does not contain ligand. The presence of multiple doublets and their corresponding cross peaks in the ^{1}H NMR and ^{1}H-^{1}H COSY spectra, indicate that more than one ligand-containing species is present. The ^{51}V NMR and ^{1}H NMR demonstrate that in the presence of excess hydrogen peroxide K[VO(O_2)Hnorida] is converted to a diperoxo-vanadate species in acetonitrile. This observation explains the reduction in enantioselectivity, assuming the diperoxovanadate species that is formed in catalytically competent. The kinetic competence of this species will be discussed later in this chapter. The formation of a diperoxo vanadate species generates two protons from the side-on coordination of hydrogen peroxide. K[VO(O_2)Hnorida] quickly decomposes in organic solutions at proton concentrations greater than one equivalent. A mixture of V^{+4} and V^{+5} are thought to give the brown color of the solution. The complex mass spectrum contains numerous peaks, none of which correspond to an identifiable ligand-vanadium complex.

The instability of K[VO(O_2)Hnorida] in acetonitrile in the presence and absence of hydrogen peroxides provides support for the formation of non-

selective oxidants. In contrast, K[VO(O_2)Hnorida] in dichloromethane is surprisingly stable. The ESI^-/MS shows a single peak at m/z: 364, consistent with the $[VO(O_2)L]^-$ anion. Figure 4.20 depicts the ^{51}V NMR of the complex solubilized in dichloromethane and resulting spectra changes upon addition *t*-butyl hydroperoxide, HTf, and substrate (Figure 4.20 and 4.21). No evidence of ligand oxidation is observed after the complete consumption of the substrate. In comparison to the acetonitrile/hydrogen peroxide system, the dichloromethane/*t*-butyl hydroperoxide is significantly more stable under catalytic conditions. The lack of diperoxovanadate formation and a reduced rate of ligand oxidation enhance the stereoselectivity of the reaction.

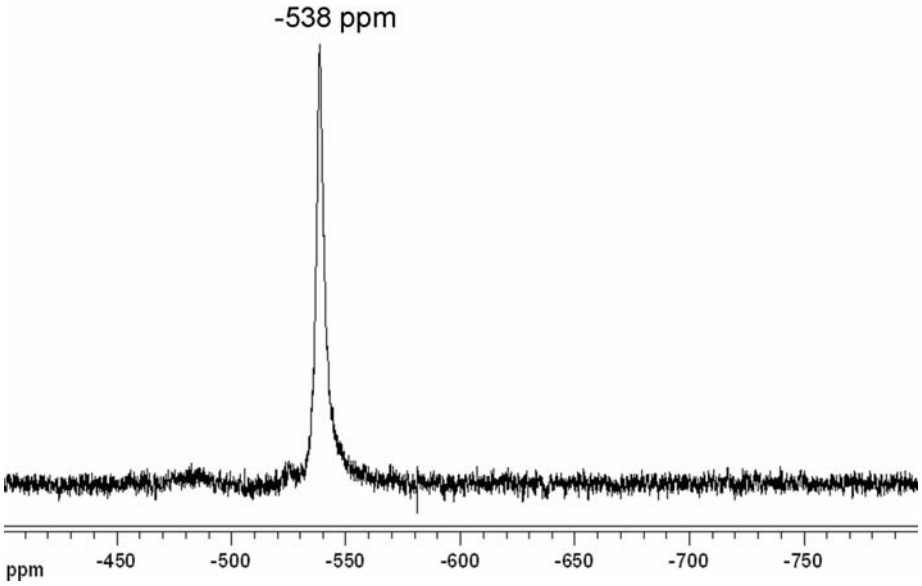

Figure 4.20: ^{51}V NMR of 1mM K[VO(O_2)Hnorida] solubilized in CD_2Cl_2 with 2 equivalents of 18-C-6.

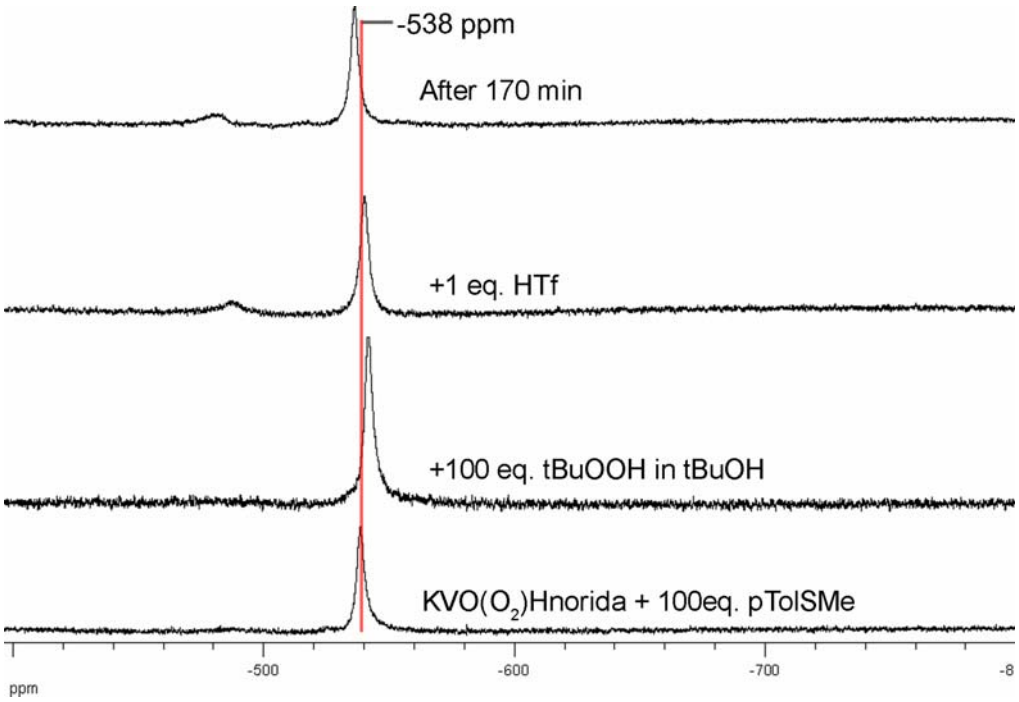

Figure 4.21: ^{51}V NMR spectra monitoring the affects of reagent addition on a 1mM K[$VO(O_2)$Hnorida] in CD_2Cl_2 with 2 equivalents of 18-C-6.

The effects of substrate and H_2O_2 concentration on K[$VO(O_2)$Hnorida]

The rate of substrate oxidation has a complex dependence on the concentration of acid, thioether, and hydrogen peroxide. Varying the concentration of the thioether resulted in identical initial rates and half-lives ($t_{1/2} \approx$ 50 seconds). However, the rate of substrate consumption increase over the course of reaction as is evident by the steeper curvature of the 3 mM pTolSMe trace after 78 seconds in comparison to the 1 mM trace at the initiation of the reaction (Figure 4.12). Additionally, there is a lag phase associated with the onset of substrate oxidation. These two factors indicates that this reaction is not ideally first order and other chemical processes are affecting the kinetics. The lag phase and the increase in the rate of sulfide oxidation over the course of reaction are likely due to the rate limiting formation of diperoxovanadate from K[$VO(O_2)$HNorida]. The solution speciation studies show that coordination of a second equivalent of hydrogen peroxide to K[$VO(O_2)$HNorida] facilitates the dissociation of the ligand set from vanadium. Given that the concentration of

vanadium in solution is small compared to all other reagents and that the rate of diperoxovanadate formation is dependent upon the concentration of hydrogen peroxide, the rate of sulfoxidation should saturate at high concentrations of hydrogen peroxide. The rate of sulfoxidation increases with increasing H_2O_2 with half-lives ranging from 45s to 605s. A plot of the rate, estimated from the half-life, versus the hydrogen peroxide concentration begins to saturate at concentrations higher than 10 mM (Figure 4.22). This behavior is consistent with the formation of diperoxovanadate being rate limiting and therefore contributing to the lag phase and increasing rate of sulfoxidation over time. The proposed mechanism based on the kinetic measurements is presented in Figure 4.23.

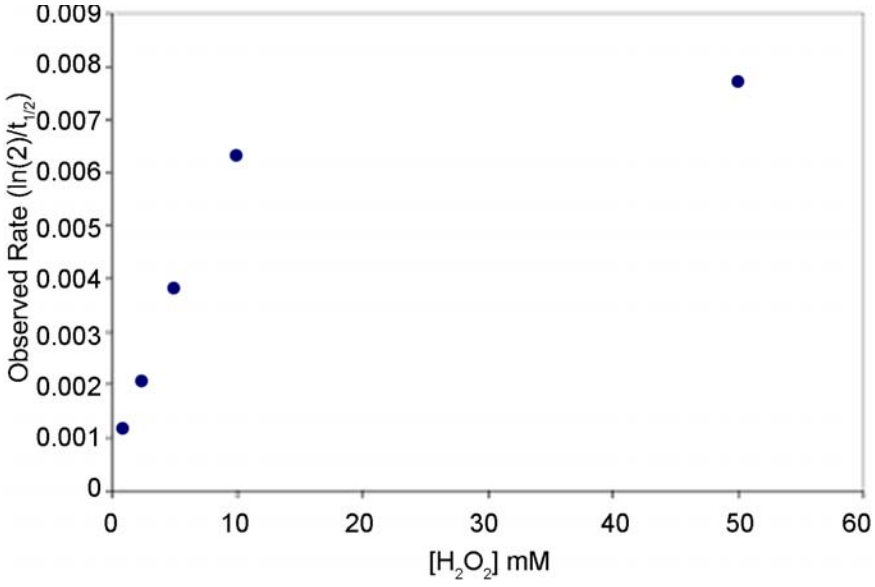

Figure 4.22: A plot of the observed rate of thioether oxidation by K[VO(O_2)HNorida] versus hydrogen peroxide concentration.

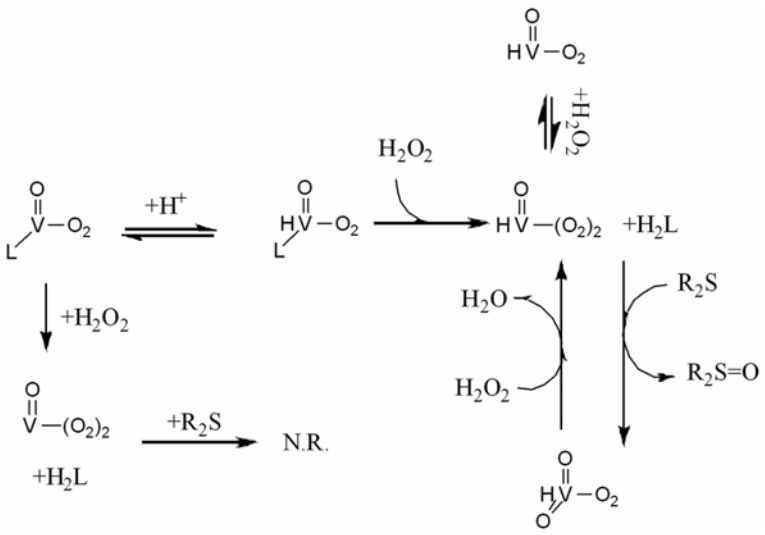

Figure 4.23: Proposed mechanism for the formation of diperoxovanadates from K[VO(O_2)Hnorida] with hydrogen peroxide in acetonitrile accounting for the reported kinetics of $VO(O_2)^-$.[14]

Espenson and co-workers have shown that $[VO(O_2)_2]^-$ oxidizes thioethers and phosphines in 50/50 mixtures of acetonitrile and water with 100 mM $[H^+]$.[14] In the presence of excess hydrogen peroxide the sulfoxidation reaction is first order in substrate concentration. The rate expression for sulfoxidation with diperoxovanadate contains the peroxide dependent equilibrium between VO_2^+, $VO(O_2)^+$ and $VO(O_2)_2^-$. The second order rate constant for the oxidation *p*-tolyl methyl sulfoxide by $VO(O_2)_2^-$ is 13.0 L mol^{-1} s^{-1}. A crude estimate of the rate constant for sulfoxidation from an initial rate fit to the integrated first-order rate law. A plot of ln[S] versus time gives a slightly curved line where the slope of the linear regression yields the pseudo first-order rate constant (Figure 4.24). The pseudo-first order rate constants obtained from the integrated rate law average to 1.53×10^{-2} s^{-1}. Table 4.5 summarizes the estimated rate constants obtained from the substrate dependence. Accounting for the concentration of vanadium in the estimated pseudo first-order rate constant derived from the sulfide dependence, the corrected rate constant is 7.65 L mol^{-1} s^{-1}. The factor of two difference between

Table 4.5: Pseudo-first order rate constant from substrate dependence

[pTolSMe]	$t_{1/2}$ (s)	k_{obs} from $t_{1/2}$ (s^{-1})	k_{obs} from ln([S]/[S]$_0$) (s^{-1})
5 eq.	50.4	0.0137	0.0149
10 eq.	50.4	0.0137	0.0157
15 eq.	50.4	0.0137	0.0153

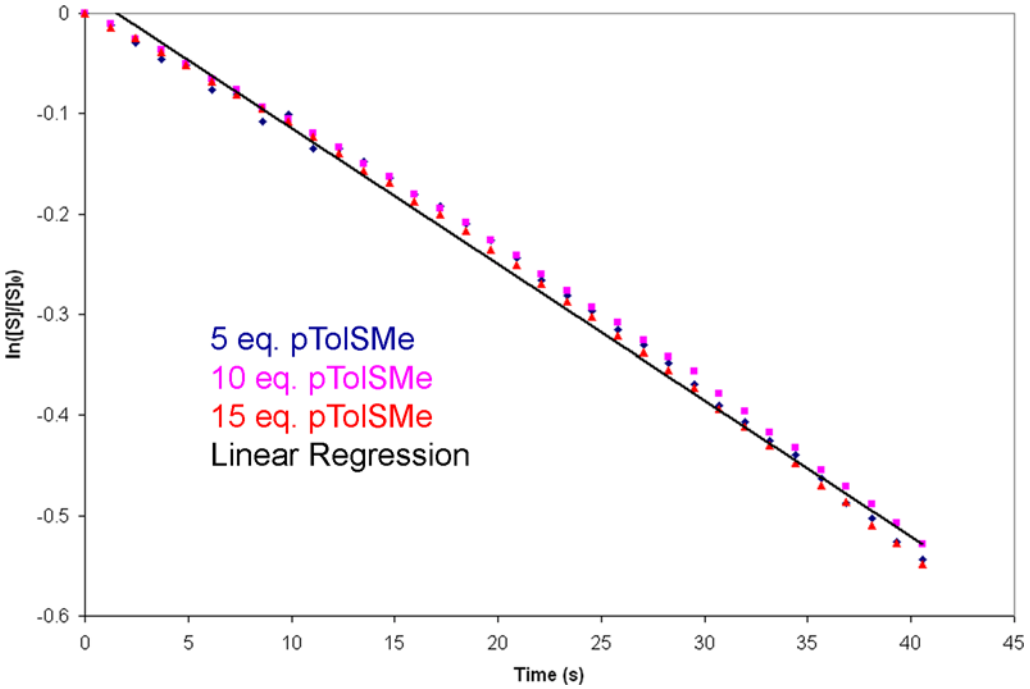

Figure 4.24: Application of the integrated pseudo-first order rate law.

the corrected rate constant derived from this work and that reported by Espenson and co-workers, probably arise from the greater concentration of water and acid (1 M $HClO_4$) used in their studies. These two factors affect the equilibrium between VO_2^+, $VO(O_2)^+$ and $VO(O_2)_2^-$ and consequently, change the concentration of diperoxovanadate. In addition, the K[$VO(O_2)$HNorida] system contains an additional ligand dissociation step in order to generate the diperoxovanadate (Figure 4.23).

As was the case for K[$VO(O_2)$Hheida], the rate of sulfoxidation is dependent on the presence of one proton per vanadium. Addition of a second proton to the reaction shows no significant effect on the rate (Figure 4.14). Coordination of peroxide to the vanadium center releases two H^+. This generates two protons per vanadium complex, which should be more than sufficient to activate the

monoanionic diperoxo species. In this case, the coordination of a diperoxo ligand would liberate the dianionic ligand from $[VO(O_2)Hnorida]^-$ which would subsequently sequester the two protons liberated from the coordination of hydrogen peroxide. The additional proton is necessary to activate the diperoxo vanadate species to carry out the sulfoxidation reaction. These results are consistent with the kinetic analysis of $[VO(O_2)_2]^-$ performed in a strongly acidic solution that provided the necessary protons to activate the complex.[14] In addition, computational studies for diperoxo molybdenum and tungsten complexes have shown that one equivalent of proton bound between the two peroxo moiety lowers the barrier to substrate oxidation.

.

Comparison of K[VO(O$_2$)Hheida] and K[VO(O$_2$)Hnorida]

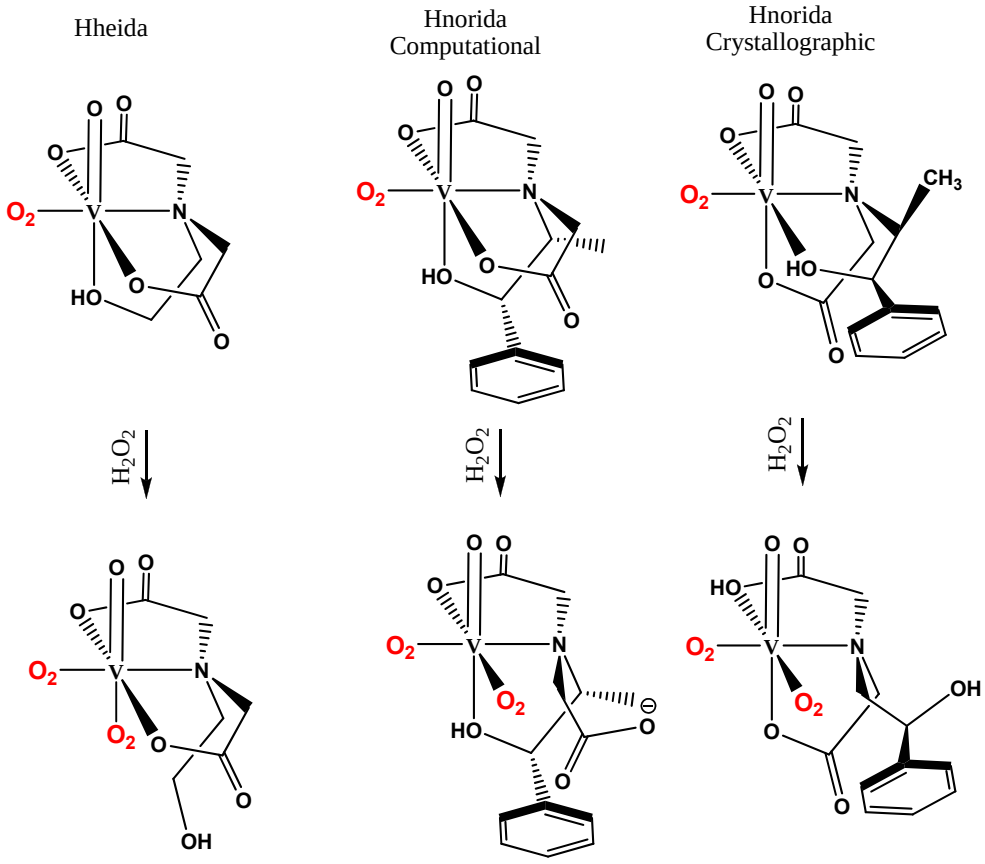

Figure 4.25: The intermediates associated with coordination of a second equivalent of hydrogen peroxide to K[VO(O$_2$)Hheida] (left), energetically favored isomer of K[VO(O$_2$)HNorida] by DFT (middle) and x-ray crystallography (right).

The formation of a catalytically active diperoxo vanadate from K[VO(O_2)Hnorida] is consistent with the lack of asymmetric sulfoxidation observed for the designed chiral catalyst. The results are in sharp contrast to the observed reactivity for K[VO(O_2)Hheida]. The ^{51}V NMR for [VO(O_2)Hheida]$^-$ is not affected by the presence of hydrogen peroxide nor substrate and only a small shift is observed upon protonation of the complex.[4] In contrast, the chiral derivative K[VO(O_2)Hnorida] readily forms diperoxo vanadate in the presence of hydrogen peroxide as was discussed above. This difference in reactivity can be explained by examining the possible intermediates formed upon the addition of a second peroxide to the vanadium center.

In the case of K[VO(O_2)Hheida], the most labile donor group, the N-hydroxyethyl arm, is also located trans to the V=O. In order for a second peroxide to coordinate to the vanadium, the N-hydroxyethyl arm must dissociate. As this position is trans to the oxo, the coordination bond formed with peroxide would be weak and the ligand set would still be tightly bound to the metal center through equatorial carboxylate donors (Figure 4.25 left). Thus, as is experimentally observed, decomposition of the complex is inhibited by the ligand's chelate effect. A different behavior occurs with the HNorida^{2-} complex, which is believed to be a consequence of the bulky substituents on the N-hydroxyethyl arms of the chiral ligand.

In order to assess the decreased stability of the [VO(O_2)HNorida]$^-$ with respect to a diperoxovanadate, it is important to identify of the solution state species for the vanadium complex. Three possible coordination modes exist for Hnorida^{2-} (Figure 4.4). Computational studies, carried out in the gas phase using a solvent continuum model, indicate that axial coordination of the N-hydroxyethyl arm of Hnorida^{2-} is energetically favored over the equatorial position. However, the solid state structure of HNorida^{2-} shows the coordination of the weakest donor, the hydroxyl, in the equatorial plane of the complex as opposed to the axial position *trans* to the V=O bond. The solid state structure may be influenced by crystal packing forces that may stabilize the higher energy isomer or one may simply crystallize the least soluble diastereomer. The computational structures

do not directly account for the effects of solvation. Consequently, both crystallographic and computational structures are viable solution state models. Since we can not *a priori* determine whether the crystallographic or computational model is a better descriptor of the solution structure of $[VO(O_2)Hnorida]^-$, we must consider both possibilities when assessing the difference in stabilities between $[VO(O_2)Hheida]^-$ and $[VO(O_2)Hnorida]^-$ The calculations predict the axial coordination mode of the N-hydroxyethyl arm to be the most stable. It may be that the steric interactions with the bulky substituents on N-hydroxyethyl arm of $HNorida^{2-}$ weakens the bond between one of the equatorial carboxylate donors and the vanadium (e.g., by restricting chelate ring conformations) allowing peroxide to coordinate in an equatorial position *cis* to the V=O (Figure 4.25 middle). This complex would be held together solely by a bidentate aminocarboxylate chelate ring and the feeble axial hydroxyl oxygen. Additionally, the trans effect of the coordinated peroxide should weaken the remaining bound carboxylate, further destabilizing the complex with respect to the diperoxovanadate. In the crystallographically characterized isomer, the alcohol is coordinated in the equatorial position trans to a carboxylate. This places the second carboxylate trans to the V=O. The elongation of the V-$O_{carboxylate}$ in the axial position illustrates the lower affinity of the carboxylate in this position. The weak equatorial hydroxyl coordination bond should allow easy access for peroxide to coordinate in the equatorial plane, *cis* to the V=O bond (Figure 4.25, right). As discussed above, this should weaken the remaining carboxylate oxygen bond, causing complex decomposition to the diperoxovanadate. In both cases, the $[VO(O_2)Hnorida]^-$ complex is expected to be unstable towards decomposition whereas the sterically less encumbered parent complex, $[VO(O_2)Hheida]^-$, should be able to withstand peroxide attack. Thus, the coordination of the second peroxide in the equatorial position of $[VO(O_2)Hnorida]^-$ facilitates the dissociation of the ligand set through the *trans* influence on a carboxylate donor, resulting in a highly catalytically active $VO(O_2)_2^-$ (Figure 4.21). The ^{51}V NMR results indicate that the diperoxo species is formed, and the sulfoxidation rate constant corrected for vanadium concentration is within

a factor of 2 of the reported second order rate constant for sulfoxidation by $VO(O_2)_2^-$ (Table 4.6).[14]

Table 4.6: Comparison of the rate constants and turnover numbers for sulfoxidation with relevant vanadium complexes. * = This work

Cmpd	Peroxide	Turnover (time, h)	Corrected or second-order k = M^{-1} s^{-1}
$K[VO(O_2)Hnorida]_{(ACN)}$	H_2O_2	400 (1)*	7.65*
$K[VO(O_2)Hnorida]_{(DCM)}$	tBuOOH	1000 (3)*	---
$K[VO(O_2)Hnorida]_{(DCM)}$	---	1 (36)*	---
$VO(O_2)_2^-{}_{(ACN/H2O)}$	H_2O_2	---	13.0[14]
$K[VO(O_2)Hheida]$	H_2O_2	950 (3)	8.1[4]

In the presence of organic peroxides the time required to achieve sulfoxidation is dramatically increased. In acetonitrile, the ligand set is labile enough to facilitate the formation of a diperoxovanadate. The dissociation of the hydroxylethyl arm of $Hnorida^{2-}$ could facilitate the ligand oxidation process the result in the decomposition of the complex. The ^1H NMR measurements of the decomposed complex shows the formation of an aromatic ketone which is consistent with a potential ligand oxidation product. Additionally, previous reports have shown that vanadium(V) is capable of oxidizing benzylic alcohols to ketones.[6,19,20] With the decreased rate of reaction with organic peroxides, the ligand oxidation process occurs at a higher rate, thereby eliminating the chiral centers in the molecule and reducing the enantioselectivity. The dissociation of the ligand from the vanadium center can be facilitated by acetonitrile through hydrogen bonding interactions with the hydroxyl proton and binding to the resulting coordinatively unsaturated vanadium species. Dichloromethane is a poor Lewis base and, therefore, can not facilitate the ligand oxidation process. This is consistent with the ESI^-/MS data and the ^{51}V NMR that show a single oxovanadium(V) Hnorida species is present. The proposed mechanism for sulfoxidation by $[VO(O_2)Hnorida]^-$ in dichloromethane in the presence and absence of hydrogen peroxide are shown in Figure 4.26.

In contrast to $Hheida^{2-}$, the $Hnorida^{2-}$ system is capable of carrying out asymmetric sulfoxidations. The single turnover experiments in the absence of H^+

in dichloromethane have an enantioselectivity of 26% in favor the S-enantiomer. Catalytic turnovers result in enantiomeric excess 14% and 19% in favor of the (R)-enantiomer for t-butylhydroperoxide and cumyl hydroperoxide respectively. This difference in enantioselectivity is explained by differences in the catalytically activated form of the Hnorida^{2-} complex which forces a preferential approach of the substrate from opposite sides of the peroxo.

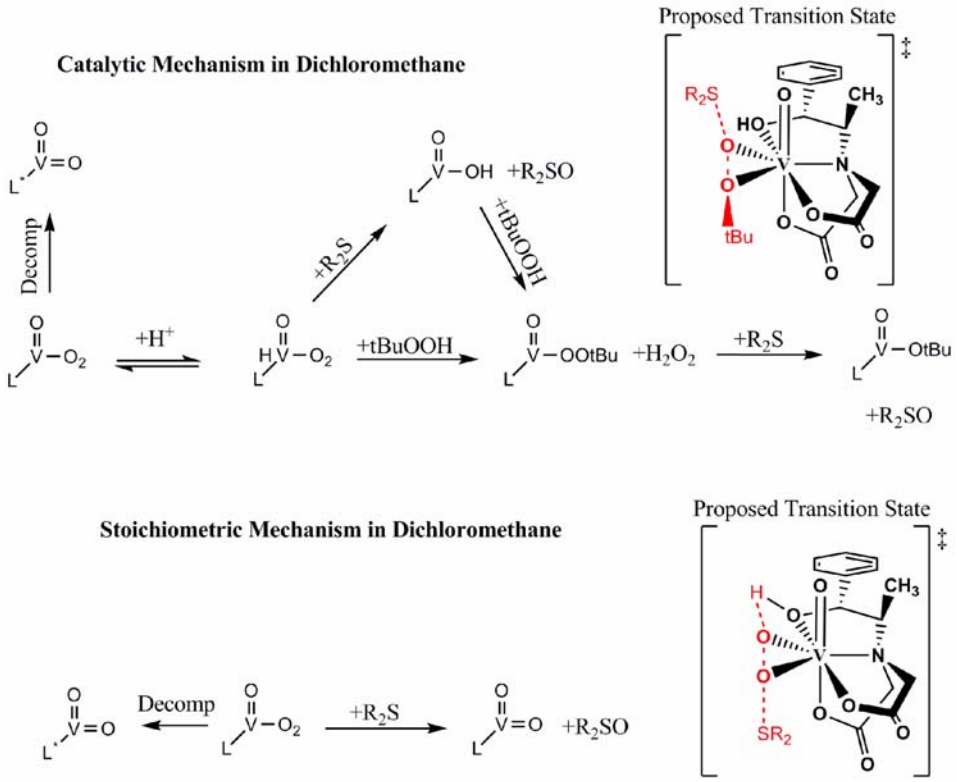

Figure 4.26: Comparison of the proposed mechanisms and transition state for sulfoxidation with K[VO(O_2)Hnorida] in dichloromethane.

Conclusion

The goal of these studies was to design an asymmetric catalyst based on a well studied well studied functional model for vanadium-dependent haloperoxidases, KVO(O_2)Hheida] that could perform asymmetric sulfoxidations with hydrogen peroxiude. The design of the ligand was based the calculated transition state geometries for sulfide oxidation with [VO(O_2)Hheida]$^-$. Typically,

computational studies are employed to rationalize the experimentally observed reactivity of the catalysts. The computational studies performed by Balcells and co-workers on Schiff-base type vanadium sulfoxidation catalysts[12,21] provide incredible insight to the reactivity of these complexes; however, the computational results have not yet been employed to design more effective catalytic systems. Another example of a computational rationalization of reactivity is present in the aminoalcohol vanadium complexes design as functional mimics of VHPOs.[18] DFT studies showed that the conformational flexibility of the ligand set the end-on coordinated cumyl peroxide reduced the enantioselectivity. In contrast, the methodology employed in this chapter utilized the knowledge of the transition state geometry to rationally design the asymmetric ligand set.

Based on the architecture of $Hheida^{2-}$, chiral centers were added to the hydroxethyl arm to break the pseudo-σ_v of $Hheida^{2-}$ thereby providing the preferential approach of sulfide to the linear transition state. The resulting oxo-peroxo complex partially accomplished the goal of asymmetric sulfoxidation with %ee of 26% for a single turnover reaction; however, the system is not capable of catalytic asymmetric sulfoxidation with hydrogen peroxide. The limitations of the K[$VO(O_2)$Hnorida] stem from the formation of non-stereoselective highly reactive diperoxo species and the propensity of the ligand set to be oxidized. The computational design methodology does not account for the stability of the complex under the reaction conditions and consequently $VO(O_2)$Hnorida was not able to accomplish the goal of asymmetric sulfoxidation with hydrogen peroxide. However, these studies demonstrate the potential role that computational methodology can play in the development of asymmetric catalysts. An important point to consider is the number of accessible transition for any catalytic transformation. Reliable estimations of the enantiomeric excess require accurate and thorough calculations of all transition state geometries after which a simple Boltzmann analysis can be applied to determine the enantioselectivity. Questions can be raised regarding the accuracy of the computed transition state barriers. To address this issue, future studies should

compare experimentally determined barriers to activation to the calculated values from a variety of density functionals. This comparison calibrates the calculation to experimental system and will lead an improvement the prediction of the enantiomeric excess.

Existing chiral sulfoxidation systems with vanadium, in particular the asymmetric Schiff-base oxovanadium(V) complexes, are highly effective, achieving enantioselectivities > 85% for alkyl aryl sulfides[2] and >97% for disulfides.[3] The use of chiral Schiff-base complexes of vanadium for sulfoxidation was originally reported by Nakajima and co-workers in 1986,[1] these original systems under ideal conditions afford a 40% enantiomeric excess in the presence of organic peroxides. Since that time a number of groups have optimized derivatization of the ligand and the experimental conditions to achieve the >98% enantioselectivities.[10,22-24] As a first attempt at the development of asymmetric sulfoxidation catalysts, K[VO(O_2)Hnorida] has performed exceptionally well. By applying modern computational methods to an established catalytic system, we have designed an asymmetric catalyst bypassing the typical combinatorial approach to ligand design.

This work also underscores the important role that diperoxovanadate species play in vanadium based catalysis. The abundance of monoperoxo-oxovanadium(V) complexes that have been examined in catalytic reactions is astounding,[13,24,25] and yet little attention is paid to the potential formation of diperoxo species in the catalytic reaction. The strong solvent dependence on stereoselectivity with Schiff-base vanadium catalysts alludes to the importance of non-selective oxidants and the potential formation of diperoxovanadates interfering with sulfoxidation.[3] Espenson and co-workers provided an invaluable study demonstrating the catalytic competence of diperoxovanadates for oxo-transfer type catalysis.[14] The solution speciation and kinetic studies contained herein provide an example of the importance of diperoxovanadates when high concentrations of hydrogen peroxide are employed as a terminal oxidant.

With the advances in modern computational chemistry, the ability to identify the transition state geometries for a variety of catalytic process is possible. This

information provides invaluable tool for the rational design and development of asymmetric catalysis. The typical combinatorial approach to catalyst design in which large array of ligand derivatives and substrates are assayed to determine the optimal conditions. This process takes significant amounts of time and resources as is evident by the decades of research that have occurred for Jacobsen catalysts,[26] Sharpless epoxidation system,[27] and the vanadium Schiff-base sulfoxidation catalysts.[24] The application of modern computational methods to assist in the design of asymmetric catalysts serves to streamline this process saving resources and time. The studies contained herein provide an example of computationally assisted ligand design for asymmetric catalysis.

References

1. Nakajima, K.; Kojima, M.; Fujita, J. *Chemistry Letters* **1986**, 1483-1486.

2. Bolm, C.; Bienewald, F. *Angewandte Chemie, International Edition in English* **1996**, *34*, 2640-2642.

3. Blum, S. A.; Bergman, R. G.; Ellman, J. A. *Journal of Organic Chemistry* **2003**, *68*, 153-155.

4. Smith, T. S.; Pecoraro, V. L. *Inorganic Chemistry* **2002**, *41*, 6754-6760.

5. Reetz, M. T.; Drewes, M. W.; Schmitz, A. *Angewandte Chemie* **1987**, *99*, 1186-1188.

6. Velusamy, S.; Punniyamurthy, T. *Organic Letters* **2004**, *6*, 217-219.

7. Jaswal, J. S.; Tracey, A. S. *Inorganic Chemistry* **1991**, *30*, 3718-3722.

8. Sharpless, K. B.; Verhoeven, T. R. *Aldrichimica Acta* **1979**, *12*, 63-74.

9. Palucki, M.; Finney, N. S.; Pospisil, P. J.; Gueler, M. L.; Ishida, T.; Jacobsen, E. N. *Journal of the American Chemical Society* **1998**, *120*, 948-954.

10. Sun, J.; Zhu, C.; Dai, Z.; Yang, M.; Pan, Y.; Hu, H. *Journal of Organic Chemistry* **2004**, *69*, 8500-8503.

11. Schneider, C. J.; Zampella, G.; Greco, C.; Pecoraro, V. L.; De Gioia, L. *European Journal of Inorganic Chemistry* **2007**, 515-523.

12. Balcells, D.; Maseras, F.; Ujaque, G. *Journal of the American Chemical Society* **2005**, *127*, 3624-3634.

13. Butler, A.; Clague, M. J.; Meister, G. E. *Chemical Reviews (Washington, D. C.)* **1994**, *94*, 625-638.

14. Du, G.; Espenson, J. H. *Inorganic Chemistry* **2005**, *44*, 2465-2471.

15. Sawada, Y.; Matsumoto, K.; Kondo, S.; Watanabe, H.; Ozawa, T.; Suzuki, K.; Saito, B.; Katsuki, T. *Angewandte Chemie, International Edition* **2006**, *45*, 3478-3480.

16. Zampella, G.; Fantucci, P.; Pecoraro, V. L.; De Gioia, L. *Journal of the American Chemical Society* **2005**, *127*, 953-960.

17. Zampella, G.; Fantucci, P.; Pecoraro, V. L.; De Gioia, L. *Inorganic Chemistry* **2006**, *45*, 7133-7143.

18. Wikete, C.; Wu, P.; Zampella, G.; De Gioia, L.; Licini, G.; Rehder, D. *Inorganic Chemistry* **2007**, *46*, 196-207.

19. Jiang, N.; Ragauskas, A. J. *Journal of Organic Chemistry* **2007**, *72*, 7030-7033.

20. Bortolini, O.; Conte, V.; Di Furia, F.; Modena, G. *Nouveau Journal de Chimie* **1985**, *9*, 147-150.

21. Balcells, D.; Maseras, F.; Lledos, A. *Journal of Organic Chemistry* **2003**, *68*, 4265-4274.

22. Jeong, Y.-C.; Choi, S.; Hwang, Y. D.; Ahn, K.-H. *Tetrahedron Letters* **2004**, *45*, 9249-9252.

23. Barbarini, A.; Maggi, R.; Muratori, M.; Sartori, G.; Sartorio, R. *Tetrahedron: Asymmetry* **2004**, 2467-2473.

24. Bolm, C. *Coordination Chemistry Reviews* **2003**, *237*, 245-256.

25. Hirao, T. *Chemical Reviews (Washington, D. C.)* **1997**, *97*, 2707-2724.

26. McGarrigle, E. M.; Gilheany, D. G. *Chemical Reviews (Washington, DC, United States)* **2005**, *105*, 1563-1602.

27. Lane, B. S.; Burgess, K. *Chemical Reviews (Washington, DC, United States)* **2003**, *103*, 2457-2473.

Chapter 5

Conclusion

Functional modeling of metalloenzymes provides new insight into the mechanism of an enzyme. Our group has developed a series of functional models to mimic the activity of vanadium dependent haloperoxidases. The best functional model for the halide and sulfide oxidations of VHPOs to date is K[$VO(O_2)$Hheida]. This complex is capable of mimicking the bromide and sulfide oxidation abilities of the enzyme and has led to much greater understanding of the mechanism. For bromide oxidation $[VO(O_2)Hheida]^-$ has a second order rate constant of 280 M^{-1} s^{-1}, whereas the enzyme has k_{cat}/K_M = 1.7 x 10^{-5} M^{-1} sec^{-1}.[1] In the case of sulfoxidation, the functional model can perform 950 turnovers in 3 hours and the enzyme can perform 520 turnovers in 20 hours.[2] In its own right, $[VO(O_2)Hheida]^-$ is a highly efficient sulfoxidation catalysts. The studies presented in this thesis have focused on understanding the mechanism of oxidation for this complex and applying that information for the design of an asymmetric catalyst.

At the onset of this project, two key questions could be raised regarding the mechanism of substrate oxidation for VHPOs and their functional mimics: 1) what is the role of protonation in activation of the vanadium-peroxo species, and 2) what is the transition state for this process. Density functional theory was used to explore the chemically feasible pre-catalytic species, protonation states, and transition states for halide and sulfide oxidation. We have shown that coordination of the hydroxyl ethyl arm of Hheida is energetically favored over coordination of an exogenous donor such as acetonitrile or water. Seven protonated intermediates were found, the most stable of which is a hydroperoxo species. Protonation of the V=O bond or the carboxylate of the ligand are 2.9

and 1.3 kcal/mol higher in energy, respectively. Transition states were located for thioether and halide oxidations (halide = I^-, Br^-, and Cl^-), all transition states were S_N2-like, with a nearly linear substrate-peroxo oxygen bond angles (S-O-O ≈ 0º). Protonation of the peroxo moiety dramatically reduces the activation barrier for both thioether and halides; however, the energy of activation is insensitive to the identity of the halide. This result further supports the hypothesis that the inability of K[VO(OOH)Hheida] to oxidize chloride is the result of the increasing basicity of the substrate, which leads to deprotonation of the catalytically active hydroperoxo species.

The computational studies provide insight into the number of potential protonated species; however, the gas phase calculations overestimate the energetic differences between intermediates due to the lack of various stabilizing interactions of the solvent with the protonated complex. X-ray absorption and vibrational spectroscopies were employed to determine if a discrete protonated intermediate is present upon addition of a H^+ to the VHPO functional model K[VO(O_2)Hheida]. The pre-edge transition of the x-ray absorption spectrum does not change upon protonation of the complex. Within the uncertainty of the measurements, this demonstrates that a maximum of 20% of a protonated oxo species (V-OH) exists under catalytic conditions. The vibrational spectroscopies, in both solution and in the solid state, for H[VO(O_2)Hheida] are inconsistent with the formation of a single protonated intermediate. The small shifts observed for the peroxo, oxo, and carboxylate vibrational bands indicate that a single protonated species does not form upon protonation. The apparent pK_a of H[VO(O_2)Hheida] in acetonitrile is 6.0 (HBr pK_a = 5.5)[1] and the small energy differences between the protonated isomers, as calculated by DFT, are both consistent with the proposal that multiple protonated species are present. The modified mechanism for sulfide oxidation by [VO(O_2)Hheida]$^-$ is presented in Figure 5.1.

These spectroscopic studies provide further support that the role of Lys353 in the active site of VHPOs is to direct the protonation of key oxygen ligand to carry out catalysis. Computational studies have shown that this hydrogen bonding interaction reduces the barrier to activation for nucleophilic substrate oxidation.[3] Approach of the substrate induces polarization of the peroxo moiety transferring the proton from the lysine residue to the peroxo moiety. Based on our vibrational studies, $[VO(O_2)Hheida]^-$ undergoes a similar process with the proton being weakly associated to a variety of protonated intermediates where the transition

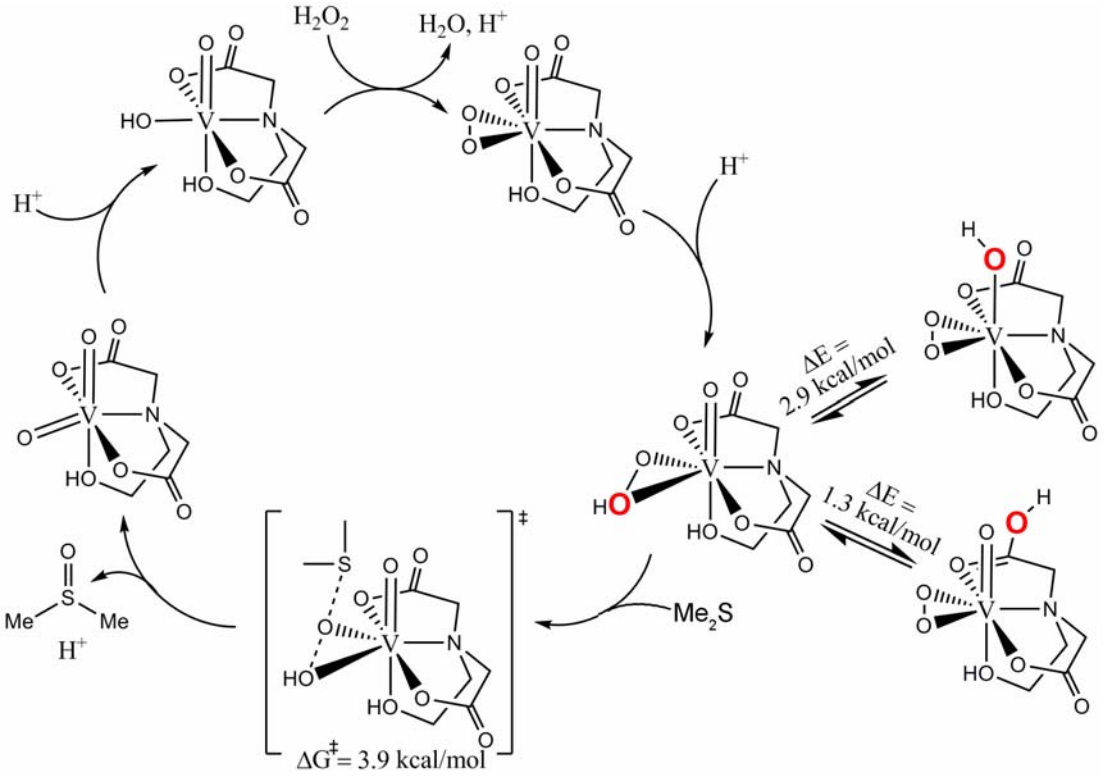

Figure 5.1: Modified mechanism for sulfoxidation by $[VO(O_2)Hheida]^-$ explicity taking into account hydrogen peroxide binding.

state selects the protonated form with the lowest barrier to activation. Hydrogen bonding has also been implicated in the activation of peroxo-titanium(IV)[4] complexes, and the diperoxo-Mo(VI)[5] and W(VI)[6] systems. Protonation of these systems polarizes the peroxo bond and activates the complexes for epoxidation. Hydrogen bond donors, whether intermolecular, as is the case for VHPOs,[3,7] and intramolecular, for Ti(IV),[8] Mo(VI),[5] and W(VI)[6] can activate peroxo metal complexes for catalytic oxidations. Our studies have expanded the understanding

of the role of protonation in the activation of K[VO(O_2)Hheida] for substrate oxidation and reinforce the proposed role of the hydrogen bond donors in VHPOs and d^0 peroxo-metal catalysts.

Using the calculated transition-state geometries, a chiral ligand set was designed based on $Hheida^{2-}$ (N-2-hydroxyethyl iminodiacetic acid). The hypothesis was that breaking the pseudo-σ_v symmetry of K[VO(O_2)Hheida] would impart a preferential approach for the substrate to the reactive hydroperoxo species, thereby enhancing the stereoselectivity of sulfoxidation. Two chiral centers were added to the hydroxethyl arm and the peroxo-oxovanadium(V) complex was isolated. Computational studies, performed by our collaborator, Prof. Luca DeGioia, showed that three confirmations of the ligand set around the peroxo-oxovanadium(V) center existed. Axial coordination of the N-hydroxyethyl arm of $Hnorida^{2-}$ is the energetically preferred confirmation. The predicted enantiomeric excess for K[VO(O_2)Hnorida] with hydrogen peroxide should be >90% in favor of the R enantiomer assuming a preferential approach of the sulfide form the left hand side of the complex. The use of *t*-butylhydroperoxide reduces the %ee to 40% in favor of the R-sulfoxide. The chiral complex, K[VO(O_2)Hnorida], accomplished the goal of asymmetric sulfoxidation with 26 %ee (S-sulfoxide) for a single turnover reaction and 19% (R-sulfoxide) with *t*-butylhydroperoxide. The difference in the enantioselectivity for this reaction arises from appropriate coordination mode necessary to activate the complex for sulfoxidation. In the case of the single-turnover reaction, a hydrogen bond must be formed with the peroxo moiety. Calculations show that the most stable ligand confirmation that can form a hydrogen bond with the peroxo moiety involves the binding of the N-hydroxyethyl arm in the equatorial plane. In contrast, the *t*-butyl peroxovanadium(V) species does not need to form a hydrogen bond to activate the peroxo moiety. In this case, the most stable isomer involves the axial coordination of the N-hydroxyethyl donor, thereby presenting a different chiral environment in the transition state.

Existing chiral sulfoxidation systems containing vanadium, in particular the asymmetric Schiff-base oxovanadium(V) complexes, are highly effective,

achieving enantioselectivities > 85% for alkyl aryl sulfides[9] and >97% for disulfides.[10] The use of chiral Schiff-base complexes of vanadium for sulfoxidation was originally reported by Nakajima and co-workers in 1986.[11] These original systems, under ideal conditions, afford a 40% enantiomeric excess in the presence of organic peroxides. Since that time, a number of groups have optimized the choice of ligand and the experimental conditions to achieve the >98% enantioselectivities.[12-15] The first generation chiral catalyst, K[VO(O_2)Hnorida], was designed on the basis of modern computational methods and established sulfoxidation catalysts. This rational design process bypasses the presently fashionable combinatorial approach typically applied to the development of asymmetric oxidants.

An abundance of monoperoxo-oxovanadium(V) complexes have been examined in catalytic reactions;[14,16,17] yet little attention has been paid to the potential formation of diperoxo species in the catalytic reaction. The strong dependence of stereoselectivity on the nature of the solvent with Schiff-base vanadium catalysts suggests that non-selective oxidants and potentially the formation of diperoxovanadates interfers with sulfoxidation.[10] Espenson and co-workers provided an invaluable study demonstrating the catalytic competence of diperoxovanadates for oxo-transfer type catalysis.[18] Our solution speciation and reactivity studies provide further support for the role of diperoxovanadates as competitive oxidants in vanadium-based catalytic oxidations.

Future Work

Modern computational chemistry is an effective tool for investigating the mechanism of transition metal catalysts. The work presented in this thesis provides an example of the application of DFT to the design of asymmetric sulfoxidation catalysts. The future direction of these calculations should focus on more sterically constraining systems, in particular models of [VO(O_2)Hnorida]$^-$ with prochiral sulfoxides. The differences in barriers to activation for pro-R and pro-S transition states can be determined and compared to the experimental

values. After locating the transition states and energy-minimized starting material adducts, a variety of chiral substitutions can be made *in silico* to find those with optimized energetic differences between the pro-R and pro-S transition states. This computational screening approach can direct the future design of asymmetric catalysts based on $Hheida^{2-}$.

In light of the results presented in thesis, there are some inherent limitations to the computational design of asymmetric catalysis. The current computational methodology neither accounts for the formation of non-selective oxidants, such as diperoxovanadate, nor takes into account the explicit solvation effects during the geometry optimization or transition state searches. There are inherent complications for the implicit solvation of a complex *in silico* with respect to the complexity of the potential energy surface and the computational time. As a first approximation of solvation, future calculations should include a computationally feasible number of solvent molecules and allow for the formation of hydrogen bonds in the transition state searches. The development of implicit solvation models would dramatically improve the predicted reactivity of transition metal complexes by modern computational methods. The prediction of the enantioselectivity using computational methods requires an exhaustive determination of all possible transition state geometries. In addition, the relative error in the energetic differences between transition states needs to be accounted for when calculating the enantiomeric excess. Future studies should use experimentally determined barriers to activation as a calibration for the choice of density functional used to calculate the transition states. This provides a more accurate depiction of the energetic difference between enantiomeric transition states and consequently results in a better prediction of the enantiomeric excess. The errors inherent in the computational methodology, which we have estimated at approximately 2 kcal/mol, can be accommodate for by the appropriate binning of the barriers to activations. Difference in energies less than the error should be treated as isoenergetic states for the purposes of a Boltzmann analysis to determine the enantiomeric excess. This method would

eliminate the over interpretation of the computational results and provide a more applicable comparison with the experimental results.

The role of protonation for d^0 metal peroxo-catalysts presented in this work raises questions regarding the design of asymmetric oxidation catalysts. The competitive protonation of ligand donors, M=O, and the peroxo moiety reduce the quantity of catalytically active species in solution and increase the number of confirmational isomers available for the oxidative transition state. The design of the asymmetric ligand Hnorida^{2-} was performed before the completion of the spectroscopic studies that are presented in Chapter 3. By accounting for this new information, a new class of oxidation catalysts can be developed. The introduction of hydrogen bond donors to ligand sets would reduce the number of conformational isomers in solution and improve the reactivity of the catalyst. To this end, the use of constrained secondary amines with the Hheida^{2-} architecture would provide a versatile platform to examine the effects of hydrogen-bonding on the rates of substrate oxidation (Figure 5.2 and Figure 5.3). This work would provide significant insight into the role of hydrogen bonding residues in the activation of VHPOs and lays the foundation for the development of a new class of asymmetric sulfoxidation catalysts.

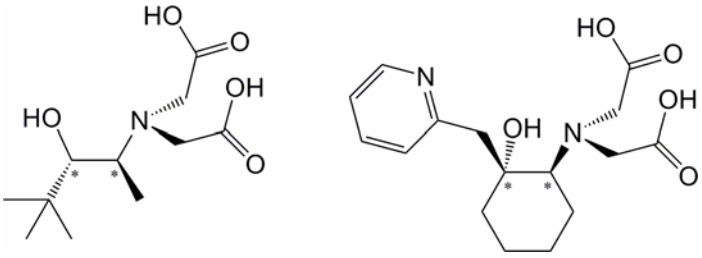

Figure 5.2: Proposed asymmetric ligands

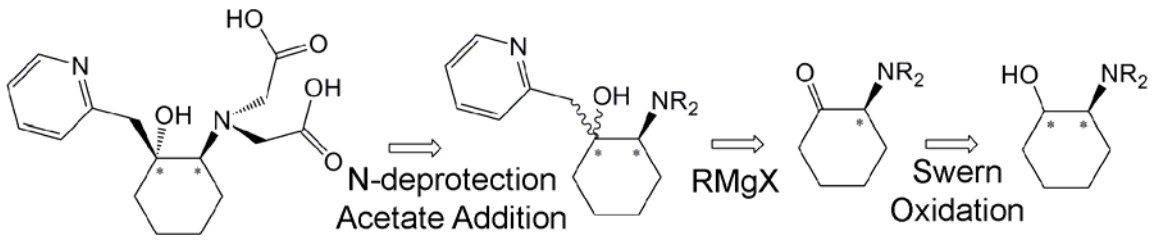

Figure 5.3: Retrosynthesis of asymmetric ligands containing H-Bond donors.

The susceptibility of Hnorida^{2-} to oxidation at the benzylic alcohol position complicates detailed studies of the asymmetric oxidation reaction. The synthesis of the *t*-butyl derivative of Hnorida^{2-} was presented in Chapter 4. This synthesis provides a facile means of introducing other sterically hindering groups in a diastereospecific fashion. Future work on this system should be focused on the synthesis of the peroxo-oxovanadum(V) complex with the *t*-butyl derivative of HNorida^{2-}. This ligand reduces the possibility of oxidation at the secondary alcohol and increases the steric bulk of the complex. A critical observation from the reactivity of Hnorida^{2-} is that the sterically encumbering nature of the chiral derivatized arm facilitates the formation of diperoxovanadate with excess H_2O_2. Future work with the *t*-butyl derivative of Hnorida^{2-} should focus on limiting the concentrations of H_2O_2 via slow addition with a syringe pump. By reducing the H_2O_2 concentration, the propensity of the complex to form diperoxovanadate will be hindered. The use of organic peroxides should be explored extensively with the *t*-butyl derivative, specifically focusing the solvent and temperature dependence of the enantioselectivity.

The types of chiral tripodal amine ligands described in this thesis provide a platform to design new asymmetric catalysts using manganese. The manganese(II) complex of HNorida^{2-} has been isolated from degassed aqueous solutions with manganese(II) chloride or nitrate. The Ortep diagram of Mn^{II}Hnorida is depicted Figure 5.4. The octahedral complex contains the four donors of the ligand set, a water molecule, and the sixth coordination site occupied by a bridging carboxylate oxygen. The bridging carboxylate oxygen results in a linear chain structure in the solid state. Initial attempts to use this complex as an epoxidation or sulfoxidation catalysts with hydrogen peroxide in DMF have not resulted in any detectable oxidations. Further work on this complex should focus on determining the reduction potential for Mn^{II}/Mn^{III} redox couple and compare that to the oxidation potential of the HNorida^{2-}. These studies will determine whether hydrogen peroxide is a strong enough oxidant to reach a high valent managese species that can carry out oxidative catalysis and provides the necessary information to determine the stability of the ligand under

oxidative conditions. The comparison of the reduction potentials for the metal and the ligand set requires a non-redox active metal be complexes to HNorida^{2-}. To this end, the zinc(II) complex of HNorida^{2-} can be synthesized from aqueous complexation of the ligand with any aqueous soluble zinc(II) salt. ZnHnorida is insoluble in aqueous solutions. The MnHNorida complex is likely to be prone to ligand oxidation, as was the case for the vanadium(V) complex. However, initial work in this area will provide the necessary synthetic knowledge to explore the reactivity of these complexes with the ligand sets described above.

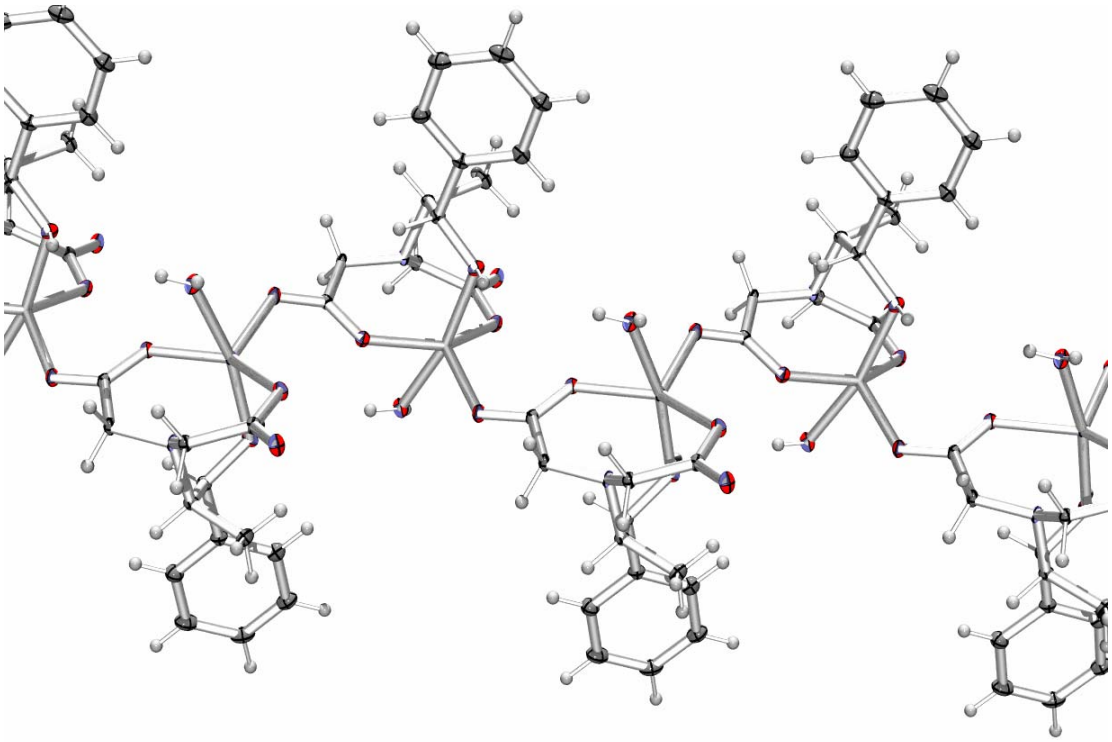

Figure 5.4: Ortep diagram of the linear chain structure formed by MnHnorida at 50% probablility.

References

1. Colpas, G. J.; Hamstra, B. J.; Kampf, J. W.; Pecoraro, V. L. *J. Am. Chem. Soc.* **1996**, *118*, 3469-3478.

2. Smith, T. S.; Pecoraro, V. L. *Inorg. Chem.* **2002**, *41*, 6754-6760.

3. Zampella, G.; Fantucci, P.; Pecoraro, V. L.; De Gioia, L. *J. Am. Chem. Soc.* **2005**, *127*, 953-960.

4. Sawada, Y.; Matsumoto, K.; Kondo, S.; Watanabe, H.; Ozawa, T.; Suzuki, K.; Saito, B.; Katsuki, T. *Angew. Chem., Int. Ed. Engl.* **2006**, *45*, 3478-3480.

5. Gisdakis, P.; Yudanov, I. V.; Roesch, N. *Inorg. Chem.* **2001**, *40*, 3755-3765.

6. Di Valentin, C.; Gisdakis, P.; Yudanov, I. V.; Roesch, N. *J. Org. Chem.* **2000**, *65*, 2996-3004.

7. Messerschmidt, A.; Prade, L.; Wever, R. *ACS Symp. Ser.* **1998**, *711*, 186-201.

8. Yudanov, I. V.; Gisdakis, P.; Di Valentin, C.; Rosch, N. *Eur. J. Inorg. Chem.* **1999**, 2135-2145.

9. Bolm, C.; Bienewald, F. *Angew. Chem., Int. Ed. Engl.* **1996**, *34*, 2640-2642.

10. Blum, S. A.; Bergman, R. G.; Ellman, J. A. *J. Org. Chem.* **2003**, *68*, 153-155.

11. Nakajima, K.; Kojima, M.; Fujita, J. *Chem. Lett.* **1986**, 1483-1486.

12. Jeong, Y.-C.; Choi, S.; Hwang, Y. D.; Ahn, K.-H. *Tetrahedron Lett.* **2004**, *45*, 9249-9252.

13. Barbarini, A.; Maggi, R.; Muratori, M.; Sartori, G.; Sartorio, R. *Tetrahedron: Asymm.* **2004**, 2467-2473.

14. Bolm, C. *Coord. Chem. Rev.* **2003**, *237*, 245-256.

15. Sun, J.; Zhu, C.; Dai, Z.; Yang, M.; Pan, Y.; Hu, H. *J. Org. Chem.* **2004**, *69*, 8500-8503.

16. Butler, A.; Clague, M. J.; Meister, G. E. *Chem. Rev.* **1994**, *94*, 625-638.

17. Hirao, T. *Chem. Rev.* **1997**, *97*, 2707-2724.

18. Du, G.; Espenson, J. H. *Inorg. Chem.* **2005**, *44*, 2465-2471.